DIELECTRON PRODUCTION IN HEAVY ION COLLISIONS AT 158 GEV/C PER NUCLEON

Vom Fachbereich Physik
der Technischen Universität Darmstadt

zur Erlangung des Grades
eines Doktors der Naturwissenschaften
(Dr. rer. nat.)

genehmigte Dissertation von

Dipl.-Phys. Oliver Busch

aus Darmstadt

Referent: Prof. Dr. P. Braun-Munzinger
Koreferent: Prof. Dr. J. Wambach
Tag der Einreichung: 17.10.07
Tag der Prüfung: 03.12.07

Darmstadt 2007
D17

Dielektronenproduktion in Schwerionenkollisionen bei 158 GeV/c pro Nukleon

Thema der vorliegenden Arbeit ist die Produktion von Dileptonen in Pb-Au Kollisionen bei 158 GeV/c pro Nukleon, gemessen mit dem Cherenkov Ring Electron Spectrometer (CERES) Experiment am Super Proton Synchrotron (SPS) am CERN. Im Jahr 2000 verfügte das Experiment erstmals über eine voll funktionsfähige Time Projection Chamber (TPC). Die exzellente Spurrekonstruktion der TPC eröffnet neue Möglichkeiten der Teilchenidentifikation mit dem CERES Ring Imaging Cherenkov (RICH) Detektor. Die Arbeit beschreibt Entwicklung und Optimierung spurbasierter Ringrekonstruktionsmethoden zur Identifikation von Elektronen sowie Pionen mit Impulsen über der Cherenkovschwelle. Verschiedene Ansätze werden anhand der CERES Daten verglichen. Dies gestattet zum ersten Mal die CERES RICH Effizienz und Unterdrückung des Untergrunds experimentell zu bestimmen.

Wir nutzen die neu entwickelten Methoden der Teilchenidentifikation zur Rekonstruktion von Elektronenpaaren bei kleinen invarianten Massen. Wir konnten die Beschreibung des Detektors im Rahmen von Monte-Carlo-Simulationen erheblich verbessern. Die Simulationen erlauben nicht nur eine präzise Beschreibung der Rekonstruktionseffizienz sondern auch die Analyse des kombinatorischen Untergrunds. Motiviert durch das bessere Verständnis des Untergrunds wurde die TPC Spurrekonstruktion erweitert, um bessere Spureffizienz bei kleinen Impulsen und Unterdrückung von Elektronen aus physikalisch trivialen Quellen zu erzielen.

Unsere Ergebnisse bestätigen die früheren Beobachtungen durch CERES, wonach im Bereich invarianter Massen $m_{inv} \gtrsim 0.2$ GeV/c^2 ein starker Überschuss an Elektronenpaaren relativ zum hadronischen Cocktail vorliegt. Unsere Resultate sind konsistent mit den Ergebnissen früherer Analysen der gleichen Daten. Der Vergleich bestätigt unsere Abschätzung der systematischen Unsicherheiten der Elektronenanalyse. Wir beobachten eine ausgeprägte Modifikation der spektralen Funktion des ρ Mesons im heissen, dichten Medium, und unsere Ergebnisse weisen deutlich auf baryonische Wechselwirkungen als Ursprung des Effekts hin.

Weiterhin präsentieren wir in dieser Arbeit die erste direkte Messung von Übergangsstrahlungsspektren in irregulären Radiatoren, durchgeführt mit Prototypen des ALICE (A Large Ion Collider Experiment) Transition Radiation Detectors (TRD). Der Vergleich der Messungen mit Berechnungen für reguläre Radiatoren zeigt für verschiedene Elektronenimpulse gute Übereinstimmung, sowohl hinsichtlich der abgestrahlten Gesamtenergie als auch in den spektralen Verteilungen.

Dielectron Production in Heavy Ion Collisions at 158 GeV/c per Nucleon

In this thesis we study dilepton production in Pb-Au collisions at 158 GeV/c per nucleon measured with the Cherenkov Ring Electron Spectrometer (CERES) at the Super Proton Synchrotron (SPS) at CERN. The data taken in the year 2000 represent the first CERES runs with the fully operational Time Projection Chamber (TPC). The upgrade of the spectrometer with this powerful tracking device allows to realize a new approach for particle identification with the Ring Imaging Cherenkov (RICH) detector. We present the development and optimization of track-based ring reconstruction methods which allow to identify both electrons and pions at momenta above the Cherenkov threshold. To compare the performance of different methods, the reconstruction is applied to the CERES data. This allows to determine experimentally, for the first time, the CERES RICH efficiency and background rejection power.

The new particle identification is used for low-mass dielectron reconstruction. Significant improvements in the simulation of the detector allow to evaluate the electron pair reconstruction efficiency with high accuracy and to study the origin of electron pair combinatorial background. The results motivate an extension of the TPC tracking, to improve the reconstruction efficiency for low-momentum tracks, and allow better identification of electron background.

Our results corroborate the previous CERES findings of an enhancement of electron pairs over the hadronic cocktail in the invariant mass region $m_{inv} \gtrsim 0.2$ GeV/c^2. Comparison to previous analyses of the same data shows good consistency and supports our estimate of the systematic uncertainties of the electron analysis. Our results supply evidence for a modification of the spectral function of the ρ meson in the hot and dense medium and strongly support baryon-induced interactions at the origin of the effect.

Furthermore, we present in this work the first direct measurements of transition radiation (TR) spectra in irregular radiators, carried out with prototypes of the ALICE (A Large Ion Collider Experiment) transition radiation detector (TRD). The measurements are confronted with calculations for regular radiators. The TR yield and the shape of the spectral distributions for different electron momenta are well described by the simulations.

Contents

1 Introduction

1.1 Symmetries of QCD

Collisions of heavy ions at ultra-relativistic energies allow to assess properties and evolution of strongly interacting matter under extreme conditions, in particular the predicted transition to a state of matter where chiral symmetry is restored and the fundamental degrees of freedom become quarks and gluons (Quark-Gluon-Plasma).
In this chapter we give an introduction to the theoretical description of strong interactions, the phenomenology of non-perturbative symmetry breaking in vacuum and at finite temperature and density and a short overview of the experimental efforts to study the expected effects in heavy-ion collisions.

In the Standard Model of particle physics, strong interactions are described by Quantum Chromodynamics (QCD) [1, 2, 3], with quarks and gluons as elementary degrees of freedom. The dynamics is governed by the QCD Lagrangian [4]

$$L_{QCD} = \overline{\Psi}(i\gamma^\mu D_\mu \ - M^0)\Psi - \frac{1}{4}G^\alpha_{\mu\nu}G^{\mu\nu}_\alpha \tag{1.1}$$

with the non-abelian gluonic field-strength tensor given as

$$G^a_{\mu\nu} = \partial_\mu A^a_\nu - \partial_\nu A^a_\mu + igf^{abc}A^b_\mu A^c_\nu$$

where A^a_μ represents the spin 1 gluon field with color index a (a = 1..8). QCD is a gauge theory, invariant under local SU(3) color transformations. The gauge covariant derivative

$$D_\mu = \partial_\mu - ig(\lambda_a/2)A^a_\mu$$

induces a coupling between the spin-1/2, colored matter fields Ψ and the gauge fields A^a_μ (with λ_a the Gell-Mann matrices, the generators of the group, defined via the structure constants $[\lambda_a, \lambda_b] = f_{abc}\lambda_c$). Each of the $N_f = 6$ flavors of quarks ('up, down, strange, charm, beauty, top'), comes in 3 colors ('red, blue, green'):

$$\Psi^T = (\ \Psi_r, \Psi_b, \Psi_g\ )$$

The matrix $M^0 = \mathrm{diag}(\mathrm{m_u}, \mathrm{m_d}, \mathrm{m_s}, \mathrm{m_c}, \mathrm{m_t}, \mathrm{m_b})$ is composed of the bare quark masses. The coupling strength g, commonly expressed in terms of $\alpha_s = g^2/4\pi$, depends on the

momentum transfer Q at which it is probed. This `running coupling` is a consequence of radiative corrections to the scattering amplitude of the investigated process. While QCD does not predict the actual size of $\alpha_s(Q^2)$ at a particular energy scale Q^2, its energy dependence is precisely determined, given a value at a scale μ^2. In 1-loop approximation

$$\alpha_s(Q^2) = \frac{\alpha_s(\mu^2)}{1 + \alpha_s(\mu^2)\,\beta_0\,ln(Q^2/\mu^2)} \tag{1.2}$$

with $\beta_0 = (33 - 2N_f)/(12\pi)$. To fully specify QCD, the value of α_s has to be determined from experiment [5], e.g. at the Z-Boson mass $m_Z = 91$ GeV, $\alpha_s(m_Z^2) = 0.118$ [6].
The equation exhibits a remarkable property of QCD: the coupling decreases with increasing momentum transfer. This specific behavior, opposite to the evolution in QED, is due to the color charge of the gauge bosons of the theory: gluons are self-interacting, which leads to a contribution from gluon loops to the gluon propagator, resulting in an antishielding of the bare charge, which overcomes the shielding due to fermion loops.
In the limit of very large momentum transfer Q^2, α_s ultimately will decrease to zero, or, in non-relativistic language: the quark-quark potential is zero at small distances. This phenomenon is known as `asymptotic freedom`. On the other hand, Eq. 1.2 indicates that $\alpha_s(Q^2)$ grows to large values and actually diverges to infinity at small Q^2. It is common to parametrize the energy dependence of the coupling in terms of the scale parameter Λ. To first order

$$\alpha_s(Q^2) = \frac{1}{\beta_0\,ln(Q^2/\Lambda^2)} = \frac{4\pi}{(11 - \frac{2}{3}N_f)\,ln(Q^2/\Lambda^2)}$$

Technically, Λ is identical to the energy scale Q where α_s diverges to infinity. To give a value, $\Lambda = 220$ MeV in 4-loop approximation, using the renormalization scheme and N_f as in [6]. Clearly, for values of $Q^2 \simeq 1\ \mathrm{GeV}^2$, perturbative expansions in the coupling constant are not meaningful any more, as α_s approaches and eventually exceeds unity. At these energy scales, the colored quarks and gluons are `confined` in colorless bound states, the hadrons of our every-day world. The assessment of QCD in the non-perturbative regime is presently one of the greatest theoretical challenges.

In field theory, invariance of the Lagrange density under a group transformation (symmetry of the theory with respect to the group) entails a conserved Noether current [7] [8]. Apart from the invariance under local $SU(3)_{color}$ transformations and a global U(1) symmetry (invariance under phase transformation of the fermion fields) from which results baryon number conservation, the Lagrangian Eq. 1.1, in the limit of vanishing quark masses, is invariant under global vector and axialvector transformation in SU(3)-flavor space:

$$\Psi \rightarrow e^{-i\alpha_V^i \frac{\lambda^i}{2}}\Psi \qquad\qquad \Psi \rightarrow e^{-i\alpha_A^i \frac{\lambda^i}{2}\gamma_5}\Psi \tag{1.3}$$

with conserved vector and axialvector Noether currents

$$j^{\mu}_{V,i} = \overline{\Psi}\gamma^{\mu}\frac{\lambda_i}{2}\Psi \qquad\qquad j^{\mu}_{A,i} = \overline{\Psi}\gamma^{\mu}\gamma_5\frac{\lambda_i}{2}\Psi$$

As a consequence, the corresponding charges

$$Q^V_i = \int d^3x \Psi^{\dagger}\frac{\lambda_i}{2}\Psi Q^Q_i = \int d^3x \Psi^{\dagger}\frac{\lambda_i}{2}\gamma_5\Psi$$

commute with the QCD Hamiltonian $[Q^{V,A}_i, H_{QCD}] = 0$.

Decomposing the quark fields into left and right chirality components $\Psi_{L,R} = \frac{1}{2}(1\mp\gamma_5)\Psi$, the Lagrangian (1.1) takes the form

$$L_{QCD} = \overline{\Psi}_L(i\gamma^{\mu}D_{\mu})\Psi_L + \overline{\Psi}_R(i\gamma^{\mu}D_{\mu})\Psi_R - \frac{1}{4}G^{\alpha}_{\mu\nu}G^{\mu\nu}_{\alpha} - (\overline{\Psi}_L M^0\Psi_R + \overline{\Psi}_R M^0\Psi_L)$$

and the transformations (1.3) translate to

$$\Psi_L \rightarrow e^{-i\alpha^i_L\frac{\lambda^i}{2}}\Psi_L, \qquad \Psi_R \rightarrow \Psi_R$$

$$\Psi_R \rightarrow e^{-i\alpha^i_R\frac{\lambda^i}{2}}\Psi_R, \qquad \Psi_L \rightarrow \Psi_L$$

In the limit of vanishing quark masses, this constitutes a global $SU(3)_L \times SU(3)_R$ `chiral symmetry` in flavor space: left- and right-handed fields do not mix and preserve their 'handedness' in strong interactions.[1]

To summarize, massless QCD is symmetric under the group

$$SU(3)_{color} \times SU(3)_L \times SU(3)_R \times U(1)_V \tag{1.5}$$

Since the `explicit` breaking of chiral symmetry by the current quark masses is very small on hadronic scales (m_u, $m_d \simeq 5$ MeV/c^2 << $m_N \simeq 1$ GeV/c^2), the predictions emerging from chiral symmetry would naively be expected to hold rather accurately in the physical world. E.g., since for massless fermions the helicity and parity eigenstates

[1] For completeness, we shall mention that the 'classical' Lagrange density 1.1 exhibits two more symmetries which are broken on the quantum level. At the classical level, massless QCD is `scale invariant` under a scale transformation in Minkowski space, $x^{\mu} \rightarrow x^{'\mu} = \lambda x^{\mu}$, resulting in a conserved dilation current $j^{\mu}_D = x_{\nu}T^{\mu\nu}, \partial_{\mu}j^{\mu}_D = T^{\mu}_{\mu} = 0$ where $T^{\mu\nu}$ denotes the energy-momentum tensor. Introduction of a scale Λ breaks scale invariance, and the dilation current is no longer conserved. Including finite quark masses, the trace of the energy-momentum tensor becomes, to lowest order in α_s:

$$T^{\mu}_{\mu} = -\frac{9}{8}\frac{\alpha_s}{\pi}G^a_{\mu\nu}G^{\mu\nu}_a + \overline{\Psi}M^0\Psi \tag{1.4}$$

In addition to this `trace anomaly`, classical QCD is symmetric under global UA(1) transformations $\Psi \rightarrow e^{-i\alpha\gamma_5}\Psi$. The breakdown of this symmetry on the quantum level leads to the so-called `axial anomaly`.

coincide, degenerate hadronic isospin multiplets of opposite parity are anticipated. However, such parity doublets are not observed. The mass splitting of scalar and pseudoscalar as well as vector and axialvector mesons is interpreted as a consequence of `dynamical` breaking of chiral symmetry: the physical vacuum state $|0>$ is not invariant under chiral transformations; while the axial charges still commute with the QCD Hamiltonian, the axial charge of the vacuum is nonvanishing: $Q_i^A|0>\neq 0$. The symmetry group Eq. 1.5 is reduced to

$$SU(3)_{color} \times SU(3)_V \times U(1)_V$$

where the global SU(3) symmetry yields isospin conservation. The dynamical breaking of chiral symmetry by the QCD vacuum manifests itself in the appearance of 8 nearly-massless Goldstone Bosons (pions, kaons, eta) with strongly reduced interactions at low energies (i.e. strongly reduced scattering length [9]).

An order parameter measuring the strength of the spontaneous symmetry breaking is the quark condensate [10]

$$\langle\overline{\Psi}\Psi\rangle = \langle\overline{\Psi}_L\Psi_R + \overline{\Psi}_R\Psi_L\rangle$$

The Gell-Mann-Oakes-Renner relation [11] relates the pion mass to the quark condensate and bare quark masses (which can be regarded as a measure of the explicit symmetry breaking):

$$m_\pi^2 f_\pi^2 = -2\frac{m_u + m_d}{2}\langle\overline{\Psi}\Psi\rangle$$

Inserting the value of the pion decay constant $f_\pi = 93$ MeV$\sim \frac{1 \text{ GeV}}{4\pi}$ yields an estimate $\langle\overline{\Psi}\Psi\rangle = -(240 \text{ MeV})^3 = -1.8 \text{ fm}^{-3}$, which may be interpreted as the density of virtual quark-antiquark pairs in the vacuum (the negative sign, of course, relates to the difference between the physical and the hypothetical "empty" vacuum).[2]

1.2 Hot and dense hadronic matter

The formation of strongly interacting matter in heavy-ion collisions allows to study experimentally the phase structure of QCD. At high temperature and density, a transition from a strongly interacting gas of hadrons to a phase of deconfined quarks and gluons, the so-called quark-gluon-plasma (QGP), is predicted. Along with the deconfinement transition, also the restoration of chiral symmetry is expected. Fig. 1.1 shows results for the order parameters of the two phase transitions from calculations in discretized Euclidean space-time. On the left, the temperature dependence of the Polyakov loop[3]and the associated susceptibility are shown. The Polyakov loop is related to the free energy F of a

[2]Similarly, as a consequence of the breaking of scale invariance, gluons condense and give rise to a nonvanishing vacuum expectation value $\langle\frac{\alpha_s}{\pi}G^2\rangle$ =0.012 GeV^4 [12].

[3]Strictly speaking, this quantity is an order parameter only for pure gauge theory, i.e. infinite quark masses.

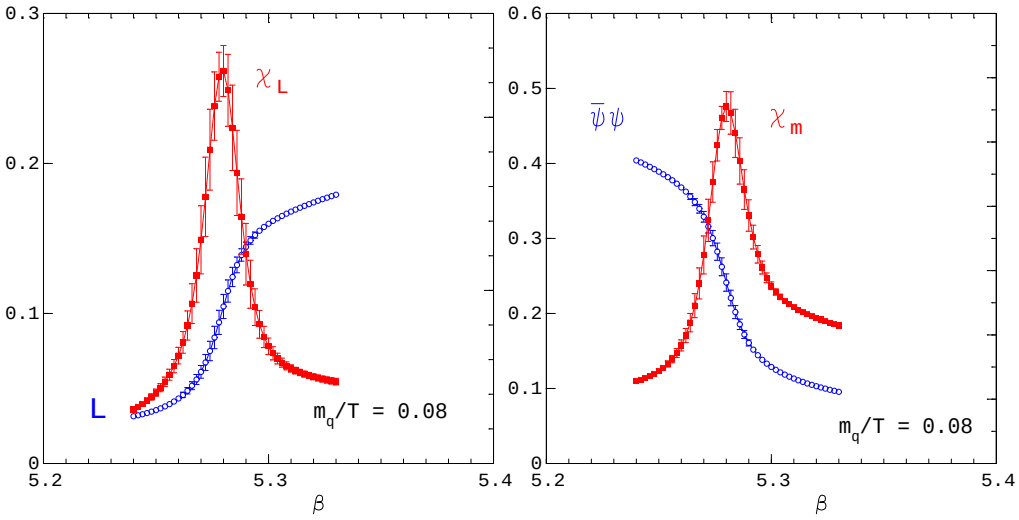

Figure 1.1: Temperature dependence of the Polyakov loop (left panel) and the quark condensate (right panel), along with the associated susceptibilities, obtained from 2-flavor lattice QCD [15].

color test charge placed in the medium: $P = exp(-F/T)$ [13] [14]. In the confined phase, F is infinite and P zero: an isolated color charge can not exist. As deconfinement sets in, F takes a finite value, resulting in an increase of P. The right hand plot presents the drop of the quark condensate at the phase transition, indicating chiral symmetry restoration. The agreement of the critical temperatures for both phase transitions, indicated by the susceptibility maxima, is a remarkable and so far non-understood coincidence.

These lattice calculations are carried out at net baryon density 0 and close to the critical temperature. Model independent results for the dependence of the quark and gluon condensates on the baryochemical potential μ can be obtained in chiral perturbation theory. It turns out that modifications of the condensates occur already at low temperatures and small baryon densities. As the temperature increases from 0, pions are thermally excited first, since they represent the lightest hadrons. The leading correction to the vacuum condensate $< \overline{\Psi}\Psi >$ is given by

$$\frac{<< \overline{\Psi}\Psi >>}{< \overline{\Psi}\Psi >} =\simeq 1 - \frac{\Sigma_\pi \rho_\pi^s(T)}{f_\pi^2 m_\pi^2}$$

where the thermal average $<< \overline{\Psi}\Psi >>$ is given as function of the pion σ-term $\Sigma_\pi = 69$ MeV, and the scalar density ρ_π^s at given temperature. At vanishing temperature and finite baryon densities, nucleons give the dominant correction to $< \overline{\Psi}\Psi >$

$$\frac{<< \overline{\Psi}\Psi >>}{< \overline{\Psi}\Psi >} =\simeq 1 - \frac{\Sigma_N \rho_N^s(\mu_N)}{f_\pi^2 m_\pi^2}$$

where $\rho_N^s(\mu_N)$ is the nucleon scalar density at $\mu_N = 3\mu_q$.

In Fig. 1.2 [16], we present a sketch of the proposed phase diagram of nuclear matter in the plane of temperature versus baryochemical potential (which is a measure of the net baryon density). The thermodynamic parameters can be experimentally varied via the c.m.s. energy of the colliding nuclei, the nuclear mass and the impact parameter. State of the art lattice calculations give for the phase transition at μ=0 a critical temperature between T_c=192±7 MeV [17] and T_c=151±3 MeV [18] and a energy density of ϵ_c= 0.7±0.2 GeV/fm^3 [19]. The band indicates a guess for the phase boundary between the deconfined QGP and the hadronic phase. The 'chemical freezeout', determined experimentally from the relative particle abundances, characterizes the stage where inelastic collisions between particles in the fireball cease and the particle composition is fixed. The 'thermal freezeout' refers to the stage where elastic collisions are no longer supported as the mean free path of the hadrons exceeds the size of the fireball. The measured temperatures there are inferred from the momentum distributions of the different hadron species.

Clearly, the thermalized hadrons emitted from the fireball carry only little information on the early stages of the fireball evolution and possible QGP formation. Because of their negligible final-state interactions with the hadronic environment, electromagnetic

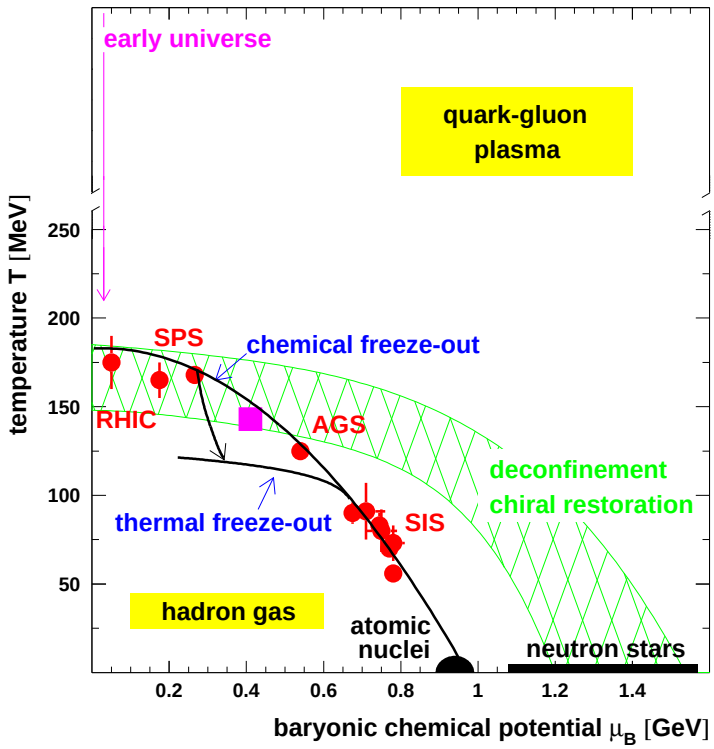

Figure 1.2: QCD phase diagram [16]. The yellow band sketches the uncertainties for the location of the phase boundary. The experimentally determined freeze-out curves are indicated.

probes - dileptons, dimuons or photons - are considered ideal to assess the high-density/-temperature regions formed in the early stages of the collision. The experimental spectra of the dilepton invariant mass are always a superposition of different stages [20]:

1 Before the nuclear surfaces actually touch, dileptons are produced through coherent bremsstrahlung. This part populates very low transverse momenta.

2 Within the first 1 fm/c of the nuclear overlap, the excited hadronic system is far from thermal equilibrium. The 'pre-equilibrium' dilepton radiation emitted at this stage mostly consists of hard processes such as Drell-Yan annihilation, leaving its trace mainly at large invariant masses >3 GeV/c^2.

3 Following deconfinement and rapid thermalization, dileptons are produced in the partonic phase via $q\bar{q}$ annihilation with characteristic parameters reflecting the early temperature history of the system.

4 After cooling and confinement of the partons into a hot hadron gas, dileptons are created in pion and kaon annihilation processes.

5 Finally, beyond the freeze-out stage, the remaining sources are hadronic resonance and Dalitz decays, mostly from π^0, η and ω mesons.

The third and fourth stage are relevant for deconfinement and chiral symmetry restoration. With respect to invariant mass, one can distinguish three regions:

1 The low-mass region with M_{ll} <1 GeV/c^2, governed by the light quark sector of u, d, s quarks, where signals of chiral restoration manifest themselves in terms of medium modification of light hadrons.

2 The high-mass region above m$_{J/\Psi}$ =3.1 GeV/c^2. Through heavy quarks one might hope to become sensitive to features of deconfinement, e.g. via the dissolution of bound hadron states (J/Ψ,Υ) due to screening of the confining potential in the QGP.

3 The intermediate mass region, where semileptonic decays of open charm, i.e. pairwise produced $D\bar{D}$ mesons, as well as prompt dileptons contribute. Thermal radiation from the plasma is expected to be continuum-like and dominated by $q\bar{q}$ annihilation [21].

1.3 Low-mass dilepton pairs: theoretical aspects

In the low-mass region, apart from π^0 and η Dalitz decays, the dilepton spectra are dominated by the light vector mesons: hadronic 2-body annihilation processes are enhanced

through the formation of intermediate vector resonances ρ, ω, ϕ which directly couple to l^+l^- pairs. The invariant mass of the lepton pair directly reflects the `spectral function`, the mass distribution of the vector meson, at the moment of the decay and allows to assess modifications of the hadron mass and decay width with respect to the vacuum. The ρ is of particular interest. Due to its small vacuum lifetime of 1.3 fm/c [6], all ρ mesons produced in the collision decay inside the fireball. In contrast, the ω and ϕ meson are less sensitive to medium-induced changes of hadron properties: with lifetimes of 23 and 44 fm/c respectively, corresponding to about 2-4 times the life time of the fireball, most of the decays occur in vacuum and cover the smaller in-medium contribution.

The dilepton production rate in a hadronic medium can be calculated as [22, 23]

$$\frac{d^8N_{l^+l^-}}{d^4xd^4q} = \frac{dR_{l^+l^-}}{dq^4} = L_{\mu\nu}(q)W^{\mu\nu}(q)$$

through contraction of the lepton tensor $L_{\mu\nu}$, given to lowest order in α by

$$L_{\mu\nu} = -\frac{\alpha^2}{6\pi^3M^2}(g_{\mu\nu} - \frac{q_\mu q_\nu}{M^2})$$

and the hadronic tensor $W_{\mu\nu}$, in which the properties of the medium are contained, defined as the thermal average over the electromagnetic iso-vector current-current correlation function:

$$W^{\mu\nu}(q) = \int d^4x e^{-iqx}\langle\langle j^{em}_\mu j^{em}_\nu\rangle\rangle$$

It can be connected to the one-particle irreducible photon self-energy

$$-2Im\,\Pi^{\mu\nu}_{em} = (e^{q_0/T} - 1)W_{\mu\nu}$$

so that the thermal rate becomes

$$\frac{dR_{l^+l^-}}{dq^4} = -\frac{\alpha^2}{\pi^3M^2}\frac{1}{e^{q_0/T}-1}Im\,\Pi_{em}(q_0,\vec{q})\ . \tag{1.6}$$

The self energy Π_{em} is dominated by the vector correlator $\Pi_V^{0\,\mu\nu}$ which is related to the vector spectral function ρ_V

$$\frac{1}{\pi}Im\,\Pi_V^{0\,\mu\nu}(q) = (q^2g^{\mu\nu} - q^\mu q^\nu)\rho_V^0(q^2)$$

but also receives a contribution from the axialvector correlator

$$\frac{1}{\pi}Im\,\Pi_A^{0\,\mu\nu}(q) = (q^2g^{\mu\nu} - q^\mu q^\nu)\rho_A^0(q^2) - q^\mu q^\nu f_\pi^2\delta(q^2 - m_\pi^2)$$

The vacuum spectral functions ρ^0 are related to physical processes. The vector spectral function can be obtained from e^+e^--annihilation into an even number of pions while ρ_A^0 can be extracted from data on τ-decay into a ν_τ-neutrino and an odd number of pions.

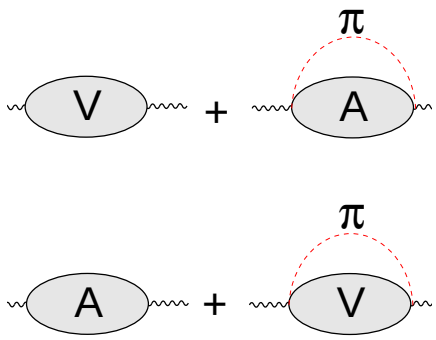

Figure 1.3: Diagrammatic representation of the mixing of vector and axialvector correlators in a heat bath of pions [20].

Chiral symmetry dictates a relationship between the vector and axialvector sector which is encoded in the Weinberg sum rules [24]

$$\int ds(\rho_V^0(s) - \rho_A^0(s)) = f_\pi^2$$

$$\int sds(\rho_V^0(s) - \rho_A^0(s)) = 0$$

In the hot hadronic medium, the onset of chiral symmetry restoration is realized in the mixing of axial and vector correlators due to the presence of thermally excited pions (Fig. 1.3). To lowest order in temperature, one obtains [25] the model independent 'mixing theorem' of vacuum correlators, which can be translated to the spectral densities:

$$\rho_V(p^0, \vec{p}, T) = (1-\epsilon)\rho_V^0(s,T) + \epsilon\rho_A^0(s,T)$$

$$\rho_A(p^0, \vec{p}, T) = (1-\epsilon)\rho_A^0(s,T) + \epsilon\rho_V^0(s,T) \ .$$

The mixing coefficient ϵ can be evaluated for the chiral limit [25]

$$\epsilon = \frac{T^2}{6f_\pi^2} \ .$$

Chiral symmetry is fully restored for $\epsilon = \frac{1}{2}$, corresponding to T≈160 MeV, which reasonably agrees with T_C from lattice calculations. In this limit the spectral functions are fully degenerate. More generally, the Weinberg sum rules can be formulated for the medium [26]:

$$\int dq_0^2(\rho_V(q_0) - \rho_A(q_0)) = 0$$

$$\int dq_0^2 q_0^2(\rho_V(q_0) - \rho_A(q_0)) = 0 \ .$$

They are trivially solved in the full mixing case. In the dense medium, the mixing receives a non-negligible contribution from pions originating from the 'pion cloud' surrounding the nuclei [27, 28].

1.4 The CERES results

The history of dilepton reconstruction in hadronic collisions dates back 30 years. Early measurements of vector mesons in pp, pA and πA collisions revealed an unexpected continuous dilepton spectrum for masses below 600 MeV/c^2 and sparked much theoretical interest and further experimental effort. The effect turned out to be due to the so-far underestimated η-Dalitz decay. Dilepton spectra were proposed as a signature for QGP formation [21].

The Helios-1/NA34 collaboration at CERN was first to measure e^+e^- and $\mu^+\mu^-$ production in p-Be collisions. After these early measurements, the dilepton sector was divided among different CERN experiments: low-mass dielectrons are the domain of CERES/NA45, while dimuons were measured by NA34/Helios-3 (with S beams), NA38/NA50 (heavy ion collisions) and NA60 (light ions). An important difference between CERES and the dimuon experiments is the accessible kinematic region: for dielectrons, due to the negligible mass of the electron compared to the muon, there is no intrinsic cutoff towards small values of the transverse mass m_T, and the CERES coverage of the region of small pair transverse momenta is much more complete than for the dimuon experiments. For the assessment of effects of chiral symmetry restoration this kinematic region is favorable, since the medium modifications of the dilepton producing processes are expected to be stronger at low p_T.

The CERES/TAPS collaboration reproduced the p-Be measurements with much greater

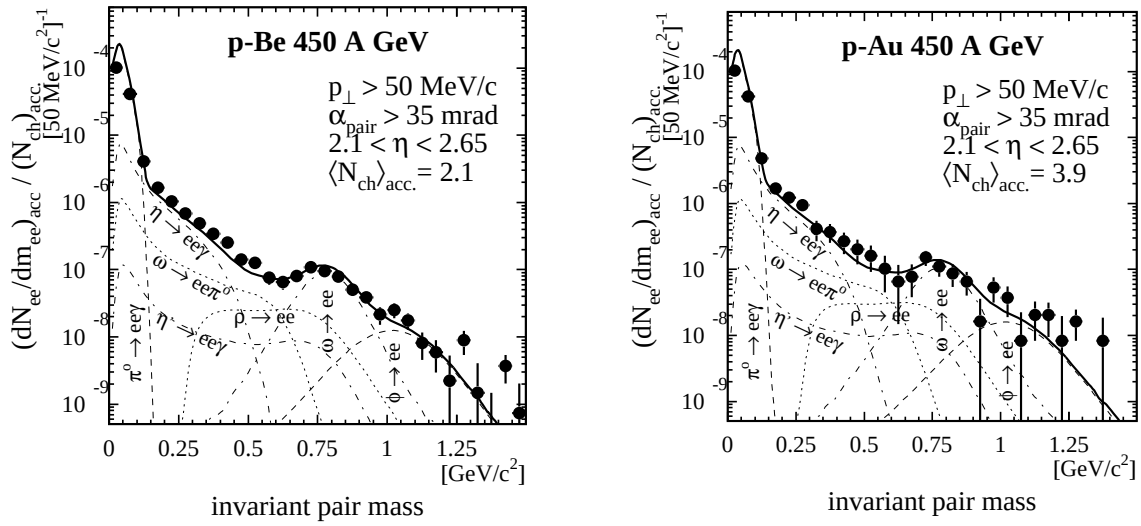

Figure 1.4: CERES inclusive e^+e^- mass spectra of 450 GeV p-Be and p-Au collisions [29]. Plotted is the number of electron pairs per charged particle into the acceptance. Contributions from various hadron decays as expected from p-p collisions are shown together with their sum (thick line).

precision and carried out first dilepton measurements in p-Au collisions in 1993 [29, 30]. The results are presented in Fig. 1.4. The observed yield is completely consistent with the hadronic cocktail: it can be described by the branching ratios of the known leptonic and semi-leptonic hadron decays and the production cross sections observed in *pp* collisions extrapolated to pA.

The situation is drastically different in nucleus-nucleus collisions. The dielectron yield observed in S-Au (1992) [31] and Pb-Au collisions (1995/1996) [32] at 200 A GeV/c and 158 A GeV/c, respectively, presented in Fig. 1.5 significantly exceeds the *pp* extrapolation. While the π^0 Dalitz peak is well reproduced by the hadronic cocktail, the dip expected in the η-Dalitz region up to the ρ/ω peak is not observed. The integrated pair yield above 200 MeV/c^2 exceeds the hadronic cocktail by a factor of 5.0±0.7(stat.) for S-Au collisions. For the combined 95/96 data, an enhancement factor of 2.73±0.25(stat.) is observed. These results met tremendous interest from theory, and the interpretation of the enhancement and its possible connection to the restoration of chiral symmetry in the hadronic or pre-hadronic phase is the subject of ongoing theoretical investigations.

To improve the momentum and therewith the mass resolution of the spectrometer, resulting in better sensitivity in the region of invariant masses between the ω and ϕ peak, the CERES experiment was equipped with a Time Projection Chamber (described in chapter 2). The first experimental run after the upgrade was performed in 1999 at a beam energy of 40 GeV/c^2 (Pb on Au), probing the phase diagram in a region of higher net baryon density. An enhancement factor of 5.61±1.4(stat.) was measured [33]. In 2000, the first run with TPC measuring Pb on Au collisions at the full SPS energy of 158 GeV/c was carried out. The analysis of these data is the objective of this thesis.

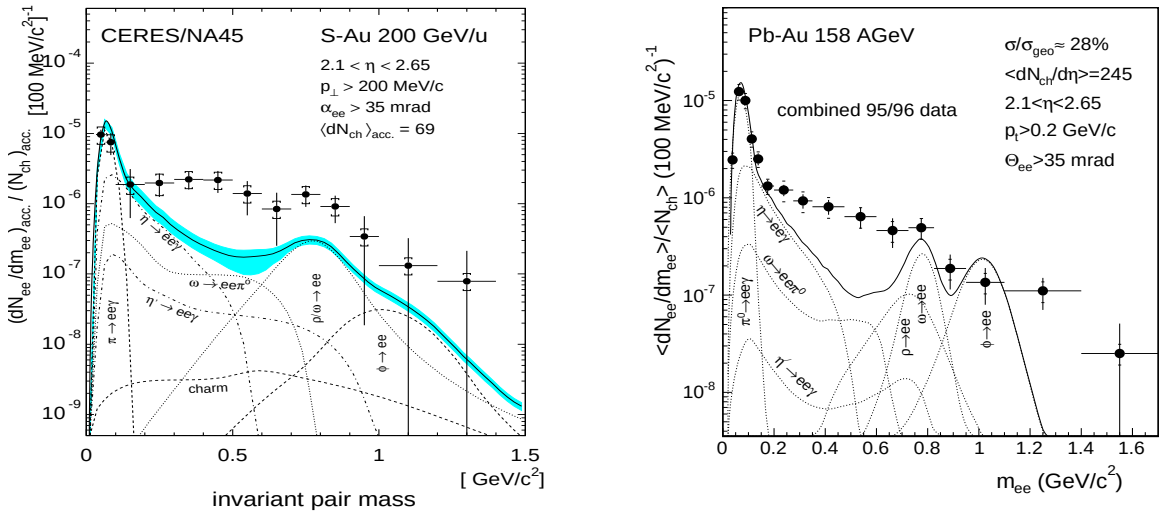

Figure 1.5: CERES inclusive e^+e^- invariant mass spectra of 200 GeV/c S-Au [31] and 158 GeV/c Pb-Au collisions (combined '95 and '96 runs) [32], compared to the hadronic cocktail.

2 The CERES detector

The CERES (Cherenkov Ring Electron Spectrometer) detector was conceived and built for the measurement of low-mass electron pairs at ultra-relativistic energies. It is axially symmetric around the beam axis and covers the full azimuth. The spectrometer was installed in 1990 at the H8 beam line of the CERN SPS North Area and started operation in 1991. It covers the pseudorapidity[1] region 2.1< η <2.65, close to midrapidity (y_0=2.91 for the maximum SPS Pb beam energy of 158 AGeV/c). The initial setup consisted of two Ring Imaging Cherenkov (RICH) detectors, placed before and after an azimuthally deflecting magnetic field (RICH1 was essentially field-free), and a silicon radial drift detector. In this setup, electron identification and tracking was provided by the RICH detectors, the silicon detector was used for vertex reconstruction. The momentum was determined by the deflection of the charged particles between RICH1 and RICH2. The measurements of p-Be, p-Au and S-Au collisions [29, 30, 31] were carried out with this configuration. In 1994 and 1995, a first major upgrade of the detector was performed to cope with the high particle multiplicities encountered in Pb-Au collisions [34, 35]. A doublet of silicon drift detectors [36] replaced the single silicon detector to enable precise charged-particle tracking before RICH1 and a multi-wire proportional counter with pad readout (Pad Chamber) was added downstream of RICH2 mirror for additional tracking. In the 1998 detector upgrade [37], the Pad Chamber was removed and a radial Time Projection Chamber (TPC), embedded in a dipole magnet, was added. The now obsolete magnet coils between RICH1 and RICH2 were switched off. The TPC allows high-precision tracking of charged particles and provides improved momentum and mass resolution and additional lepton and hadron identification. The data analyzed in this work were taken with this latest setup, presented in Fig. 2.1.

2.1 Target region

The target region, sketched in Fig. 2.2, comprises the target proper and various detectors for beam definition used in the trigger system. The beam enters the target area via an evacuated Al tube that reaches until a few millimeters short of the target and is

[1] The pseudorapidity of a particle is defined via the polar angle θ with respect to the beam axis: η =-ln tan $\frac{\theta}{2}$. For ultra-relativistic particles with momenta p>>m, η approaches the rapidity y, with sinh$y = \beta\gamma = \frac{p}{m}$.

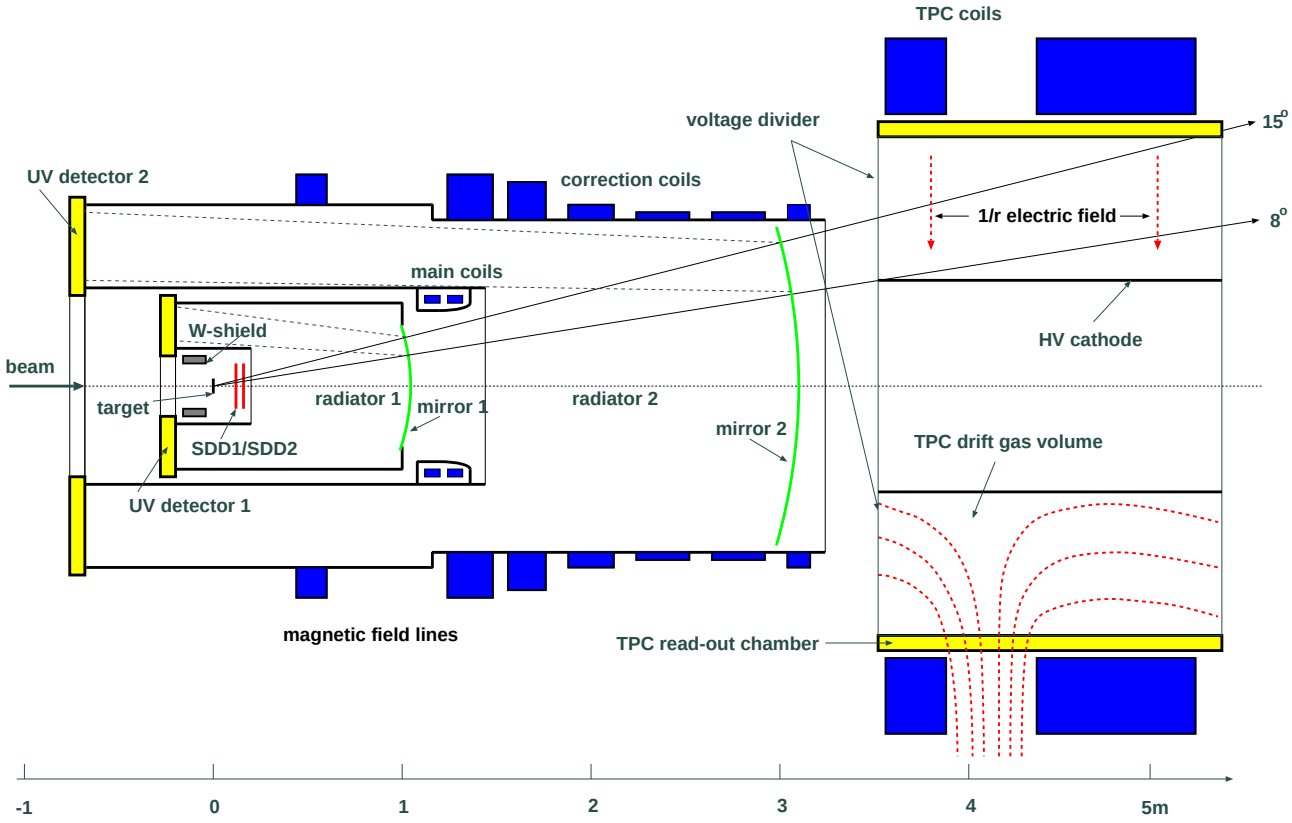

Figure 2.1: The CERES experimental setup in 2000.

sealed by a thin mylar window. To minimize the radiation length into the detector acceptance and thus the amount of electrons from γ conversions, which are background to the measurement of electrons from meson decays, the target is segmented into 13 disks spaced uniformly by about 2 mm on the beam axis. Each disk has a diameter of 600 μm and a thickness of 25 μm. The target is housed in a cylindrical tungsten cylinder, to shield the UV-detectors from charged particles emerging from the target in backward direction.

2.2 Trigger

The trigger [38] provides fast recognition and selection of interactions in the gold target. It provides the signal to start the data acquisition and open the TPC gating grid. The minimum bias trigger (MBT) is defined by 3 beam counters (BC), gas Cherenkov detectors consisting of thin Al-mylar mirrors positioned along the beam axis to reflect the Cherenkov light into photomultiplier photocathodes. BC1 is placed 60 m upstream from the target, BC2 and BC3 within the target area, upstream and downstream from the target, as shown in Fig. 2.2. The coincidence of BC1 and BC2 defines a beam trigger, the veto of BC3 identifies beam-target interactions: MBT = BC1 $\times$ BC2 $\times$ $\overline{\text{BC3}}$.

A direct measurement of the impact parameter of the collision is not possible. However, based on the assumption that collisions with smaller impact parameter will produce more particles, one can use the charged particle multiplicity to extract the impact parameter and classify an event. For the selection of central interactions, a scintillation multiplicity counter (MC), covering midrapidity, was used to trigger on events with high charged particle multiplicity: the light yield is proportional to the number of charged particles traversing the scintillator. The centrality trigger (CT) was defined by coincidence of the minimum bias trigger and a signal above threshold from the MC: CT = MBT $\times$ MC(>bias).

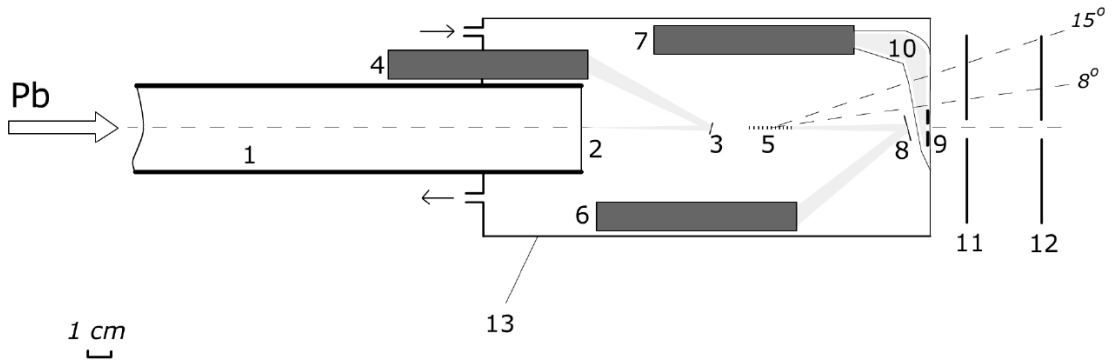

Figure 2.2: Scheme of the target area: 1 - carbon vacuum pipe, 2 - aluminum entrance window, 3 - BC2 mirror, 4 - BC2 photo multiplier (PMT), 5 - segmented gold target, 6 - BC3 PMT, 7 - MC PMT, 8 - BC3 mirror, 9 - MC scintillator, 10 - Al-mylar light guide, 11 - SDD1, 12 - SDD2, 13 - gas volume of Cherenkov detectors BC2 and BC3

2.3 Silicon drift detectors

The silicon drift detectors (SDD) [39] fulfil several purposes in the electron analysis strategy: (i) event reconstruction: the SDDs locate the interaction vertex within the segmented target, improving thereby the momentum resolution of the spectrometer; (ii) tracking: the SDDs provide a precise measurement of two points of the trajectories of charged particles emerging from the primary interaction vertex; (iii) background rejection of close electron pairs from conversions or Dalitz decays, either resolving two close tracks or detecting a double pulse-height signal.

Semiconductor detectors operate as solid state ionization chambers. A charged particle traversing a semiconducting crystal excites electron-hole pairs. The band gap between valence and conducting band in silicon is E_g = 1.12 eV, the average energy to create an electron-hole pair 3.6 eV [40]. Charge collection is accomplished by an electric field, creating a depleted zone in the junction between a p- and n-doted layer.

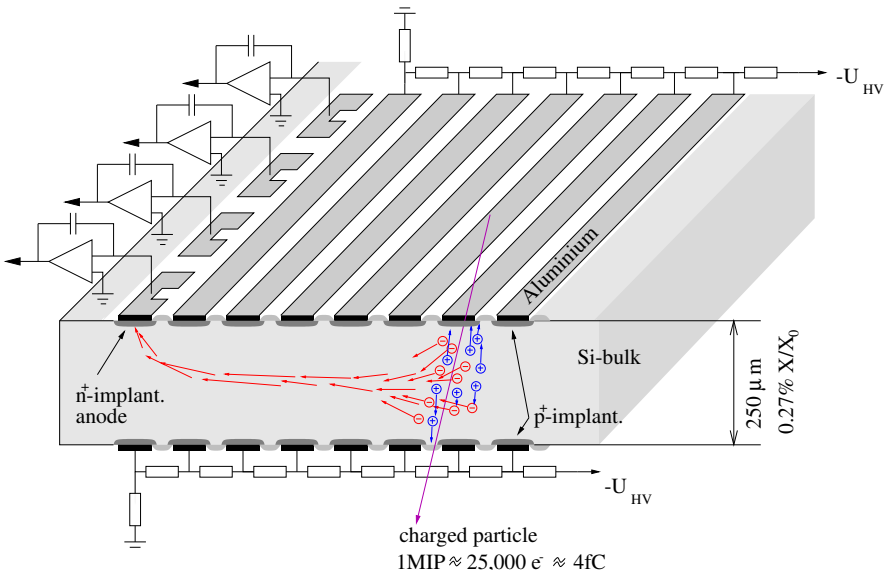

Figure 2.3: Schematic view of a radial slice of the Silicon drift detector

The SDD telescope [41] consists of two cylindrical SDDs with an active area of 55 cm^2 cut out of a 4 in. diameter silicon wafer 280 μm thick. The detectors are centered on the beam axis, approximately 10 and 14 cm downstream from the target as shown in Fig. 2.2, covering the full azimuthal acceptance and the pseudorapidity region $1.6 < \eta < 3.4$. There is a small hole in the center of each detector to allow the passage of the beam. The electrostatic drift field is provided by means of concentric p^+ electrodes, suitably biased by an implanted voltage divider, as shown in Fig. 2.3. The drift field transports the ionization electrons radially outward to an array of 360 anodes located at the periphery of each detector. The drift time measures the radial coordinate of the particle's interaction point. Charge sharing between contiguous anodes allows to resolve the azimuthal coordinate. To improve resolution, adjacent anodes are interlaced to optimize the charge sharing. The maximum drift time for a field of about 700 V/cm is approximately 4 μs.

2.4 Ring Imaging Cherenkov Detector

The principal device for electron identification in the CERES experiment is the Ring Imaging Cherenkov (RICH) detector system [42], consisting of two separate subdetectors RICH1, RICH2. With the advent of the TPC, the magnetic field in the RICH detectors was switched off and charged particles traverse RICH1 and RICH2 undeflected, allowing combined operation of the subdetectors.

Cherenkov radiation is emitted whenever a charged particle traverses a material with a velocity β exceeding the phase velocity of light c/n in the material with index of refraction n. The electromagnetic radiation, real photons in the visible and UV energy range, is

emitted on a 'Mach' cone with opening angle [43]

$$\cos\,\theta_C = \frac{1}{\beta n}\ . \tag{2.1}$$

The threshold behavior follows from this relation, requiring $\cos\theta_C \leq 1$, as $\beta_{Thr} = 1/n$, or equivalently

$$\gamma_{Thr} = \sqrt{\frac{1}{1-\beta_{Thr}^2}} = \sqrt{\frac{1}{1-1/n^2}}\ .$$

For high velocities, we can derive the asymptotic behavior setting $\beta = 1$ in Eq. 2.1. It follows the asymptotic angle θ_C^∞:

$$\cos\ \theta_C^\infty = 1/n$$

$$\theta_C^\infty \approx \sin\theta_C^\infty = \frac{1}{\gamma_{Thr}}\ .$$

The number of photons scales as $\sin^2\theta_C$, giving a total of N detected photons for a radiator of length L

$$N = N_0 L z^2 \sin^2\theta\ . \tag{2.2}$$

Here, z is the charge of the particle. The `figure of merit` N_0 is a measure of detector characteristics (e.g. properties of the radiator and mirror, quantum efficiency and the bandwidth of detectable photon energies [44]). N is the mean number of photons, the emission follows Poissonian statistics. For the asymptotic case, we have

$$N_\infty = \frac{N_0 L}{\gamma_{Thr}^2}\ .$$

For non-asymptotic particles, the number of photons is lower:

$$\frac{N}{N_\infty} = \frac{\sin^2\theta_C}{\sin^2\theta_C^\infty}\ . \tag{2.3}$$

In mirror-focused RICH detectors [46] the emission pattern of the radiation is used for particle identification: a spherical mirror projects the light emitted on a Mach cone onto a ring with radius

$$r = F\sqrt{\frac{1}{\gamma_{Thr}^2} - \frac{1}{\gamma^2}} \tag{2.4}$$

in the mirror focal plane (focal length F), as sketched in Fig. 2.4 for the CERES experiment. In the CERES RICH, methane at atmospheric pressure ($n-1 \simeq 0.444\cdot 10^{-3}$) [6] is used as radiator, resulting in a Cherenkov threshold of $\gamma_{Thr} \simeq 32$. For this reason electrons, due to their small mass, emit Cherenkov light already at very small momenta. Only a small fraction of the heavier particles, mainly muons and pions with momenta exceeding 4 to 5 GeV/c, also emit Cherenkov light, such that electrons are the dominating

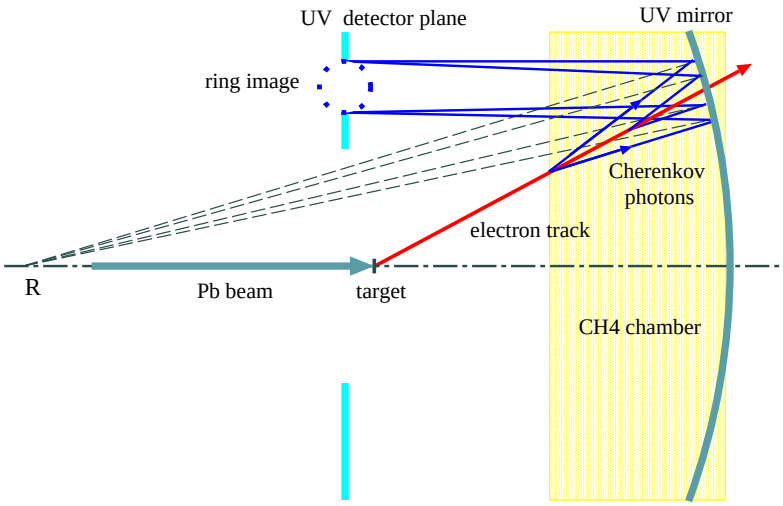

Figure 2.4: Schematic view of the CERES RICH detector [45]

source of Cherenkov radiation[2]. For momenta of the order of 1 GeV/c up accessible to the spectrometer, the Cherenkov angle for electrons takes the asymptotic value θ_C^{∞} =0.031 rad, often sloppily referred to as `asymptotic radius`. In order to keep the radiation length as low as possible, RICH1 mirror is a very thin aluminum-coated laminated carbon-fiber structure ($X/X_0 = 1.4\%$). Unfortunately, the attempt failed to replace the conventional 6 mm glass mirror of RICH2 by a lighter structure [45] in time for the 2000 runs, and with a radiation length of $X/X_0 = 4.5\%$ this constitutes the thickest individual component of the detector. The two readout planes (UV1, UV2) consist of 2-dimensional position-sensitive gas detectors with ∼50000 readout pads each [47]. The photon conversion region, operated with a mixture of He/CH_4 (6%) and TMAE as photosensitive agent, is separated from the radiator volume by UV-transparent windows. In order to achieve sufficient partial pressure of the TMAE, the entire RICH system is kept at a temperature of 50 °C. For charge amplification, the conversion region is followed by two parallel-plate avalanche stages and a multi-wire proportional chamber.

2.5 Time Projection Chamber

The Time Projection Chamber [48] (Fig. 2.5) is located immediately downstream of RICH2, 3.8 m from the target. It has an active length of 2 m, an inner radius of 48.6 cm and an outer radius of 130.8 cm. As all the other detectors in the experiment, the TPC has cylindrical geometry. It covers the range $2.1 < \eta < 2.65$ in pseudorapidity. Charged particles traversing the TPC volume ionize the detector gas. The ionization electrons drift in the radial ($1/r$) electric field between the cylindrical inner electrode at high voltage

[2]hence the notion 'hadron-blind detector'

(-29.2 kV) towards the grounded cathode wires. Each of the 16 readout chambers has three wire planes with wires running in azimuthal direction: gating grid, cathode wire plane, and anode wire plane. The arriving charge cloud passes the gating and cathode wire planes and produces an avalanche close to the anode wires in the amplification region, inducing a signal on the Chevron-type cathode pads. The Chevron design of the pads was adopted due to its efficient charge sharing, which allows reconstruction of the azimuthal ϕ coordinate with high precision, and small differential non-linearities [49]. Each particle track is sampled with up to 20 space point measurements, resulting in $48 \times 16 \times 20 = 15360$ readout channels. Each channel is equipped with low-noise electronics [50] which samples the analog signals with 8-bit ADC in 256 time bins per channel.

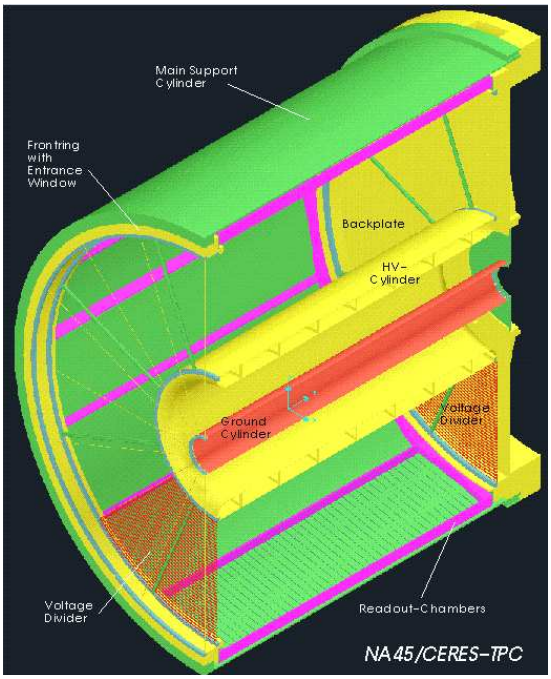

Figure 2.5: The CERES TPC.

The particle momentum is measured by the curvature of the reconstructed track in the magnetic field of two large coils of a warm magnet surrounding the TPC, with currents (up to 4160 A) running in opposite direction. The magnetic field lines in the r-z plane are indicated in Fig. 2.6, upper panel. The dash-dotted line marks the acceptance in polar angle θ of the upstream spectrometer as well as of the TPC (location indicated by the short-dashed rectangle). The lower panel of Fig. 2.6 shows the radial and longitudinal field components, for both the inner and outer extremes of the θ acceptance, as function of the z-coordinate. Charged particles traversing the magnetic field are, to first order, only deflected in azimuthal direction. The bottom plot presents the trajectory of a singly positively charged particle with momentum 1 GeV/c on the surface of a cone with angle θ again for the minimum and maximum θ accepted. In addition, the quantity $r \cdot \mathrm{d}\phi/\mathrm{d}z$ is

shown, which determines the extent of the primary ionization trail in direction of the wires of the read-out chambers. This quantity needs to be multiplied with the length $\Delta z = 4$ cm covered by each read-out pad to estimate the limit in intrinsic point resolution due to the track deflection. The kinks at $z \approx$1.2 m are due to the two super-conducting magnet coils located between the two RICH counters (inoperative during the 2000 run), the strong bend at $z \approx$4.2 m, i.e. at the level of the TPC, represents the region of maximal field strength produced by the new coils.

The drift gas mixture, Ne,CO_2 (20%), was carefully chosen to achieve 1.) good position resolution and tracking performance, minimizing diffusion, Lorentz angle and radiation length and maximizing the primary ionization and 2.) a high drift velocity, to avoid any limitation of the primary interaction rate by the drift time within the TPC [37].

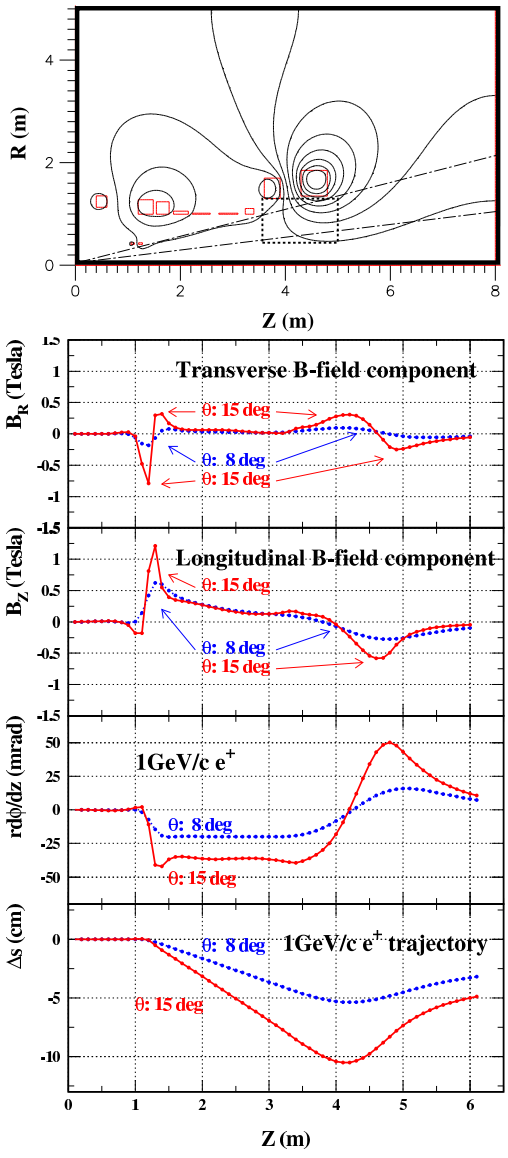

Figure 2.6: Magnetic field of CERES. Upper panel: Field lines. The active volume of the TPC is indicated by the dashed rectangle. The superconducting magnet at $z \approx$1.2 m was inoperative during the 2000 runs. Lower panel: field components transverse to and in beam direction (top and next to top) as well as a displacement from an undeflected track on the surface of a cone with angle θ of a 1 GeV/c singly charged particle (bottom). In the next to bottom plot is shown the length of the arc projected into the $r-\phi$ plane per unit length in z, $r-\mathrm{d}\phi/\mathrm{d}z$.

3 Data analysis

The data analyzed in this thesis were taken at CERN SPS in autumn 2000 with a 158 AGeV Pb beam on a Au target. The data sample comprises $33{\cdot}10^6$ events. The majority of the data were recorded triggering on the most central 7% of the geometrical cross section σ_{geom}. In addition, $3{\cdot}10^6$ events with $\sigma/\sigma_{geom} = 20\%$ and about $0.5{\cdot}10^6$ events with minimum bias trigger were taken. For calibration purposes short runs were interspersed, with laser tracks into the TPC, at lower beam intensity, without the target and without magnetic field (consider [51] for a complete list of runs). Due to occasional discharges in the RICH readout chambers, not both RICH1 and RICH2 were operative all the time. This reduces the available data sample for the electron pair analysis to $23{\cdot}10^6$ events.

The SPS provided ion beams as 4 s bursts every 19 s with typically 10^6 ions per burst. Events acquired within each burst were stored in one data file. The raw data comprise $\sim$ 100000 bursts managed by the CASTOR (CERN Advanced STORage manager [52]) hierarchical mass storage system at CERN. For calibration purposes, the bursts were grouped in `calibration units` of $\sim$200, representing roughly one hour of data taking.

3.1 A new approach

The identification of electrons produced in heavy ion collisions is a major experimental challenge: the hadronic background exceeds the lepton signal by 3 to 4 orders of magnitude. For the reconstruction of the correlated dilepton signal, excellent electron identification is required, which, in CERES, is prominently provided by the RICH detectors. In this thesis, a new strategy for particle identification in the RICH, proposed in [53], is applied in the dilepton analysis[1].

Before the upgrade in 1999, the CERES RICH detectors were an integral part of the tracking strategy: electron rings were reconstructed in RICH1 and RICH2 separately, and the track momentum was determined via the displacement of the ring centers between the two detectors due to the deflection of the particle in the magnetic field. In the new CERES experimental setup, the CERES radial TPC, a superior tracking detector with excellent momentum resolution, allows the reconstruction of electron `and` hadron

[1] In [54, 55] the dilepton analysis of the 2000 data was performed with the conventional RICH reconstruction.

tracks, independently of the particle identification in the RICH. On the other hand, it is conceivable to use the TPC tracks as input for the RICH ring reconstruction, as predictors for possible ring centers. In this new approach, any charged particle traversing the RICH furnishes a ring candidate. To establish criteria to distinguish between electron signal and hadron background, a detailed study of the RICH detector characteristics was carried out. The development of new techniques for RICH ring reconstruction and new criteria for electron identification is the main goal of this thesis.

3.2 Data production

Extracting physics from the signals measured by the complex detector system of a high-energy physics experiment is a sophisticated task. Before any physics information can be performed, the raw data have to be converted into a more convenient data format and the raw signals (ADC output) have to be grouped and transformed into data structures closer to the physical understanding and intuition (hits, tracks, rings, ...). This process is called `production`.

The entire data analysis proceeds in 3 major stages:

- raw data production and event reconstruction
- tracking, vertex reconstruction and RICH ring reconstruction
- dilepton analysis.

These stages are distributed over different production steps, where each step handles the output of the previous one. To extract physics information from the data, the detectors have to be calibrated and inter-calibrated. The time-dependent calibration parameters, e.g. the TPC gas properties (Lorentz angle, gas gain, ...) as function of ambient pressure and temperature, or the drift velocity in the SDD detector, are determined for each calibration unit and corrections are already applied during the raw data production. Further, increasingly precise, calibration is applied on each subsequent production step and during data analysis [57]. The CERES production chain consist of the following steps:

- step0: burstwise trigger calibration
- step1: raw data analysis, first iteration for detector calibration [48, 58]. Reconstruction of detector hits in SDD, TPC and RICH; TPC and SDD tracking, vertex reconstruction
- step2: reiteration of step1, calibration [55]
- step3c: data reduction

- step4c: partial reiteration of the step2 raw data production, comprising reconstruction of the RICH hits and a newly implemented TPC low-momentum tracking.

The combined step1 and step2 production was performed during 2 months in summer 2003 on 400 processors at the LFS batch farm [56] at the CERN Computing Center. The step2 output is organized under the form of data objects using classes from the CERES C++ COOL (CERES Object Oriented package Library) library. Since the COOL package is very complex and the step2 data volume rather large, this framework is not suitable for efficient data analysis. In order to reduce the data volume and to facilitate and speed up analysis, the step3c format was developed [57], and supplemented by step4c. The step3c and step4c output is stored on CASTOR and is also available at file servers at GSI Darmstadt.

3.2.1 Step3c

Design and implementation of the step3c software, extending the range of applicability of the original implementation described in [57], was part of this work. Step3c is not an exclusive dilepton analysis package, but provides the tools for any kind of lepton or charged hadron reconstruction (hence the appendix "c"). Indeed, a rich variety of different physics observables have been and are being analyzed with step3c, such as production of neutral pions [59], neutral and charged kaons [60] [61] as well as phase space correlations [62] like flow [63], Bose-Einstein Correlations [57] and high-p_T angular correlations [64] [65].

To allow fast access to the data, step3c strongly reduces the data volume of step2 - preserving, however, the full information relevant for any data analysis foreseen. Step3c is implemented within the ROOT [66] object oriented data analysis framework, the events are stored on ROOT trees. The step3c event class contains all track segments reconstructed in step2: all SDD tracks, with the coordinates and amplitudes of the SDD hits (at most 2 per segment), the TPC tracks, the RICH rings reconstructed with a spatial Hough algorithm as well as RICH rings with non-asymptotic radius for high momentum pion tracks [67]. To avoid time consuming calculations during the data analysis, the inter-detector matches are already established in the step3c production: for each segment the best matching segment (minimizing the pair opening angle) in each other subdetector is determined. For the newly developed track-dependent RICH reconstruction, the RICH hits were also kept. The inheritance tree is shown in Fig. 3.1: the step3c output is stored in objects of type CSSegment, the detector segment base class, contained in the CSEvent. The individual detector segments (CSSegSD, CSSegTPC, CSSegPion, CSSegRICH) inherit from CSSegment. CSSegment itself is a ROOT TObject and implements protocol for object I/O (streaming and storing the data members), organizing and sorting (container classes), error handling, printing etc. All data members are protected (not private)

to allow easy extension of the package by the user employing the concept of inheritance.

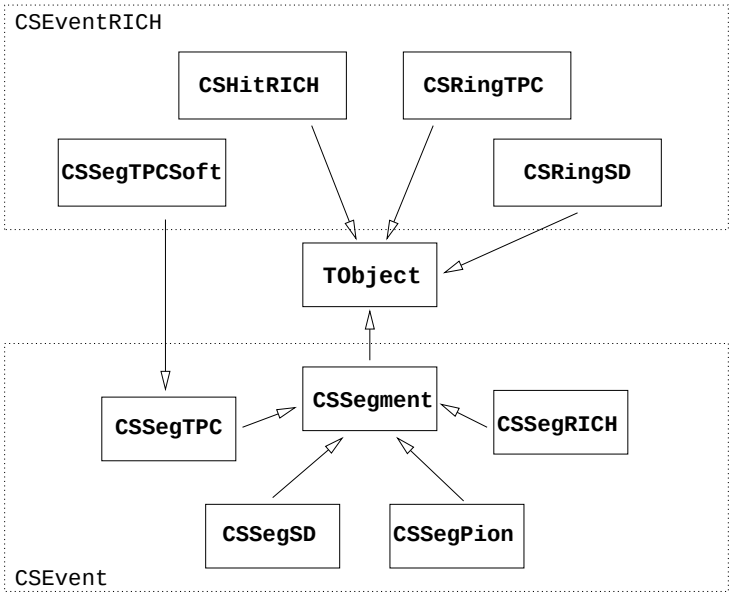

Figure 3.1: Inheritance tree of the step3c (CSEvent) and step4c (CSEventRICH) classes.

3.2.2 Step4c

Step4c stores the results of a raw data partial reproduction performed in the beginning of 2007. This second production had to be carried out for 2 reasons:

1. during the original step2 production, accidentally not all RICH hits were stored on the ROOT tree. When the high-momentum pion reconstruction had been implemented, unfortunately, the COOL library was not consistently updated. As a result, all hits in vicinity of any high-momentum track, about 15% of the total number, were not kept. Applying the newly developed hit-based RICH ring reconstruction in the electron analysis, this loss would have caused strong systematic effects on the electron reconstruction efficiency. The effect is not seen in the traditional reconstruction, since the Hough transformation is carried out at the raw data level and uses the information from (unclustered) RICH pads.

2. a detailed investigation of the contributions to the combinatorial background to the dilepton invariant mass distribution, described in section 5.6, revealed as dominant background source single electrons from π^0 Dalitz decays into two electrons with one non-reconstructed low-momentum leg. To reduce this background, a dedicated low-momentum TPC tracking (section 3.3.2) was developed and run during step4c production.

The process flow of step4c production is presented in Fig. 3.2. The raw data, stored on tapes on CASTOR, is staged to POOL and copied to AFS ("Andrew File System") [68]) volumes for the step0 trigger calibration. The step1 calibration output from the first raw data production can be reused, which allows to directly proceed at the level of step2. In the TPC tracking hits can not be shared by different tracks. To be consistent, the standard track reconstruction is performed first, then the remaining hits are used for the low-momentum tracking. For each raw data file, 1 batch job for step0/step2 is submitted. The output is temporarily stored on ROOT trees containing the conventional step2 event objects, using existing classes from the COOL library. The event contains the newly produced soft and kink tracks as well as the RICH hits. To allow for consistency checks, the trigger information is stored as well.

Once 10 raw data bursts are produced, an automatic procedure submits one further batch job to collect the step2 ROOT files and start step4c production. The newly developed track-based RICH ring reconstruction is applied to the RICH hits, using the fully calibrated TPC segments as well as the SDD segments from step3 as predictors for the ring center. We ensure consistency comparing event by event the trigger information between step3 and the reproduced burst. The 10 step4c output files are TARred, copied to CASTOR and transferred to GSI. The structure of the step4c event class, CSEventRICH, is presented in Fig. 3.1. For data analysis, the step4c library can be loaded together with the step3 library and the data from the supplementary step4c ROOT tree can be analyzed in parallel to the step3 output. Full account of the data members of step3c and step4c is given in Appendix A.

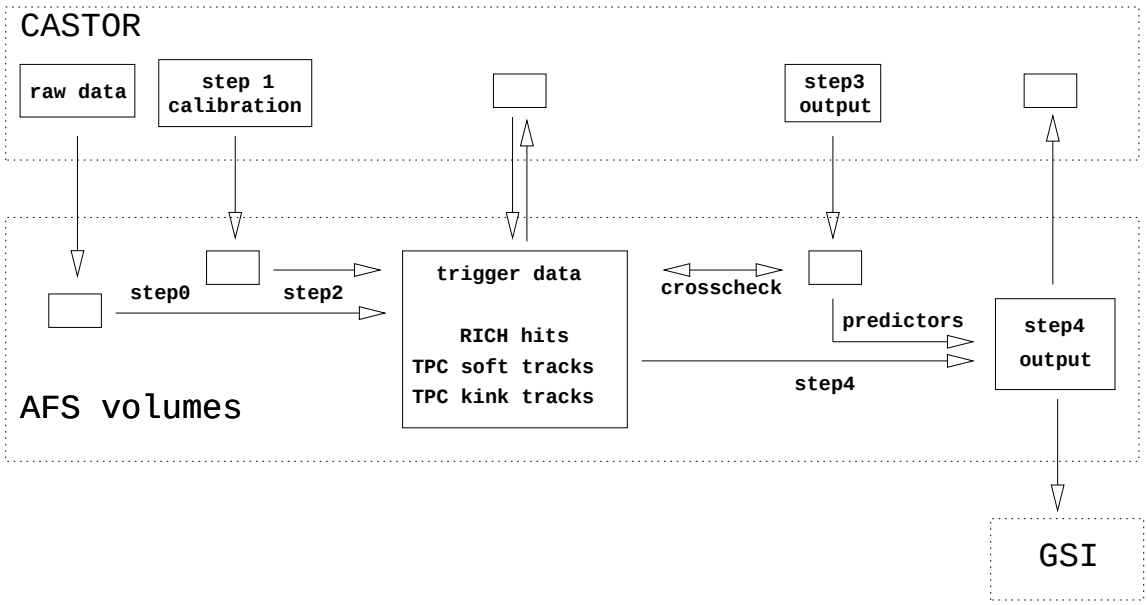

Figure 3.2: Process flow of the step4c production.

3.3 Momentum determination with the TPC

3.3.1 Hit reconstruction and track finding

The hit reconstruction connects, for each of the 20 TPC planes, the amplitude measured in subsequent time bins on adjacent pads, identifies local maxima and calculates the hit position as 2-dimensional center of gravity. The drift time translates into the radial coordinate, the the azimuthal angle ϕ is given by the position on the pad.

The TPC tracking was designed to reconstruct the particle trajectories with high efficiency and accuracy in an environment of high hit multiplicity. The track finding proceeds in several steps. First, 5 hits in the middle planes of the TPC are connected to a track root, defining the curvature of the track in ϕ. Then, the track is extended down- and upstream in order to maximize the number of hits on the track. Hits are searched for within the `hitbin` of the track root, a narrow slice in $\Delta\phi$ and $\Delta\theta$. The expected position for the hit in the next plane is calculated iteratively, extrapolating from the previous hits. To avoid picking up hits too far from the particle trajectory, only hits found within a small window around the predicted position are accepted and added to the track.

3.3.2 Low momentum tracking

With decreasing momentum, charged particles experience stronger deflection in the TPC magnetic field and, on average, stronger multiple scattering (compare Eq. 3.1). To reconstruct soft tracks, the basic steps of the standard tracking were slightly modified,

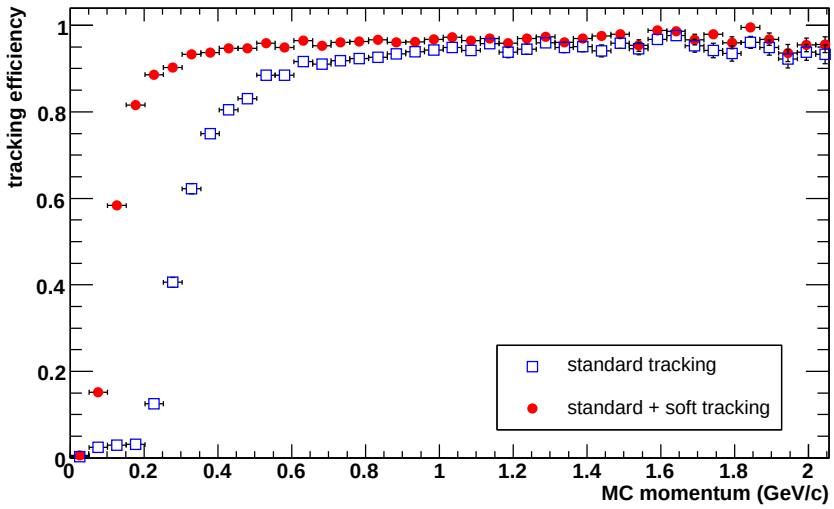

Figure 3.3: TPC tracking efficiency for the standard tracking (open symbols) and the combined standard plus new low-momentum tracking (full symbols). The results are obtained from Overlay Monte-Carlo simulations.

extending the tolerances for hits accepted for track root formation and for hit collection during the track extension. This allows to reconstruct tracks with stronger bend than in the standard method, but also increases the number of fake tracks. To minimize this contribution, the low-momentum tracking is applied as a second step after the standard tracking, excluding hits already used before.

In Fig. 3.3, we show the tracking efficiency for single electrons from a sample of simulated π^0 Dalitz pairs embedded into real events ('Overlay Monte-Carlo'). The standard tracking alone is compared to the results for the combined standard plus low-momentum tracking. The tracking efficiency is of the order of 95% for momenta larger than $\sim$1 GeV/c (during the 2000 runs, due to problems with the electronics, one third of a TPC chamber could not be read out, accounting for part of the small loss of tracks). For lower momenta, the standard track reconstruction exhibits a strong drop in efficiency. In this range, the dedicated soft tracking gives a tremendous improvement: TPC tracks with momenta down to $\sim$0.4 GeV/c are still reconstructed. We note that there is also a small contribution of high-momentum tracks found by the new tracking which were not reconstructed before.

3.3.3 Track fitting

The hits on TPC tracks established in step2 are (re-)fitted during the step3c production (for a detailed description of the fit procedure see [48, 69]. The fit proceeds in two steps: 1.) a straight line radial fit of the cylindrical coordinate $\rho(z)$, where z is parallel to the beam axis, to determine the polar angle θ of the track. 2.) a fit of the momentum-dependent deflection $\phi(z)$ induced by the magnetic field in the TPC. Due to the intricate inhomogeneous B-field configuration, the deflection of the particle in the magnetic field can not be described analytically with sufficient accuracy. Instead, the field is calculated in a finite-element framework and reference tracks for simulated particles are stored in bins of θ, ϕ and momentum. The fit is carried out iteratively, varying the momentum smoothly from the initial value for the track reference, to determine the set of parameters which minimize χ^2 of the reconstructed hits with respect to the reference track. The point resolution of the hits is estimated as function of the drift time and pad amplitude. To take further systematic effects of the detector resolution on the hit reconstruction into account, the hits are additionally weighted with their inverse residuals from fits to a representative set of simulated tracks, stored as function of the hit position [70].

In Fig 3.4, we present the momentum resolution obtained from Overlay-Monte-Carlo simulations. Two approaches to describe the azimuthal deflection of the track are compared: in the 2-parameter fit, solely the reference track is used to determine the phi offset at the target center, z=0, and the inverse particle momentum. In the 3-parameter fit, an further parameter is introduced to superimpose an additional azimuthal deflection, linear in z, as is introduced e.g. by multiple scattering of the particle. Scattering dominates

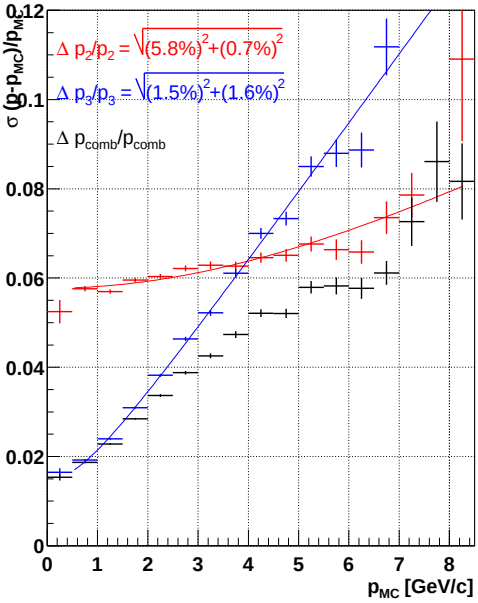

Figure 3.4: Momentum resolution for the 2-parameter (labelled p2) and 3-parameter (p3) track fitting procedures and the combined (p_{comb}) reconstruction.

for low particle momenta. Consequently for softer tracks the 3-parameter fit gives the better description of the particle trajectory, resulting in superior momentum reconstruction. For high momenta, the scattering hypothesis is less justified and the 2-parameter fit gives the better results. The combined momentum resolution, as indicated in the figure, is $\Delta p/p \sim 2\% \oplus 1\% \cdot p/(\mathrm{GeV/c})$.

3.4 Particle identification with the TPC

In the TPC, different particle species can be distinguished by their energy deposit in the detector gas. Moderately relativistic charged particles loose energy in matter primarily by ionization and atomic excitation. The mean rate of energy loss is given by the Bethe-Bloch equation [6],

$$-\frac{dE}{dx} = Kz^2\frac{Z}{A}\frac{1}{\beta^2}[\frac{1}{2}\ln\frac{2m_ec^2\beta^2\gamma^2T_{max}}{I^2} - \beta^2 - \frac{\delta}{2}]$$

Here T_{max} is the maximum kinetic energy which can be imparted to a free electron in a single collision, Z and A the atomic number and atomic mass number of the absorber, β, γ and z the velocity, Lorentz factor, and charge of the incident particle, and K a constant factor. I is the mean excitation energy. For very low momenta the energy loss is high, decreases with increasing momentum until it reaches a minimum at $\beta\gamma \simeq 4$. As the particle momentum increases further, the ionization rises as $\log(\beta\gamma)$ (logarithmic rise) until it saturates at very high energies at the Fermi plateau, the height of which (relative to the minimum) is determined by the parameter δ.

In the TPC, the energy deposit of the incident particle is measured by the amplitude of the hits on track. The energy loss probability in individual collisions follows a Landau distribution, which is strongly asymmetric ('Landau tail'). Consequently, the most probable energy loss is lower than the mean. A more robust measure of the energy deposit than the mean is the `truncated mean`, for which the hits with the highest and the lowest amplitude are not included. Fig. 3.5 shows the truncated dE/dx as function of momentum for both negative and positive particles. The lines in the figure [57] are calculated for different particle species according to Eq. 3.4. Pions, electrons, protons and kaons can be clearly distinguished. The dE/dx resolution [55], shown in the lower panel of Fig. 3.5 on the right, depends on the number of hits on track.

For tracks with many hits, the measured resolution approaches the parametrization following Allison and Cobb [71] also shown in the Figure. For the maximum possible

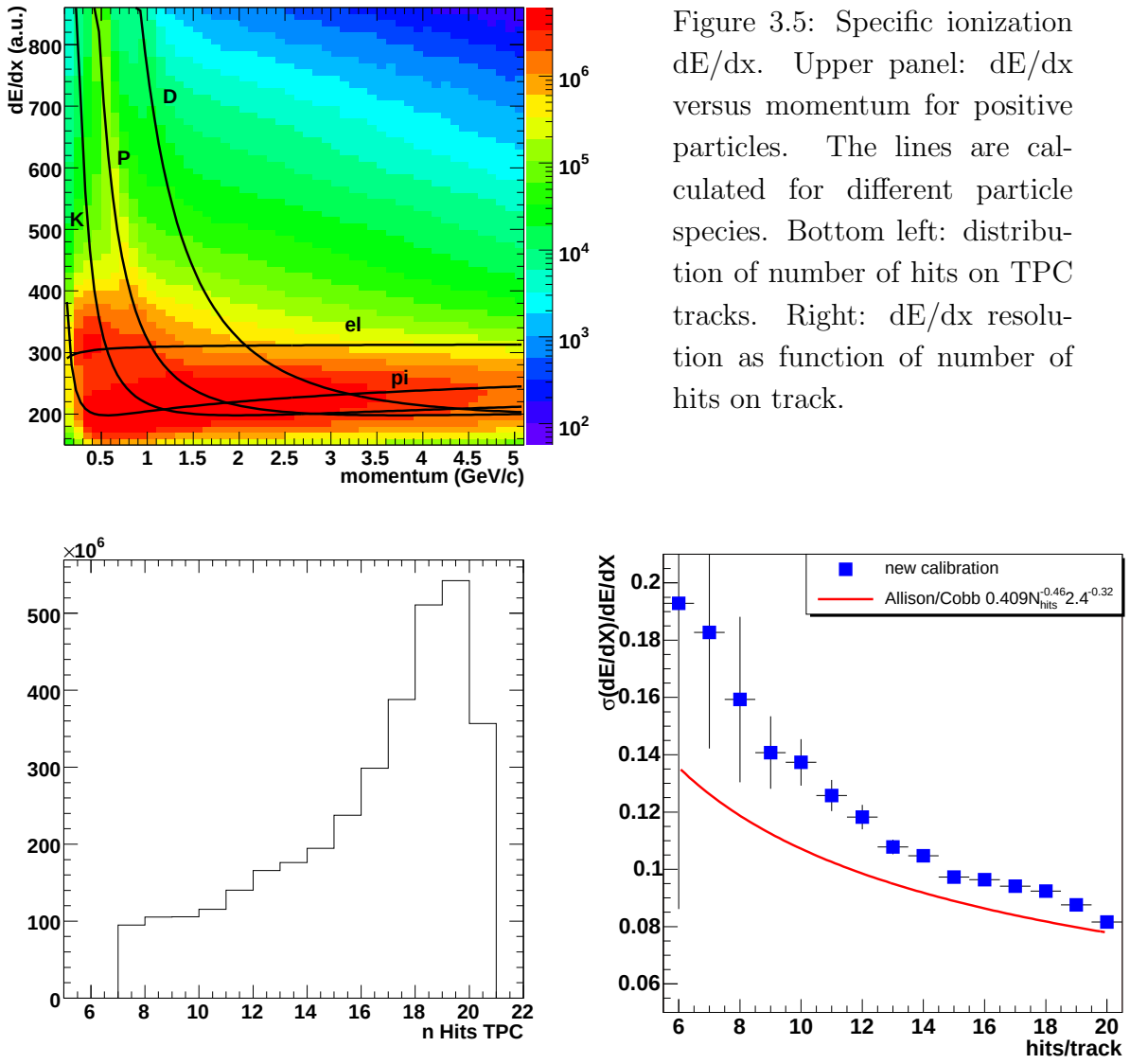

Figure 3.5: Specific ionization dE/dx. Upper panel: dE/dx versus momentum for positive particles. The lines are calculated for different particle species. Bottom left: distribution of number of hits on TPC tracks. Right: dE/dx resolution as function of number of hits on track.

value of 20 hits on track, the resolution is 8%. Since the most probable number of hits on track is 19, as demonstrated in the left panel, the majority of tracks is measured with a dE/dx resolution better than 10%.

3.5 SDD tracking

The SDD raw data consists of the amplitudes of 360 anodes and 256 time bins sampled by the FADC. After pedestal subtraction, pulses of adjacent time bins with nonzero amplitude are identified. The center of gravity in time direction is calculated, applying a correction for the so-called `ballistic deficit`, signal loss during on the level of the electronics induced by the the systematic delay of the signal arrival time as function of the radial hit coordinate due to diffusion of the charge cloud. Pulses on neighboring anodes whose center of gravity differ by less than one time bin are joined into a hit. The hit coordinate in azimuthal direction is calculated as the center of gravity of the contributing pulses.

The reconstructed hits are combined to tracks and are used to reconstruct the vertex in an iterative robust vertex fitting procedure [72]: all hits in SDD1 and SDD2 are combined to straight track segments and a weighted sum of their projected distances to the assumed vertex position is calculated. In the next iteration, this center of gravity becomes the new initial value for the vertex position and each track segment gets a new weight according to its deviation from the mean value in the previous step. After the position of the

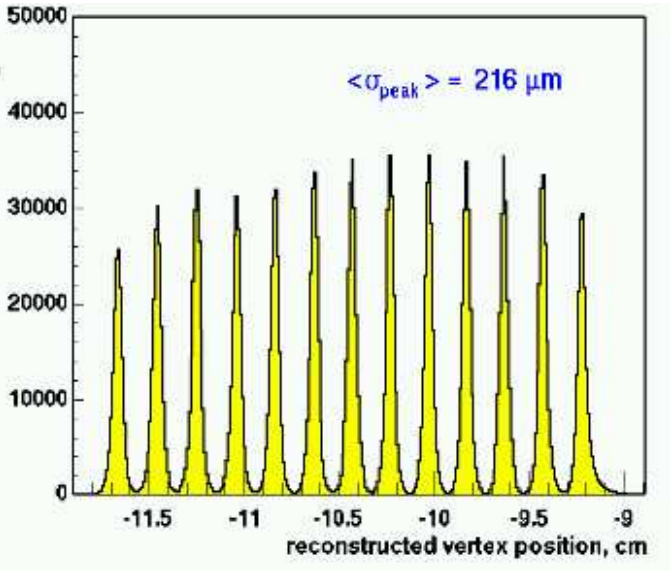

Figure 3.6: Distribution of vertex positions reconstructed with the SDD detectors along the beam axis showing the 13 Au target disks.

vertex is defined, its z-position is redefined as the position of the closest vertex disc. The vertex reconstruction capabilities of the SDD detectors are demonstrated in Fig. 3.6, which presents the reconstructed vertex positions before shifting: the 13 subtargets are clearly resolved. The obtained vertex resolution is $\sigma_z \simeq 200$ μm.

3.6 Charged particle multiplicity

The average number of charged particles produced per event as function of the pseudo-rapidity η is determined with the SDD detector, using the SDD hits (but not the tracks) established during the step2 tracking. Details of the analysis can be found in [73, 74].

Tracks are constructed combining the hits from SDD1 and SDD2 to all possible pairs. The contribution of fake combinations is evaluated counting the number of uncorrelated pairs obtained after rotating one of the SDD detectors. To avoid losses due to dead anodes, the analysis is carried out in a restricted phi slice and the result extrapolated to full 2π coverage. To avoid any bias introduced by artificial hit splitting or limited two-track resolution, only hits are used that are isolated within a certain minimum distance to their next neighbor. This cut is systematically varied, and the exponential dependence between track multiplicity and the size of the isolation window extrapolated to zero. The contribution from δ-electrons was estimated from data taken with a beam trigger and subtracted. Fig. 3.7 shows the charged particle density $dN/d\eta$ for events with 0-5% and 5-10% centrality. Averaging over the interval $2.1 < \eta < 2.65$, relevant for the electron analysis, the charged particle density is 347 for 0-5% and 292 for 5-10% centrality. The relative systematic error on the measurement is estimated to 12%.

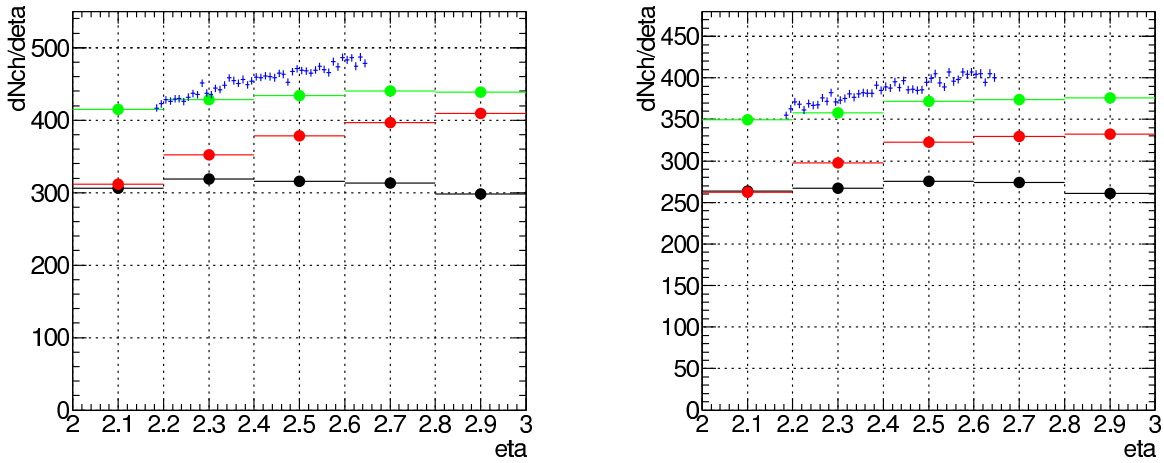

Figure 3.7: Pseudorapidity distributions of charged particles: raw(black) and corrected for two-track efficiency. The result of a naive counting SDD tracks, without subtraction of fakes, is shown in green. For comparison, the charged tracks in the TPC are shown in blue.

3.7 Particle identification with the RICH detectors

3.7.1 Hit reconstruction and clean-up

The raw data of the two RICH detectors consists of the induced-signal amplitudes of ∼50000 pads in each detector. The hit reconstruction proceeds in two steps. During raw-data production adjacent pads with an amplitude above a threshold are joined to clusters. A first `clean-up` procedure, based on pad amplitudes and cluster topology [54], is applied to reject fake clusters not originating from a photon produced in the radiator. Finally, the hit coordinates are determined from the position of the local maximum of the amplitudes of the pads within a cluster. Clusters with more than 2 local maxima are split.

Further rejection of noisy hits is applied during step4c production. This second clean-up step on the hit level is illustrated in Fig. 3.8. The 2-dimensional histogram in the upper left panel shows the distribution of RICH1 hits in the projective plane (of unit radius), normalized to the number of events. For the hit clean-up, the detector area is

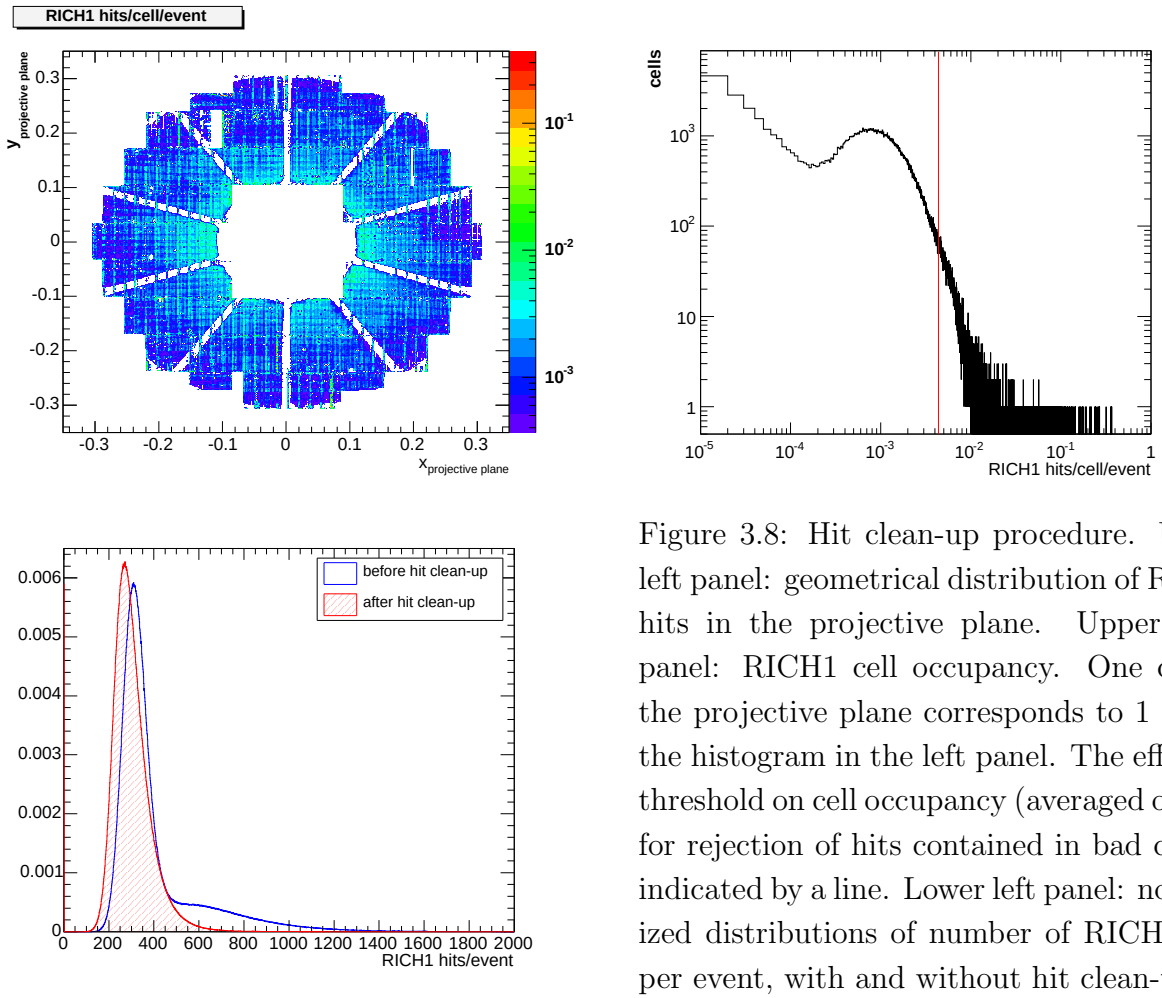

Figure 3.8: Hit clean-up procedure. Upper left panel: geometrical distribution of RICH1 hits in the projective plane. Upper right panel: RICH1 cell occupancy. One cell in the projective plane corresponds to 1 bin in the histogram in the left panel. The effective threshold on cell occupancy (averaged over θ) for rejection of hits contained in bad cells is indicated by a line. Lower left panel: normalized distributions of number of RICH1 hits per event, with and without hit clean-up.

divided into quadratic cells corresponding roughly to the size of a pad. One bin in the histogram represents one cell. The distribution of bin contents, i.e. the occupancy of the detector cells, is shown in the upper right panel. The peak at very low values of RICH hits/cell/event corresponds to inactive regions in the radiator (e.g. the mirror spokes). Only strongly scattered photons arriving from the mirror produce a hit here. Towards high cell occupancies the distribution displays a pronounced tail, representing cells which contain a hit about 30, 40 times more often than expected on average. Such unreasonably high occupancy is a strong indication for a detector effect producing fake hits. Hence, cells containing more than a maximum allowed number of hits are marked as 'bad' and discarded during the RICH ring reconstruction. The threshold for RICH1 (RICH2) is adjusted differentially within slices of polar angle θ to retain 95% (99%) of all cells within a given slice. The θ-averaged effective threshold in terms of cell occupancy is indicated in the figure. In the same spirit, cells containing a hit in 2 or more subsequent events are marked as 'bad'. A small contribution of fake hits due to artificial hit splitting during the hit finding procedure is reduced joining any two hits closer than a minimum required distance. The thresholds applied in the hit clean-up procedure were carefully adjusted, monitoring electron efficiency and pion rejection of the RICH ring reconstruction, in order to minimize the number of fake hits while maintaining the highest possible photon reconstruction efficiency.

In the lower panel of Fig. 3.8, the normalized distributions of the number of RICH1 hits per event with and without the hit clean-up are presented. The peak of the distribution is only slightly shifted. However, the pronounced tail caused mostly by fake hits is strongly reduced by the clean-up procedure.

3.7.2 Free ring reconstruction: Hough transformation

The RICH ring reconstruction hitherto [29, 32, 33] used for electron identification is a spatial Hough transformation. The algorithm finds rings with known (asymptotic) radius. The procedure is a RICH standalone reconstruction, i.e. the ring centers are determined using no other than RICH information. In the CERES production chain, the Hough transformation is carried out on the raw data level during step2 production, using the detector pads (and not the RICH hits). The method relies on a simple geometrical procedure: given a circle with radius R, the center of the circle can be constructed as the intersection of any three (or more) circles with radius R centered themselves on the circumference. The algorithm for RICH ring reconstruction maps the detector pads to a Hough array. For each pad with a signal, all cells in the array located on a ring with asymptotic radius centered at the pad are incremented by the pad amplitude. The local maxima of the Hough array define the ring centers.

3.7.3 Track based ring reconstruction I: free radius

In the track based ring reconstruction, the ring center is determined as intersection of the extrapolated TPC track with the RICH1-RICH2 combined plane. Each TPC track is considered a predictor. Knowledge of the ring center reduces ring reconstruction to one dimension (`angular Hough transformation`): the histogram in Fig. 3.9 is an example for the distribution of the distance of RICH hits from the predicted ring center for a `single` electron track (hence the strongly visible Poissonian bin-by-bin variations). All hits on a ring have the same distance - given by the ring radius - from the center. The ring radius can be considered a free parameter and determined as the global maximum of the distribution (for the electron track shown, the asymptotic radius of 31 mrad is expected). Therefore, this reconstruction method is not limited to rings with asymptotic radius and not restricted to electron identification. It can also identify other radiating particles, e.g. pions or muons, with momenta above the Cherenkov threshold.

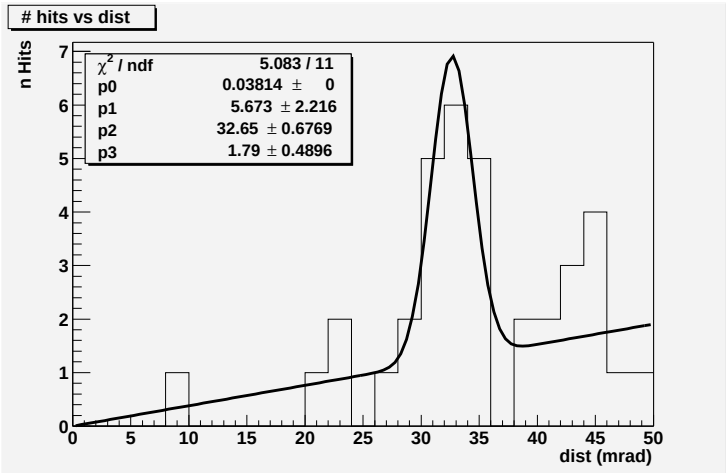

Figure 3.9: Distance of RICH hits from predicted ring center for one electron track. The fit to the distribution determines the ring radius (maximum) and background (see text for details). The expected asymptotic radius is 31 mrad.

The second measure to qualify the ring properties is the number of hits on ring. It corresponds to the integral over the maximum of the histogram (we adopt an integration interval of 6 mrad, corresponding to 3 histogram bins). The bin-by-bin fluctuations of the histogram entries indicate a non-negligible density of background hits in the RICH[2]. The contribution of background hits to the maximum is estimated from the local average hit density in vicinity of the predictor, as illustrated in the figure: the maximum of the histogram is fitted by a Gaussian peak on top of linearly increasing background. The linear behavior of the background reflects a locally homogeneous and isotropic background hit

[2]To the background several sources contribute, among them fake hits, but also real photons hits produced by secondary interactions, δ electrons and pions and muons just above the Cherenkov threshold.

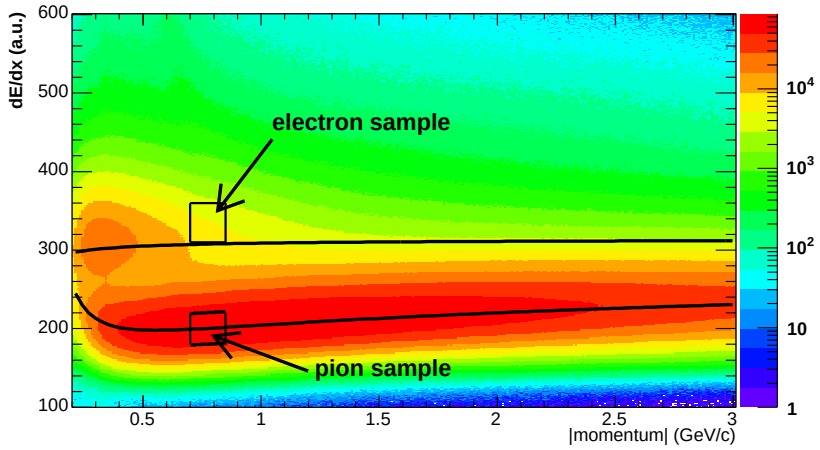

Figure 3.10: Sample selection via TPC particle identification. The lines indicate the dE/dx vs momentum cuts applied to prepare an electron enriched sample and a pion dominated sample of particles below the Cherenkov threshold.

density. The mean of the Gaussian accurately determines the ring radius, the area under the line the number of background hits in the integration interval.

Technically, the log-likelihood fit procedure implements a Levenberg-Marquardt algorithm [75, 76, 77], as described in Appendix B. Since the fit is applied in every event to each TPC predictor, performance is a critical issue for this application: the routine was carefully optimized and is 1-2 orders of magnitude faster than conventional multi-purpose routines for non-linear optimization.

For a proof of principle, we present results of the RICH ring reconstruction for an electron-enriched sample of predictors. Electrons are selected exploiting TPC particle identification, selecting tracks within the RICH1 and RICH2 fiducial acceptance ($0.180 < \theta < 0.235$) with electron-typical dE/dx within a small momentum range, as indicated in Fig. 3.10. We require very high track quality to ensure good dE/dx resolution. To exclude conversion pairs, a very good match ($1\ \sigma$) between the TPC and SDD track is required, and the conversion rejection cuts, described in section 3.8.4, namely a cut on the resummed SDD dE/dx and a TPC isolation cut, are applied. The electron reference is confronted to a background sample of pions with momenta below the Cherenkov threshold, for which no RICH ring is expected. We prepare the pion sample applying the same criteria, except for the different dE/dx selection, shown in Fig. 3.10. The distribution of the reconstructed ring radius for both samples is presented in Fig. 3.11. For the electrons, we observe a pronounced peak at the expected asymptotic radius corresponding to the Cherenkov angle of 0.031 rad. The unavoidable contamination of hadrons present in the electron enriched sample gives rise to a second component, smeared over all radii, which is reproduced by the background reference in the right panel. The radius distribution for the non-radiating hadrons is featureless and rises monotonically, representing the probability of an upward

fluctuation of the number of background hits from the average, which increases with the distance from the predictor.

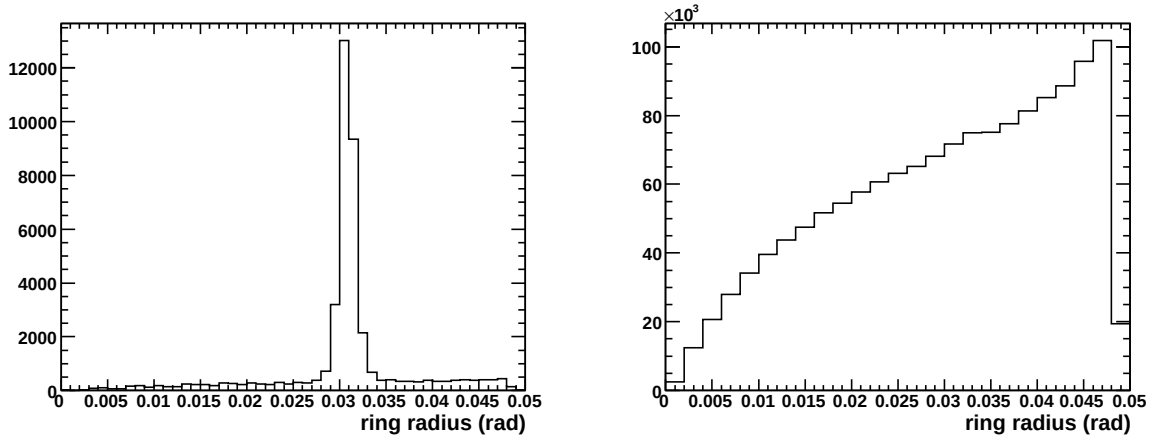

Figure 3.11: Reconstructed RICH ring radius distribution. Left panel: electron enriched sample. Right panel: background sample of non-radiating particles.

3.7.4 Track based ring reconstruction II: asymptotic radius

The track based ring reconstruction gives the freedom to reconstruct rings with any radius. However, electrons in the relevant momentum range exceeding a few 100 MeV/c have asymptotic radius. For electron identification, we can exploit this knowledge in the ring reconstruction. Technically, we proceed as described before, counting the number of hits with distance r_∞=0.031 rad from the predictor. The distribution of the number of hits on ring is shown in Fig. 3.12. For the non-radiating hadron reference, after subtraction of the contribution of background hits, the most probable value of the distribution is zero. In the distribution for the electron enhanced sample, this peak recurs due to the hadron contamination, but in addition we observe a pronounced contribution from Cherenkov photons. The interpretation of the inefficient peak in the electron distribution as a consequence of pion contamination is substantiated by quantitative estimates of the purity of the sample selection with the adopted TPC dE/dx cuts. Furthermore, the contribution of imperfections of the RICH detector system (dead areas) to the inefficient peak was investigated within the CERES Monte-Carlo detector simulation. It was found to be very small (as discussed more quantitatively in section 3.7.5). This conclusion also receives strong support by the correlation of the number of hits on ring measured in RICH2 versus RICH1 for the electron enriched sample, shown in the bottom right panel of Fig. 3.12: the plot nicely illustrates how for the pions both in RICH1 and RICH2 no hits are found on the expected ring, in contrast to the electron component, to which both RICH1 and 2 contribute.

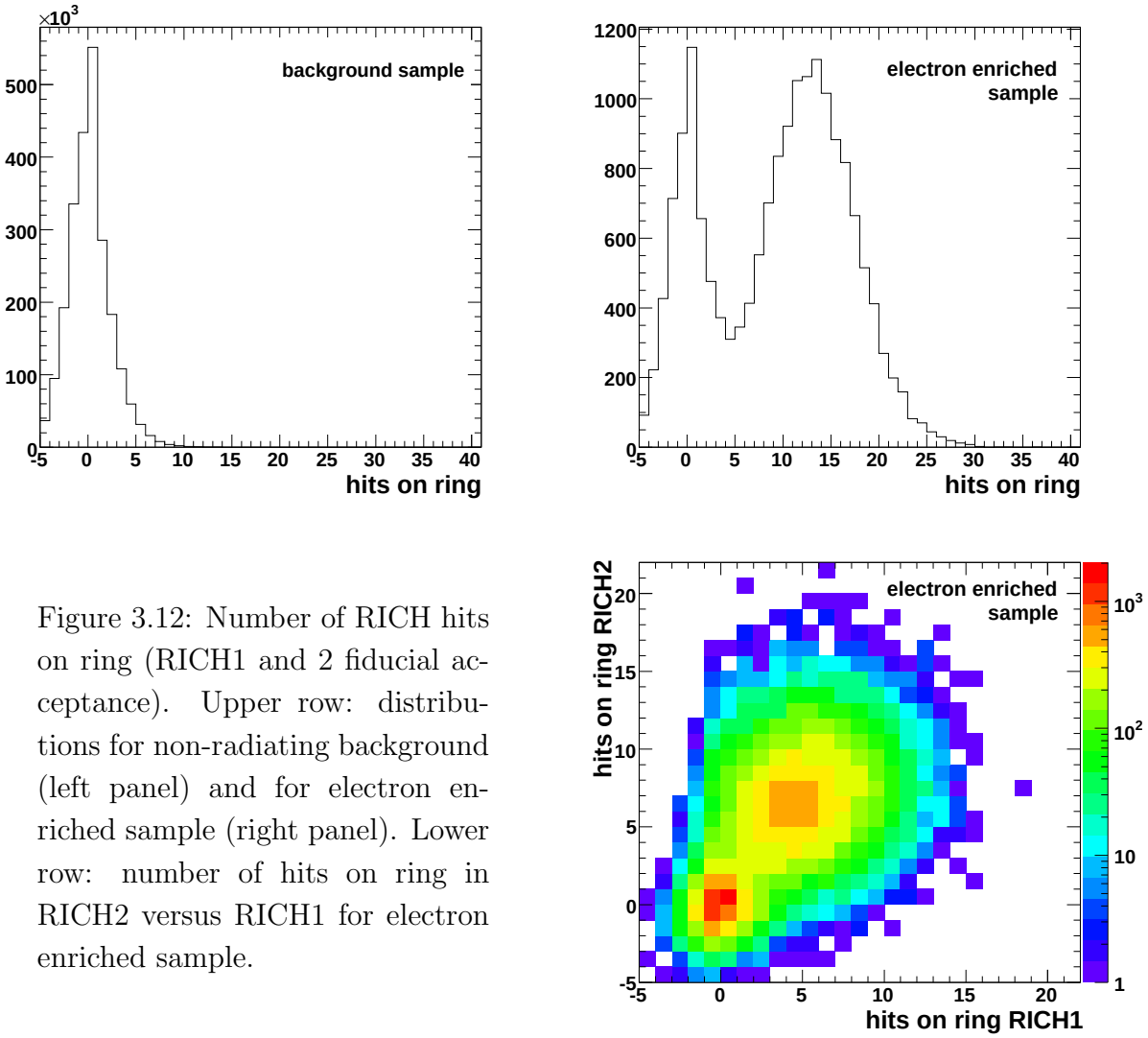

Figure 3.12: Number of RICH hits on ring (RICH1 and 2 fiducial acceptance). Upper row: distributions for non-radiating background (left panel) and for electron enriched sample (right panel). Lower row: number of hits on ring in RICH2 versus RICH1 for electron enriched sample.

3.7.5 RICH electron efficiency and pion rejection

In this section we present the experimentally determined RICH efficiency. The electron efficiency is closely tied to the pion rejection: requiring certain characteristics for a 'true' electron ring, a fraction, called efficiency, of all electrons is correctly identified. On the other hand, some hadrons, mostly pions, are misidentified as electrons. The latter probability is represented by the pion efficiency, the fraction of pions misidentified as electrons, or related quantities, like the pion rejection (1 - pion efficiency) or the inverse pion efficiency, commonly referred to as 'pion rejection factor'. Electron and pion efficiency are correlated: varying the ring selection criteria (i.e. the cuts on ring characteristics), a cut with higher electron efficiency unavoidably results in a higher pion efficiency. We investigate this systematics in order to 1.) characterize the particle identification properties of the CERES RICH detector system and 2.) to allow for a comparison of the performance

of various ring reconstruction algorithms with possibly very different measures of the ring characteristics. Technically, the pion and electron efficiencies are determined from the distributions obtained for the reference electron and background samples described in the previous sections, having subtracted the hadron contribution from the electron enriched sample.

In Fig. 3.13, the electron efficiency for the RICH1 and RICH2 common fiducial acceptance is plotted against pion rejection. We compare the track-based RICH ring reconstruction algorithms described in Section 3.7.3 (labelled 'free radius') and Section 3.7.4 (labelled 'asymptotic radius') to the spatial Hough algorithm (Section 3.7.2). Along the graph for the reconstruction with asymptotic input radius, we vary the cut on the number of hits between 6 and 13. For a pion rejection of 99%, we measure an electron efficiency of 90%; for a cut of 10 hits, the pion rejection grows to 99.9%, still accepting more than 70% of the electrons. In case of the free radius ring search, in addition to a varying cut on hits on ring we also restrict the reconstructed radius to $r_\infty \pm$ 0.003 (compare Fig. 3.11). The figure demonstrates the benefit (for the purpose of electron ID) of using the expected electron ring radius as an input to the reconstruction: for a given pion rejection, the electron efficiency is slightly higher for the asymptotic ring reconstruction compared to the

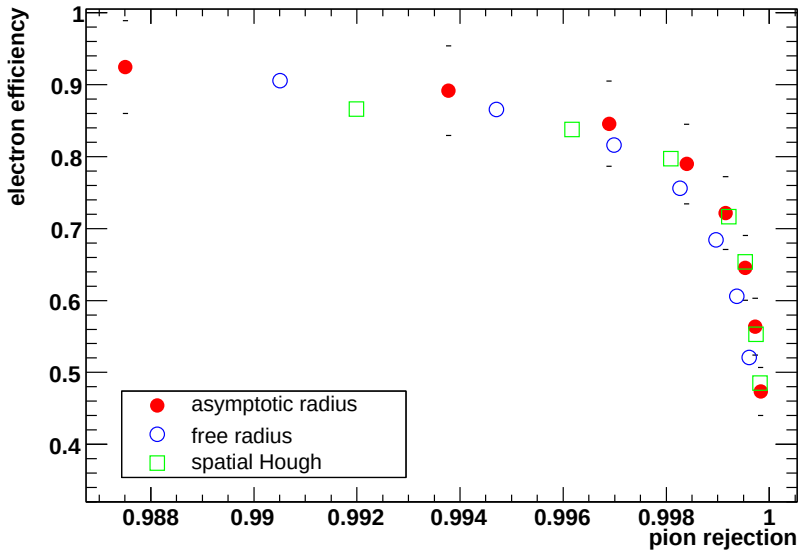

Figure 3.13: RICH electron efficiency versus pion rejection for different reconstruction methods (RICH1 and 2 fiducial acceptance). Two track-based ring reconstruction methods with free radius and asymptotic input radius are compared to the spatial Hough algorithm. Along each line we vary the cut on required ring quality. The systematic error on the evaluated efficiency, common to all three curves, is indicated for the asymptotic radius reconstruction.

free radius ring search. For the comparison with the spatial Hough algorithm, we apply a 1.5σ TPC-RICH matching cut as in [55, 54] and require in addition a Hough amplitude varying between 90 (intrinsic threshold of the algorithm) and 230. The spatial Hough reconstruction, which also employs the asymptotic input radius, performs very similar to the track-based ring search algorithms.

The relative systematic error of the electron efficiency is estimated to 7%. It is composed of two contributions. The error induced by the subtraction of the inefficient peak from the distribution of number of hits is 4%, estimated by the variations observed for the different algorithms. A further contribution stems from the systematic uncertainty on the `shape` of the background subtracted distribution of the number of hits on ring in the vicinity of 0. This tail receives a contribution from geometrical inefficiencies of the RICH detector (dead areas). We reproduce these inefficiencies within the Overlay Monte-Carlo simulation of the detector and correct, in the data, the scale applied for subtraction of the inefficient

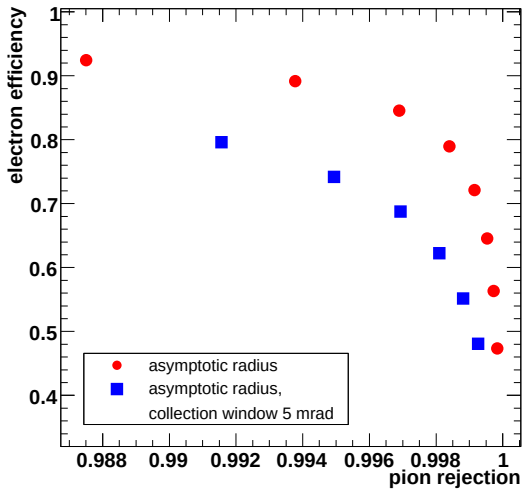

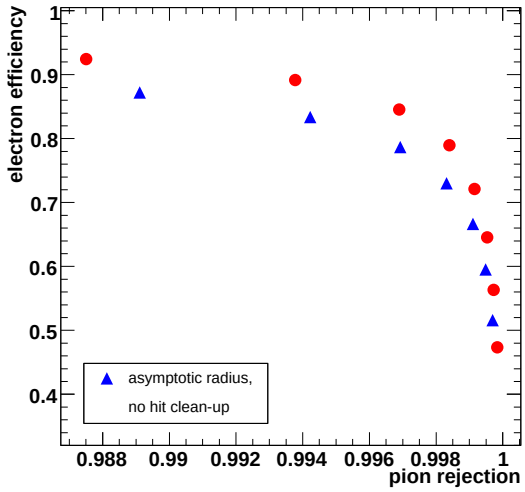

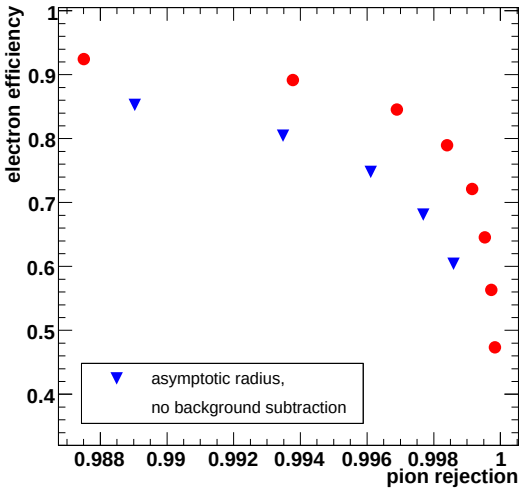

Figure 3.14: Optimization of the RICH electron efficiency and pion rejection. Different approaches are compared to the standard track-based reconstruction with asymptotic input radius. Upper panel: variation of the hit collection window. Lower panels: effect of the eventwise hit clean-up procedure (left panel) and the track-wise background subtraction (right panel).

peak until the shape of the tail from the simulations is reproduced. The correction on the obtained efficiency is 3%, which is interpreted as maximum contribution to the error. For convenience, in Fig. 3.13, the systematic error, common to all three graphs, is only indicated once.

Fig. 3.14 illustrates the optimization of the performance of the RICH reconstruction algorithms. In the top panel we compare the track-based asymptotic radius ring reconstruction in the 'standard' version, with a hit collection interval $r_\infty \pm$ 0.003 rad, to a modified incarnation with increased tolerances $r_\infty \pm$ 0.005 rad. The larger collection interval results in higher hit collection efficiency, but on the other hand the contribution from pick-up of background hits is expected to rise. This latter effect dominates, as demonstrated by the figure. For given rejection, the efficiency is much higher for our standard choice of the collection interval. In the lower panels, we demonstrate the effect of the hit clean-up procedure applied prior to ring reconstruction (Section 3.7.1), and of the local track-by-track background hits subtraction (Section 3.7.3). The effect of either way of background suppression is an improvement of the pion rejection for a given cut (shifting, in a way of speaking, the whole curve to the right). This also translates to higher efficiency for given rejection.

3.7.6 Geometrical effects

The RICH performance discussed in the previous section was geometrically restricted to the fiducial acceptance, the area of full ring containment in both RICH1 and RICH2. However, in the range of interest for the electron analysis, $2.1 < \eta < 2.65$, corresponding to the polar angle interval $0.244 > \theta > 0.141$, the coverage by RICH2 is incomplete. Consequently, approaching lower θ, we expect a decrease of the number of hits on ring: the RICH2 acceptance is roughly $0.140 < \theta < 0.270$, resulting in losses of hits from $\theta \approx 0.170$ down. In the left panel of Fig. 3.15 we present the scatter plot of the number of hits on ring versus θ of the predictor, for an electron enriched sample. One can, again, distinguish the electron contribution at a high value of hits on ring and the contribution from non-radiating particles. We have superimposed the graph of the most probable number of hits on ring, determined differentially in θ slices of 10 mrad width (red circles). It clearly indicates how, approaching smaller θ, the number of hits on ring goes down. The resulting loss of efficiency is shown in the right panel of Fig. 3.15, for a cut requiring at least 10 hits on ring. Note that here the subtraction of the contribution of non-radiating particles is done independently in each θ slice, and consequently this contribution to the systematic error in each slice is uncorrelated.

The effect manifest in the signal is also expected for the background hits: outside the RICH fiducial acceptance, the assumption of an isotropic hit distribution (and a linear increase of the number of hits picked up as function of the distance from the ring center)

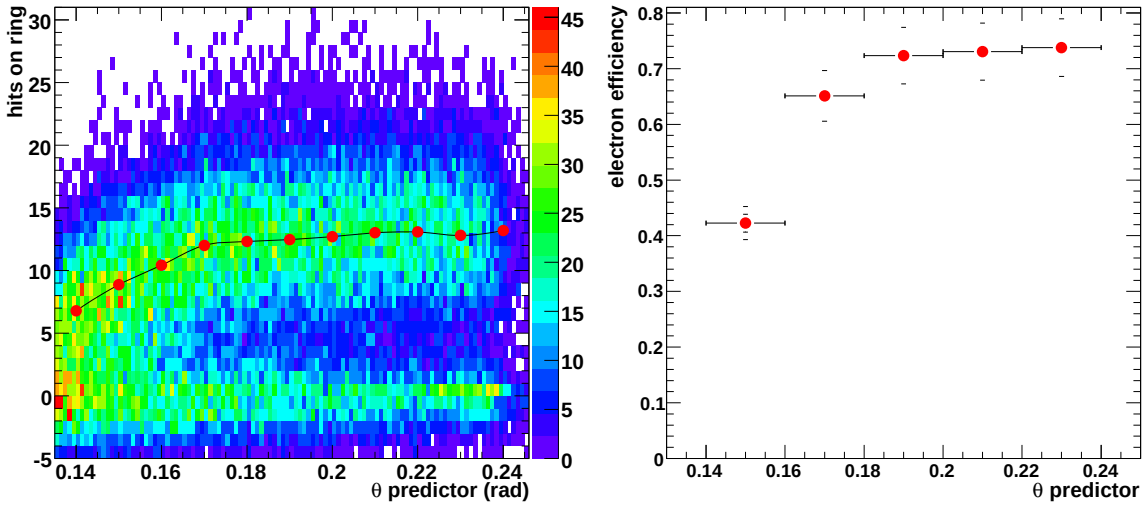

Figure 3.15: Effect of the RICH acceptance. Left panel: number of hits on ring (asymptotic radius), plotted as function of the θ coordinate of the ring center for an electron enriched sample of tracks. The m.p.v. of the number of hits for slices in θ is superimposed on the scatter plot (line to guide the eye). Right panel: RICH efficiency versus theta. A constant cut of 10 hits is applied.

breaks down. The expected modification of background density is taken into account by a nonlinear correction to the shape of the background fit, described in Appendix B.

3.7.7 Momentum dependence

The RICH efficiency depends on the momentum of the radiating particle. For different reasons, efficiency losses are expected at low momenta:

1. For momenta of the order of the threshold momentum, the number of emitted Cherenkov photons depends on the Cherenkov angle $\sim \sin^2\theta_c$ (Eq. 2.2).

2. Multiple scattering of the emitting particle results in a "smearing" of the emitted photons with respect to the "nominal" ring center. The photon hit collection efficiency deteriorates [3]

[3]The emission of Cherenkov radiation is an interference effect. The formation length $l_F = 2\gamma^2 c/\omega$ [78] for emission of a photon of energy ω by a particle with Lorentz factor γ is estimated to a few times 10 cm for an electron of $\lesssim$1 GeV/c and a photon in the UV range (few eV). This is comparable to the length $l_\gamma = \alpha X_0/(4\pi)$ over which a particle statistically scatters an angle $1/\gamma$ due to multiple Coulomb scattering. Hence, a further direct suppression due to the distortion of the emission process by multiple scattering is conceivable.

3. For the track-based ring reconstruction, a correlation between the ring center resolution and the photon hit collection efficiency is expected. Consequently, multiple scattering also induces efficiency losses at this level.

In the momentum range accessible to CERES, effect (1.) is only relevant for pions and muons, whereas (2.) and (3.) should be expected for electrons with asymptotic radius, too. In Fig. 3.16, we present the measured momentum dependence of the electron efficiency. A cut of 10 RICH hits is applied. For momenta larger than ∼1 GeV/c, the efficiency is constant, for smaller momenta we observe a deterioration. The onset of this efficiency drop corresponds roughly to a transverse momentum of p_T=200 MeV, the transverse momentum threshold for the electron pair analysis. Note that in this plot the subtraction of the contribution of non-radiating particles is done independently in each momentum slice. Consequently, the corresponding contribution to the systematic error in each slice is uncorrelated.

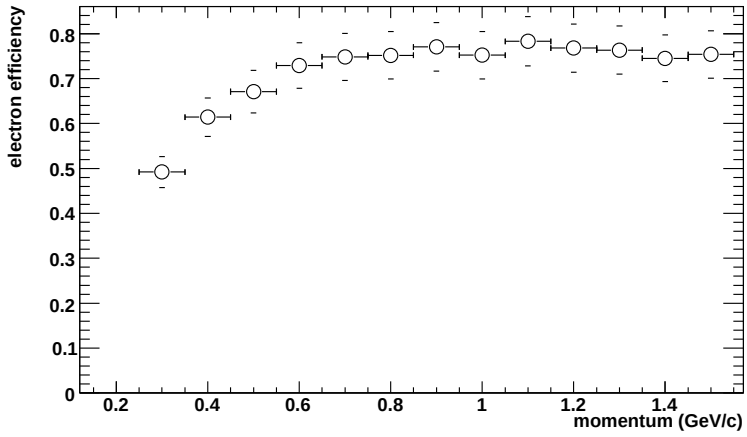

Figure 3.16: RICH efficiency versus momentum. A cut of 10 hits is applied. The systematic errors are in each slice receive a contribution from the subtraction of the non-radiating particles, which is uncorrelated between different slices.

3.7.8 High momentum pion case

The track-based ring reconstruction with free radius allows identification of Cherenkov radiating particles other than electrons. Since the present work focusses on electron pair reconstruction, we will not discuss the subject in depth, but rather flash some basic results to give a proof of principle.

In the momentum range accessible to CERES, the only hadrons emitting Cherenkov radiation are pions, with a momentum threshold of 4.7 GeV/c. In the spirit of the approach employed in the previous sections, we investigate the RICH response for a test

sample of radiating pions, applying a momentum dependent cut on the TPC dE/dx, as shown in Fig. 3.5. In Fig. 3.17, we present the reconstructed radius as function of the pion momentum. For low momenta (non-radiating pions) we observe the background-induced distribution of fake radii already known from Fig. 3.11 (no cut on the number of hits on ring is applied in this plot). In contrast, above 5 GeV/c, the Cherenkov radius is clearly reconstructed. The momentum dependence of the reconstructed radius compares well to the theoretical expectation (Eq. 2.4), indicated by the line superimposed to the plot. The largest deviations are observed at low momenta, where the rings are, due to the momentum dependence of the photon yield, least defined.

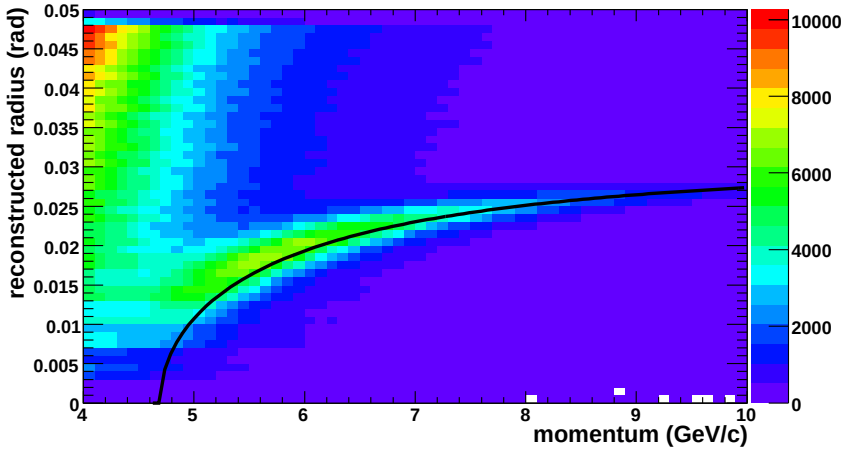

Figure 3.17: RICH reconstructed radius versus momentum for a pion sample. For radiating pions, at momenta larger than 4.7 GeV/c, the Cherenkov radius is clearly reconstructed. The curve superimposed on the figure shows the theoretically expected momentum dependence.

3.8 Dilepton analysis

The major steps of the electron analysis are:

- global track reconstruction,
- electron identification,
- background rejection,
- pairing and subtraction of combinatorial background.

In the first and second step, individual detector segments are combined to electron tracks. The majority of these electrons stems from trivial physics sources. Hence, in the third step we attempt to identify and remove them the electron track sample. Finally, the electrons are combined to dilepton pairs and the combinatorial background is subtracted to obtain the physics signal.

3.8.1 Global track reconstruction

A global track consists of a TPC and SDD track segment. We construct global tracks combining each TPC segment with the SDD segment which minimizes the opening angle between the segments. The matching distribution of the opening angles (discussed here in terms of the projections on θ, ϕ) is a measure of the detector position resolution. Multiple Coulomb scattering of the particles in the detector material introduces a momentum dependence: the deflection by scattering is given as [6]

$$\theta_{plane}^{rms} = \frac{13.6\ MeV}{\beta cp} z \sqrt{\frac{X}{X_0}} \left[1 + 0.038\ \ln \frac{X}{X_0}\right] \tag{3.1}$$

where p, $c\beta$ and z are the momentum, velocity and charge number of the incident particle, and $\frac{X}{X_0}$ is the thickness of the scattering medium in radiation lengths. Using $\frac{X}{X_0} \lesssim 1\%$ as a rough estimate for the radiation length before RICH2 mirror, the estimated contribution to the resolution from multiple scattering is $\sim$1.1 mrad, which is similar in magnitude to the detector granularity. Thus, at low momenta the matching quality deteriorates and is no longer determined by position resolution alone. The momentum dependence is parametrized as

$$\Delta\theta = \sqrt{P_0^{\theta 2} + \frac{P_1^{\theta 2}}{p^2}} \tag{3.2}$$

(and correspondingly for $\Delta\phi$). Here, the term P_0 parametrizes the effect of multiple scattering, whereas P_1 measures the resolution.

We discuss the matching quality as function of the track polar angle θ, to take geometrical effects on the TPC hit and track reconstruction (e.g. the systematic dependence

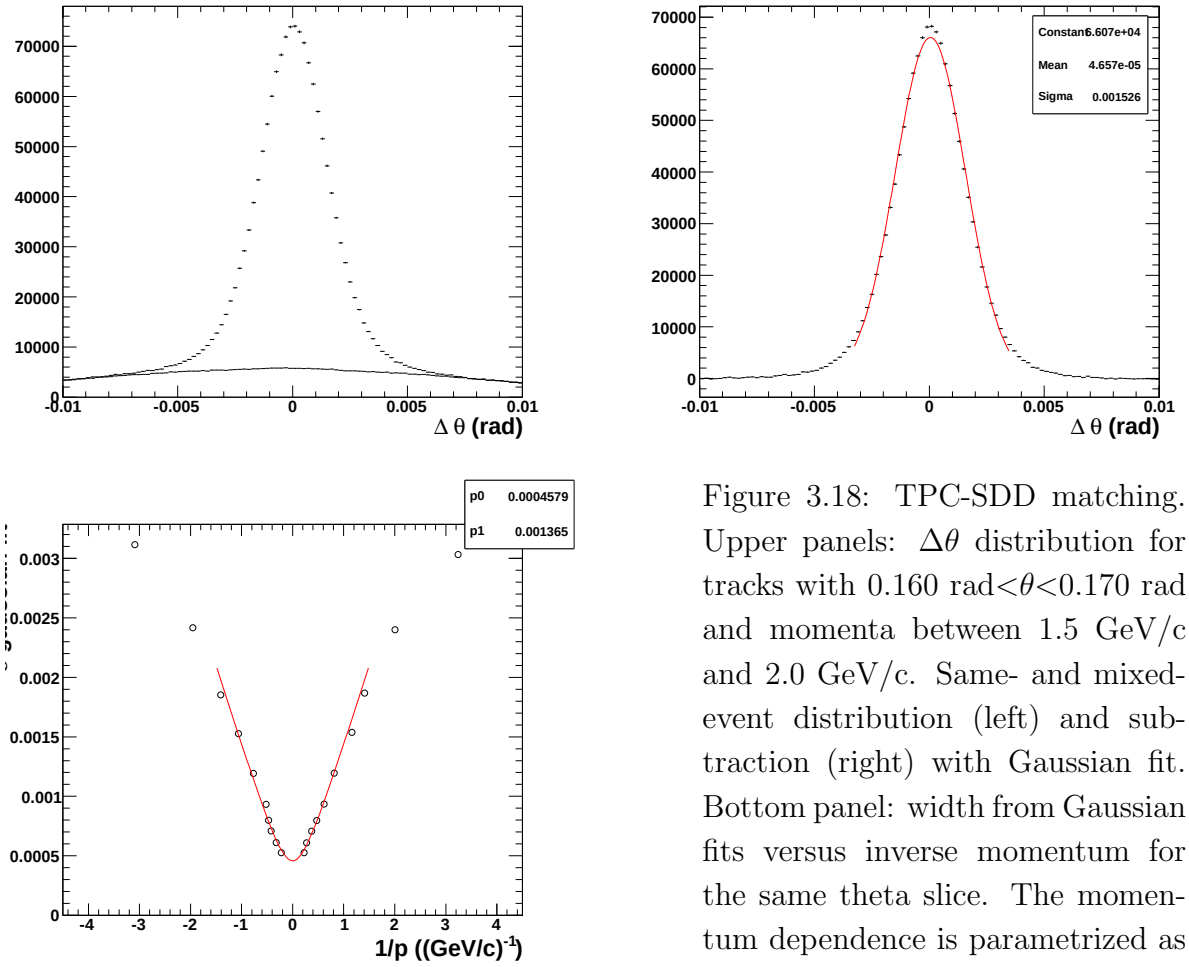

Figure 3.18: TPC-SDD matching. Upper panels: $\Delta\theta$ distribution for tracks with 0.160 rad$<\theta<$0.170 rad and momenta between 1.5 GeV/c and 2.0 GeV/c. Same- and mixed-event distribution (left) and subtraction (right) with Gaussian fit. Bottom panel: width from Gaussian fits versus inverse momentum for the same theta slice. The momentum dependence is parametrized as described in the text.

of the drift time and track length) and the pseudorapidity dependence of particle multiplicity and detector occupancy into account. Furthermore, the resolution of the SDD hits, which are typically reconstructed averaging over the signal induced on several SDD anodes, is worse for hits reconstructed from a single anode alone. For the SDD segments, we distinguish 3 configurations of combinations of hits from SDD1 - SDD2: 1.) multi anode - multi anode, 2.) multi anode - single anode or single anode - multi anode and 3.) single anode - single-anode. About 80% of all SDD segments are of the multi anode - multi anode configuration, the single - single case represents less than 1%.

The procedure is illustrated in Fig. 3.18. In the upper left plot, we present, as an example, the $\Delta\theta$ matching distributions for a sample of electron tracks with polar angle 0.160 rad$<\theta<$0.170 rad and momenta between 1.5 GeV/c and 2.0 GeV/c. We superimpose the distribution from a mixed-event analysis, where each TPC segment from one event is matched to a SDD segment from a different event. The shape of the mixed-event distribution represents random matches of uncorrelated segments. Normalizing the mixed-

event distribution to the tails of the same-event distribution, the contribution of fake matches to the same-event distribution can be quantified, and subtracted. The result of the subtraction is shown in the top right panel of Fig. 3.18, together with a Gaussian fit. In the lower panel, we plot, for the same θ slice, the width σ of the matching distributions obtained in slices of the inverse track momentum. The momentum dependence is fitted according to Eq. 3.2 to determine the parameters P_0 and P_1.

Fig. 3.19 presents, for the three classes of SDD segments, the parameters P_0^θ, P_1^θ, P_0^ϕ and P_1^ϕ as function of θ. As expected, the detector resolution is best in the multi anode - multi anode case and degrades if single anode hits contribute to the SDD segment. The effect is more pronounced in P_0^ϕ than P_0^θ, but can be observed for both coordinates.

To reject random combinations not representing the physical trajectory of any particle, we apply a momentum-dependent 2σ matching cut. This cut rejects combinations includ-

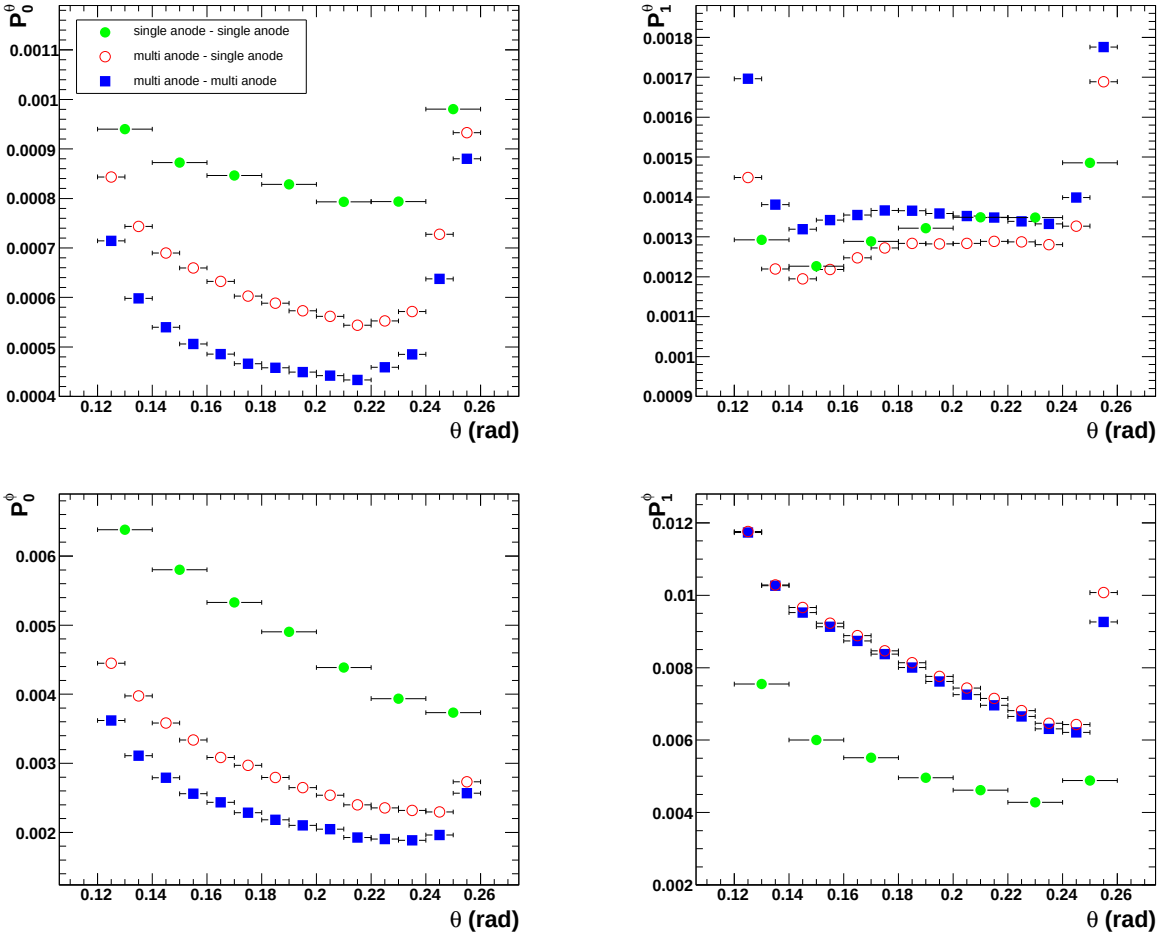

Figure 3.19: TPC-SDD matching: parameters P_0^θ, P_1^θ, P_0^ϕ and P_1^ϕ describing the momentum dependence of the width of the matching distributions, plotted as function of θ.

ing fake SDD or TPC segments as well as secondaries, tracks which do not originate from the target, in particular electrons from photon conversions behind the target (especially in RICH2 mirror). For this reason, in the electron analysis, the SDD-TPC matching cut is an important step in background rejection.

3.8.2 Track quality

Further cuts to ensure track quality and reject fakes are applied on the TPC and SDD segments. For the TPC, we require a minimum number of hits on track. In Fig. 3.20, we present the scatter plot of the number of hits versus the polar angle θ of the TPC segment. The θ dependence reflects the detector geometry inducing a variation of the length of the trajectory contained in the TPC volume. The cut, indicated by the line, is varied accordingly to maintain the efficiency at a constant level.

For the SDD segments, fakes are rejected limiting the maximum allowed opening angle between the two hits combining to the segment. To account for the differences in position resolution, the cut is adapted to the different classes of SDD segments, the multi-multi, multi-single and single-single anode hit configurations. An example of the distribution and the cut is shown in Fig. 3.20.

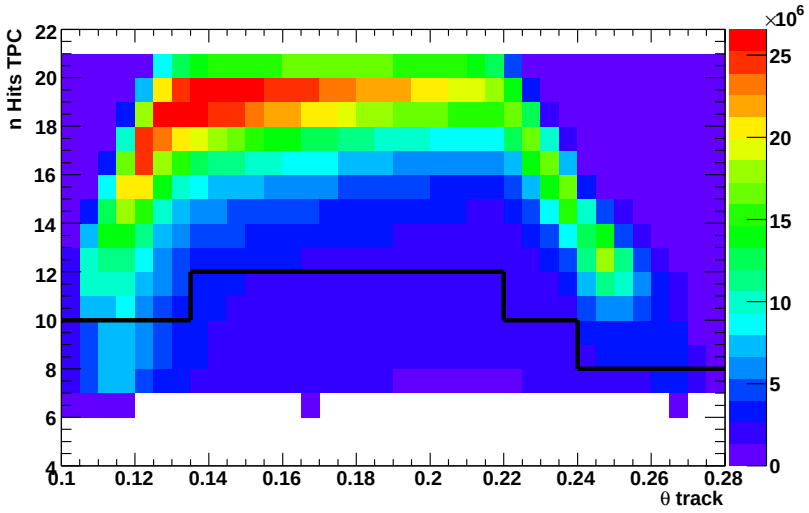

Figure 3.20: Number of hits on the TPC segment versus position of the segment. The θ dependent cut applied in the dilepton analysis is indicated by the line.

3.8.3 Electron identification

Identification of electrons from a heavy-ion collision is a challenging endeavor: charged hadron multiplicities exceed the number of electrons by two to three orders of magnitude.

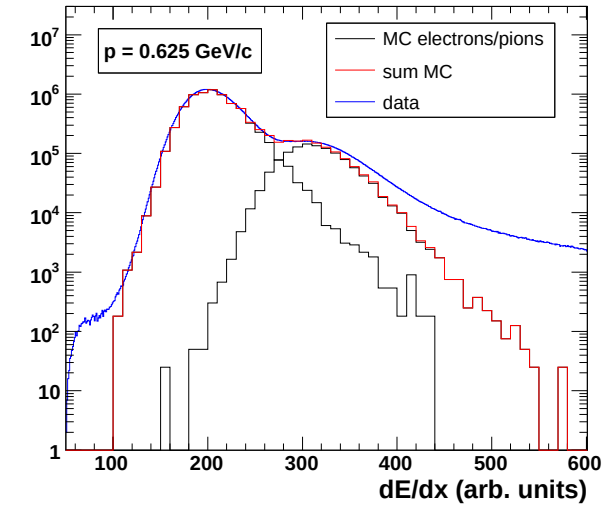

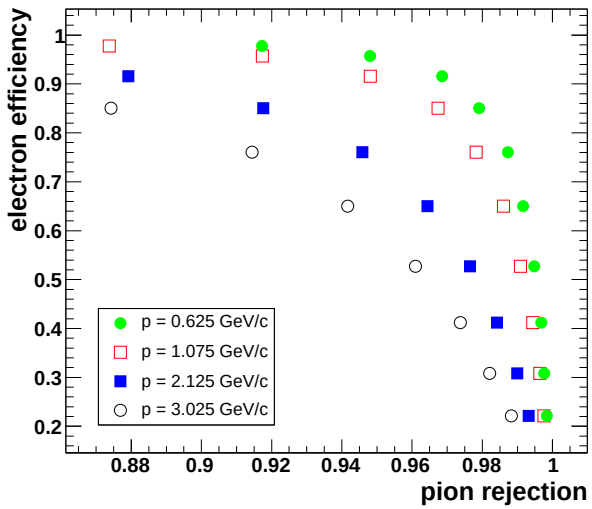

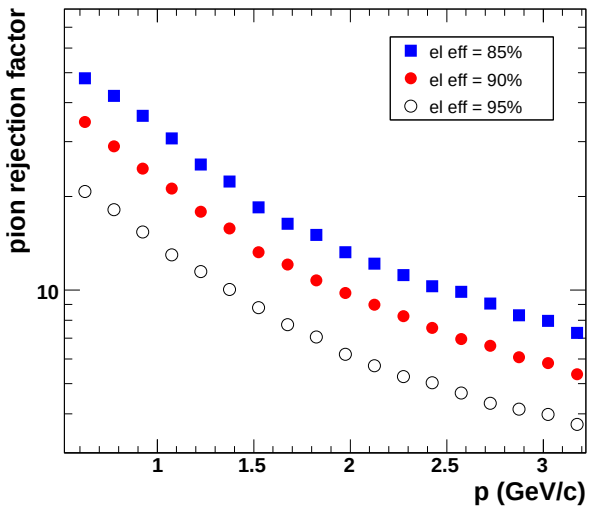

Figure 3.21: TPC electron efficiency and pion rejection. Upper panel: simulated dE/dx distributions (scaled) for electrons and pions and their sum, compared to the data for a momentum of 0.625 GeV/c. Lower panels: electron efficiency versus pion rejection for different momenta (left), pion rejection as function of momentum for given values of the electron efficiency (right).

In CERES, electrons are identified combining the PID information of the RICH and TPC detectors. In this section, we attempt a quantitative estimate of the TPC electron identification capabilities to determine the combined efficiency and rejection power. The TPC electron efficiency and pion rejection can be evaluated using the dE/dx distributions from an Overlay Monte-Carlo detector simulation of the energy deposit in the TPC. In Fig. 3.21, upper panel, the distributions generated for electrons (high dE/dx) and pions (low dE/dx) are compared to the data, for tracks with a momentum of 0.625 GeV/c. In data and simulations, track quality cuts, in particular the cut on the number of TPC hits on track, are applied as in the electron analysis. The sum of both distributions describes the data reasonably well (the tails in the data stem from a small contribution of other particles than electrons and pions, not taken into account in the simulations). To accurately describe the pion relativistic rise, we determine from the data the most

probable value for each momentum slice and scale the pion distribution accordingly. In the lower left panel, the resulting electron efficiency is plotted versus pion rejection (defined in analogy to Section 3.7.5) for different momenta. Along each curve, the lower cut on dE/dx is varied (a constant upper cut is applied in addition). A larger cut value leads to better (higher) pion rejection, but reduces efficiency. The relativistic rise, moving the pion distribution closer to the electron dE/dx, leads to a deterioration of the pion rejection for higher momenta. This effect is studied in detail in the bottom right plot: the pion rejection factor, the inverse of the pion efficiency, is shown as function of momentum for fixed values of electron efficiency. We observe an increase of the fraction of pions misidentified as electrons with momentum.

These results, together with the numbers discussed in Section 3.7.5, lead to the following estimate of the combined particle identification properties: the RICH cut applied in the electron analysis corresponds to an electron efficiency of $\gtrsim 70\%$ and a pion rejection factor of $\sim$1200. The pion rejection achieved with the TPC at 1 GeV/c for 95% electron efficiency is about 15, corresponding to a combined rejection factor of $\lesssim$20000 for an electron efficiency of 70%. The power of the combined RICH-TPC particle identification is illustrated in Fig. 3.22. We plot dE/dx as function of momentum for all particles identified as electrons in the RICH. The comparison with Fig. 3.5, without RICH condition, demonstrates, how powerful pions are suppressed relative to the electrons. For the electron analysis, we apply a momentum dependent dE/dx cut, indicated in the figure: for

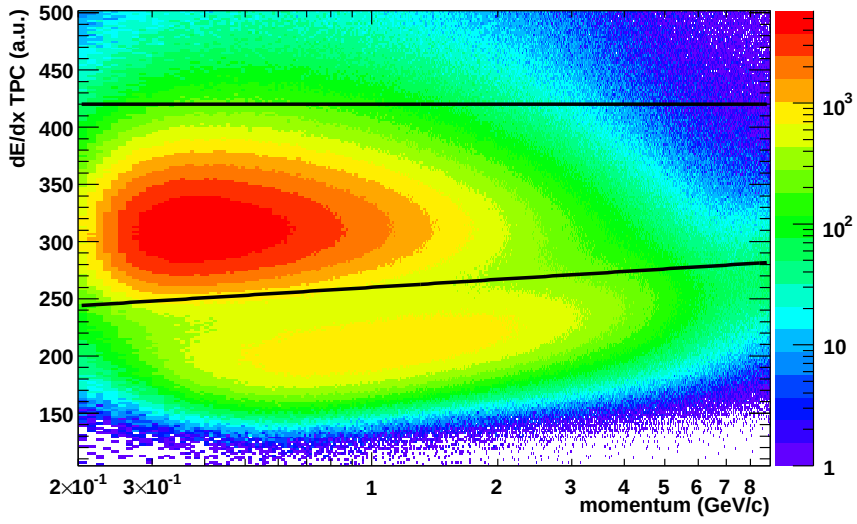

Figure 3.22: TPC dE/dx versus momentum for negative particles. A RICH cut is applied to enhance the contribution of electrons in the sample. The lines indicate the lower dE/dx cut applied to select electrons and reject pions and the upper cut to reject protons and kaons.

higher momenta, the cut threshold increases logarithmically in order to compensate for the relativistic rise of the pions. Furthermore, an upper momentum cut of 9 GeV/c is applied.

3.8.4 Reduction of combinatorial background

Any attempt to reconstruct vector mesons in the dielectron channel in a heavy-ion collision suffers from a severe background of electrons from "trivial" physics sources. The most important contributions are electrons from decays of pseudoscalars, i.e. the π^0 and η Dalitz decays, and photon conversions, with $\pi^0 \rightarrow \gamma\gamma$ the dominant source of photons. Furthermore, due to the large excess of pions over electrons, misidentified pions contribute fake electron tracks. A distinctive feature of conversion and Dalitz pairs is their low pair invariant mass of m_{ee} <200 MeV/c^2, resulting in a small pair opening angle on the on hand and small momentum of the single legs on the other. The reconstruction of such pairs suffers from three very fundamental experimental restrictions: 1.) limited detector acceptance, 2.) limited tracking efficiency for very low momentum tracks and 3.) limited two-track resolution. Hence, in many cases only one out of two legs will be reconstructed or resolved. Combined with other electron tracks, such single legs contribute to the combinatorial background of uncorrelated pairs. The conversion probability for photons is proportional to the radiation length of the material traversed. In the CERES setup, conversions into the electron acceptance originate mainly from the target, the SDD detectors and RICH2 mirror.

An important measure for rejection of combinatorial background consists of a lower transverse momentum cut on the single track level of p_T = 100 to 200 MeV/c. Further rejection steps are discussed below.

Double dE/dx rejection in the silicon detectors

The energy loss of charged particles in the SDD follows a Landau distribution, which approximately reads

$$\frac{d^2N}{dEdx} = \exp(-\frac{x}{2} + e^x)$$

with $x = \frac{E_{loss}-E_{max}}{\sigma}$ where E_{max} and σ denote the most probable energy loss and the width of the distribution, respectively. The Landau distribution is strongly asymmetric, with a tail extending from the most probable energy loss to very high energies. On top of the Landau tail, very close tracks with a separation of a few mrad, as produced by Dalitz pairs and target conversions, are not resolved but registered as a single hit with double amplitude. This signature is a powerful tool to reject fake electron tracks. To maintain high rejection power also in the region between perfect overlap and fully resolved double hits, we sum up the amplitudes of all hits in the SDD within a resummation window

of 7 mrad around each hit on a track and apply the rejection cuts on the resummed amplitude. In Fig. 3.23 we show the correlation of the resummed amplitudes in SDD2 versus SDD1. The peak of common double dE/dx in both detectors is clearly distinguished from the single amplitude peak produced by the majority of tracks (pions). The line indicates the cut applied in the analysis: tracks are rejected if the hits in both SDD detectors have the double resummed dE/dx. This correlated cut minimizes losses of tracks with high amplitude due to the single-hit Landau tail. Conversions occurring in the SDD detectors itself produce only an incomplete track and deposit little energy. They are rejected excluding tracks with hits with very low amplitude in either SDD detector.

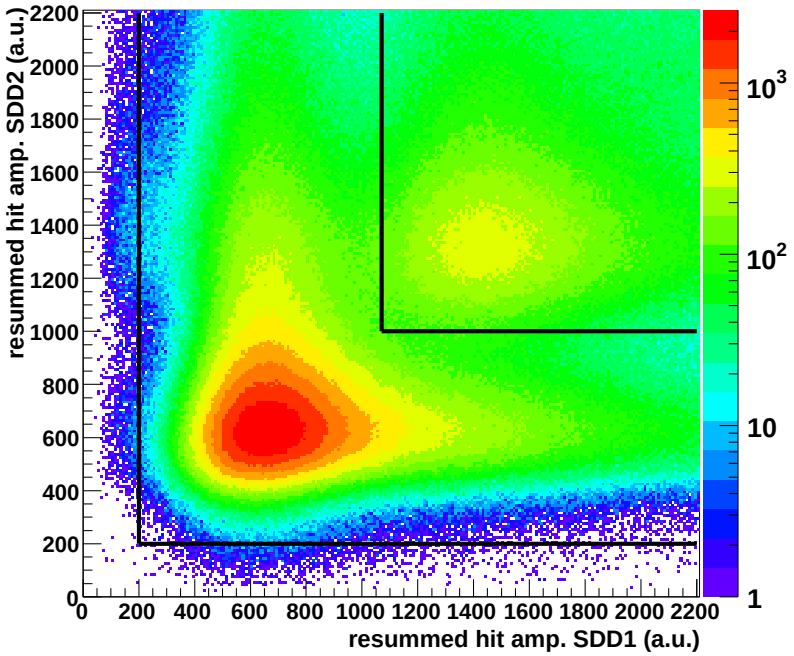

Figure 3.23: Resummed amplitude (dE/dx) of hits in SDD2 versus SDD1. The two dominant islands correspond to single tracks (with dE/dx$\lesssim$1000) and double tracks (dE/dx $\gtrsim$ 1000). The line indicates the cut applied to reject conversions, representing the dominant contribution to the double tracks.

TPC conversion rejection

Photon conversions after the SDD detector can create an electron segment in the RICH and/or the TPC. Typically, most of those TPC segments will not combine into a global track: to a high degree, they are rejected by the requirements of a match to a SDD segment and a high number of RICH hits. The residual contamination of conversion legs with a fake match in the SDD and RICH can be suppressed if both conversion legs are tracked

in the TPC. The signature used for rejection is the presence of another TPC segment of opposite charge with electron dE/dx in close vicinity of the track. In Fig. 3.24, we present for a sample of electrons the correlation between the TPC dE/dx and the opening angle of the closest neighboring TPC segment of opposite charge. At low dE/dx and moderate distance, we observe the 'normal' component of pion tracks. In addition, we distinguish an electron component of close-by segments with high dE/dx. The line indicates the cut applied in the analysis: electron tracks with a TPC segment with a dE/dx higher than 270 within a distance smaller than 15 mrad are rejected as conversion legs.

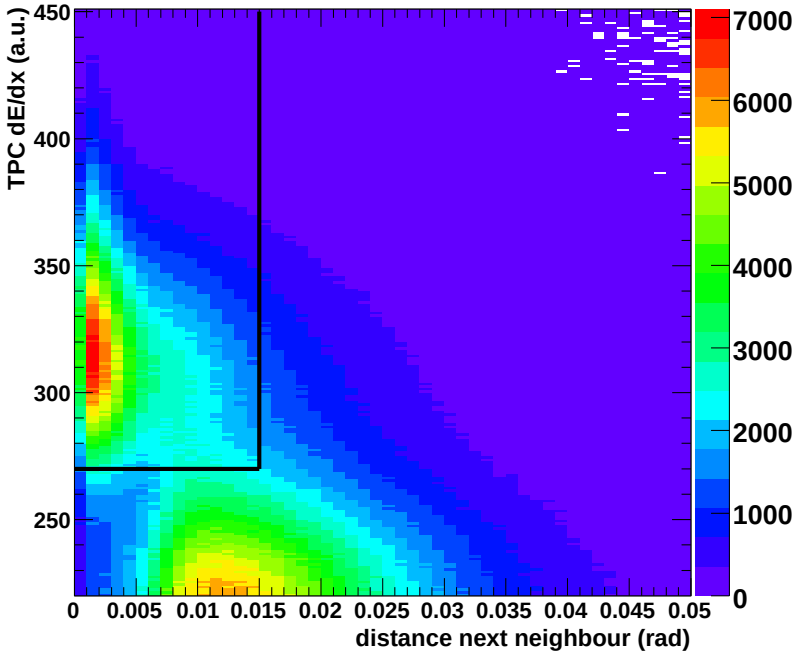

Figure 3.24: TPC dE/dx versus opening angle of the closest TPC segment of opposite charge in vicinity of an electron track. The island at very small distances and high dE/dx is indicative for conversions. The lines represent the rejection cut applied in the analysis.

A similar strategy is pursued with the soft TPC segments obtained from the dedicated low-momentum tracking. Here, some comments on the observed properties of these tracks are at order. In the top left panel of Fig. 3.25, we plot TPC dE/dx versus momentum of the soft tracks. We observe a remarkably strong component of very soft electrons (no RICH condition is applied in this figure). Their origin is clarified by the distribution of TPC dE/dx plotted versus the track polar angle, shown in the top right panel. At θ values beyond the single track acceptance of the dilepton analysis indicated by the lines, a strongly enhanced electron contribution is visible. This points to conversions in the TPC mechanical support as source of the electrons. This suspicion is confirmed by the

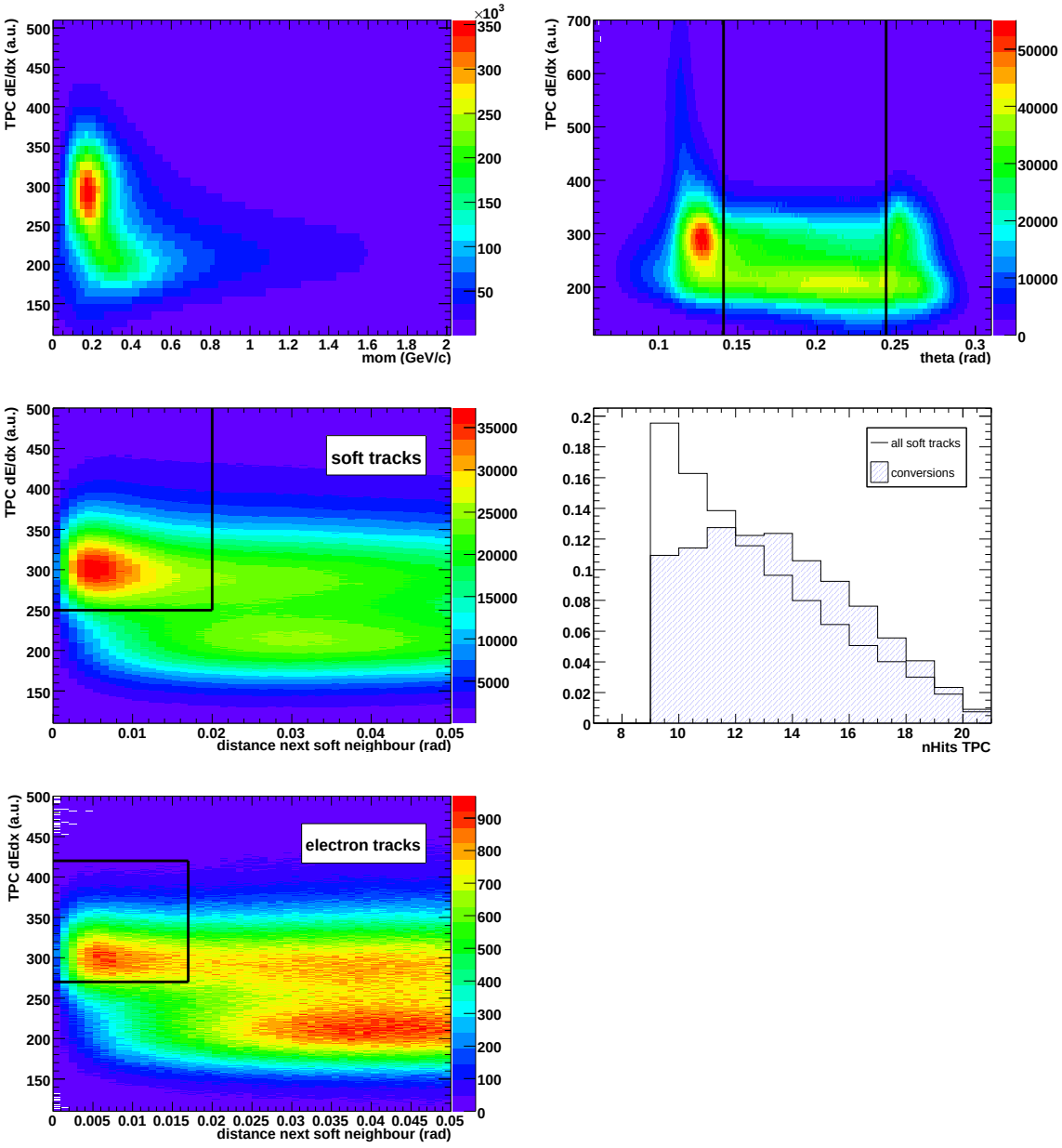

Figure 3.25: Properties of the soft TPC segments reconstructed by the dedicated low-momentum tracking. Upper left panel: TPC dE/dx versus momentum for negative tracks. Upper right: TPC dE/dx versus segment polar angle. At θ values beyond the single track acceptance of the electron analysis indicated by the lines, an enhanced electron contribution from conversions in the TPC support is visible. Center left: TPC dE/dx versus opening angle of the next neighbor of opposite charge among pairs of soft tracks. The cut to identify conversion pairs selecting close segments with electron dE/dx is indicated by the lines. Right: number of hits on track, for all soft tracks and a conversion sample. Bottom panel: Conversion rejection against soft segments: TPC dE/dx versus opening angle of the next neighbor soft track for each global electron track. The soft track sample was cleaned from conversion pairs before pairing. Global electron tracks are rejected, if a close soft track with high dE/dx is found in vicinity, as indicated by the line.

distribution of the opening angle between any soft track and its closest neighbor of opposite charge among the soft tracks, presented in the center left panel: a pronounced peak at very small distances is seen, the distinctive signal for conversions. The lines in the figure indicate the cut applied to identify conversion pairs composed of two soft tracks. In the center right panel, we present the distribution of the number of TPC hits on track. It is peaked at the lowest possible number of 9 hits allowed by the production cuts. This indicates, not surprisingly, an important contribution of fake segments due to the relaxed conditions on the matching between the individual hits on track in the low-momentum tracking. To investigate the distribution for real tracks, we apply the cut indicated in the center left panel to `select` a conversion sample. The distribution obtained for these tracks is superimposed on the plot: it is peaked at a value of about 13 hits, distinguishing the real tracks from fakes.

These observations motivate the rejection strategy adopted with the soft tracks. We require a minimum number of TPC hits for any soft track considered for rejection. In the next step, soft tracks are paired among each other to identify conversion pairs. To maintain high efficiency in the following step, the identified conversions are excluded from the sample of soft tracks used for further rejection. Furthermore, all soft tracks outside the θ interval indicated in the top right plot are excluded. The rejection step proper consists of pairing the sample of 'good' electron tracks established by the standard TPC tracking with the remaining soft tracks. If in the vicinity of an electron track a soft electron track with momentum below 0.5 GeV/c is found, it is considered a conversion leg and rejected. The final rejection step is illustrated in the bottom panel of Fig. 3.25, where the TPC dE/dx of the closest soft track is plotted versus its opening angle with respect to any good electron track.

High momentum pion rejection

Clean identification of electrons via the TPC dE/dx information gets increasingly difficult for high momentum tracks, due to the relativistic rise of the pion specific ionization (Section 3.8.3). Although the TPC dE/dx cut is increasing with momentum to compensate for the effect, a small fraction of the pions will survive the cut. Since the single-electron p_T spectra steeply decrease with momentum, this induces a significant pion contamination of the electron sample.

To improve pion rejection at high momenta, we exploit the fact that pions above the threshold momentum of $p \approx 4.7$ GeV/c emit Cherenkov radiation. The emitted photons can be reconstructed in the RICH detector using the free radius ring search, as was demonstrated in Section 3.7.8. In Fig. 3.26, we plot the reconstructed radius as function of the track momentum for the particles identified as electrons by the TPC. At low momenta, the majority of the particles has the asymptotic radius of 31 mrad expected for electrons. At high momenta, a pion component with a momentum dependent radius

can be clearly distinguished. The structure is the same as observed in Fig. 3.17 for a dedicated pion sample. To reduce the contamination, any particle with a radius similar to the expected pion radius is excluded from further analysis. The cut is indicated by the lines. At very high momenta $\gtrsim$8 GeV/c, the Cherenkov radius for pions approaches the asymptotic value expected for electrons. We adjust the cut to avoid rejection of electrons along with the pions.

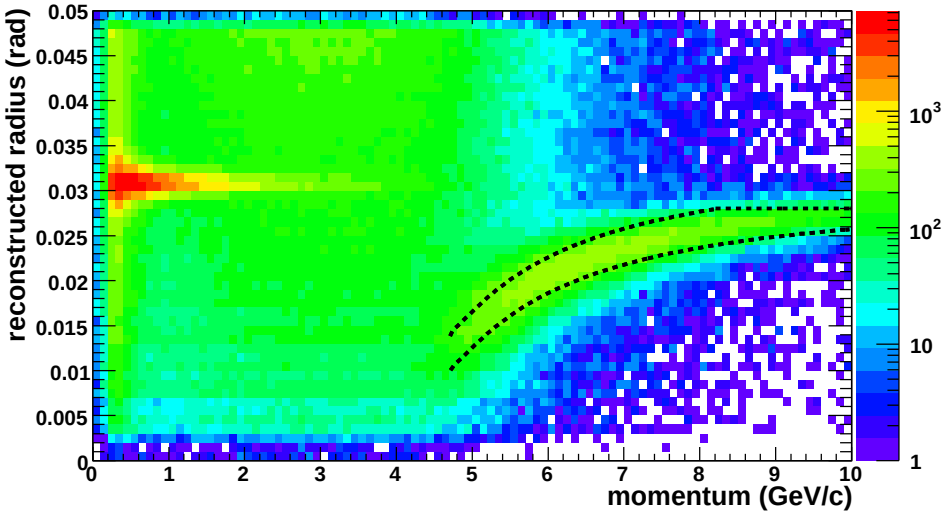

Figure 3.26: RICH reconstructed radius versus momentum for electron tracks, selected via TPC dE/dx. The pion contamination of the sample is visible at high momenta, for which pions produce Cherenkov radiation. The lines indicate the rejection cut applied in the analysis.

3.8.5 Pairing and subtraction of combinatorial background

After the background rejection, all identified electrons and positrons within one event are combined to pairs, henceforth referred to as unlike-sign pairs. The Lorentz invariant pair mass m_{inv}, defined as the root of the squared sum of the four-momenta, can be calculated from the individual three-momenta and the pair opening angle Θ_{ee}, neglecting the electron mass (which is small compared to the electron momenta):

$$m_{inv}^2 = (p_{e^+} + p_{e^-})^2 = (E_{e^+} + E_{e^-})^2 - (\vec{p}_{e^+} + \vec{p}_{e^-})^2 \approx 2\,|\vec{p}_{e^+}||\vec{p}_{e^-}|(1 - \cos\,\Theta_{ee})$$

It is impossible to distinguish between correlated electron-positron pairs originating from a vector meson or Dalitz decay and an accidental combination of tracks from separate sources. Hence, the observed unlike-sign pair distributions are composed of the actual signal S of correlated dielectrons N_{+-}^{corr} and the `combinatorial background` pairs B:

$$N_{+-}^{total} = N_{+-}^{corr} + N_{+-}^{uncorr} = S + B$$

To extract the physics signal from the observed distribution of unlike-sign pairs, we have to determine the amount of background pairs and the shape of the background distribution. This can be accomplished using the same-event like-sign invariant mass distribution or (to some extent) with the mixed-event technique. In the first method, the uncorrelated unlike-sign background is estimated via the like-sign electron pairs. We can safely assume that these are uncorrelated: the most important physical source of electrons of equal charge is the decay of $\pi^0 \to e^+e^+e^-e^-$, which is not only suppressed by about a factor 400 relative to the π^0 Dalitz decay but also charge symmetric, and hence negligible. A further possible source of like-sign electron pairs is a Dalitz decay followed by a conversion of the emitted photon, e.g. $\pi^0 \to e^+e^-\gamma \to e^+e^+e^-e^-$. This process is suppressed by the conversion probability X/X_0 of a few percent and more so by the conversion rejection cuts applied in the analysis and can also be neglected. Both charges have the same acceptance and track reconstruction efficiency, as demonstrated in Fig. 3.27, where the numbers of reconstructed electrons and positrons per event, after all rejection cuts, are presented. The asymmetry in the number of negative and positive electron tracks is very small, the mean numbers of electrons and positrons nearly identical. On top of the measured numbers we superimpose Poissonian distributions with equal mean as in the data. The comparison demonstrates that the measured distributions are nearly Poissonian.

For Poissonian statistics, the mean unlike-sign combinatorial background can be eval-

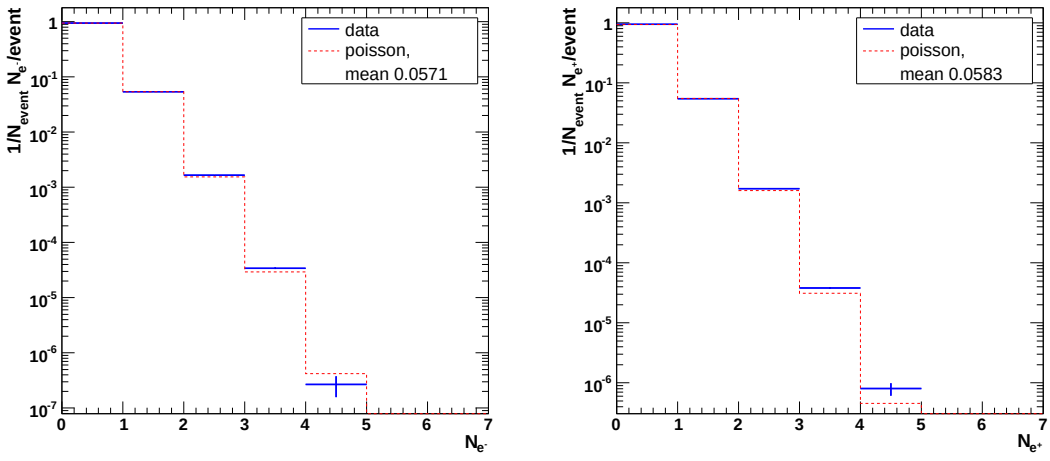

Figure 3.27: Number of reconstructed electron/positron tracks per event. The normalized distributions are compared to Poissonian distributions with equal mean, respectively for negative and positive tracks.

uated as twice the geometrical mean of the like-sign pairs:

$$B = 2 \cdot \sqrt{N_{++} \cdot N_{--}} \tag{3.3}$$

with the r.m.s. deviation

$$\sigma_B^2 = N_{++} + N_{--}$$

Using

$$N_{++} \approx N_{--} \equiv N_{like}$$

we obtain

$$B = 2 \cdot N_{like}$$

and

$$\sigma_B^2 = 2 \cdot N_{like} = B \tag{3.4}$$

The physics signal is obtained by subtraction

$$S = N_{+-}^{tot} - B$$

with the variance

$$\sigma_S^2 = \sigma_{N_{+-}^{tot}}^2 + \sigma_B^2 = (S + B) + B = S + 2 \cdot B \tag{3.5}$$

Since $B >> S$ for the open pair signal, the error of the signal is, in very good approximation,

$$\sigma_S = \sqrt{2 \cdot B} \tag{3.6}$$

If the background subtraction is carried out in differential spectra, e.g. in bins of an invariant mass spectrum, the statistical fluctuations of the like-sign background severely contribute to the error of the signal. Such fluctuations can be avoided determining the `shape` of the background distribution with the mixed-event technique. In this approach, a large number of uncorrelated unlike-sign pairs is obtained mixing each track from a given event with all tracks of opposite charge from several different events, generating a smooth high-statistics background spectrum. This reduces the `local` statistical error of the signal to $\sqrt{B}$, i.e. by a factor $\sqrt{2}$ relative to Eq. 3.6. In the event mixing, however, the absolute normalization of the background, Eq. 3.3, is lost. The scale factor applied to the smooth background distribution is obtained by comparison to the like-sign background (and can not be determined analytically). This reintroduces the contribution σ_B, Eq. 3.4, as a `global` systematic error.

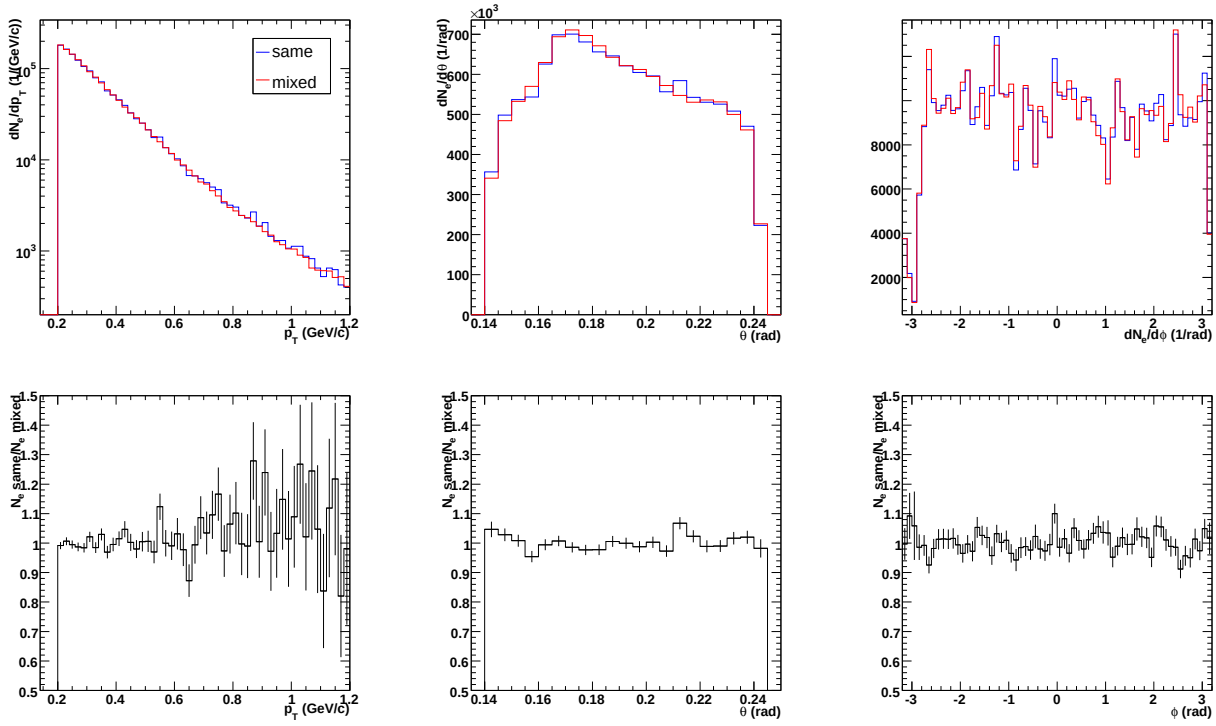

Figure 3.28: Comparison of single leg properties of tracks used for the same- and mixed-event spectra: transverse momentum, θ and ϕ distributions, as well as the ratios same- to mixed-event. The mixed-event distributions are normalized to the same-event distributions and the ratios scaled correspondingly.

For the validity of the event mixing procedure, the background has to be generated from a sample of tracks physically equivalent to the tracks contributing to the same-event unlike-sign pairs. To prevent any bias of the generated pairs with respect to event multiplicity (i.e. to avoid tracks from high-multiplicity events to be overrepresented among the pairs) we mix only events with similar centralities. To avoid any bias introduced by inhomogeneities in the centrality distribution, it is important to have a large 'pool' of events to mix among each other (the size of which is technically limited by the memory available for the data analysis). In our implementation, this pool contains 10 bursts, comprising ∼2500 events. Each event is mixed with up to 10 other events, but with none of them twice, to avoid autocorrelations. In Fig. 3.28, we compare the basic properties of single tracks contained in the mixed- and same-event selection. The differential same-event transverse momentum p_T, θ and ϕ distributions are confronted with the mixed-event distributions, appropriately scaled to account for the intrinsically much higher statistics in the mixed-event case. The same- and mixed-event single track distributions display excellent agreement. This impression is confirmed by the ratios (scaled accordingly), presented in the bottom panels. They are flat, which proves the absence of any systematic

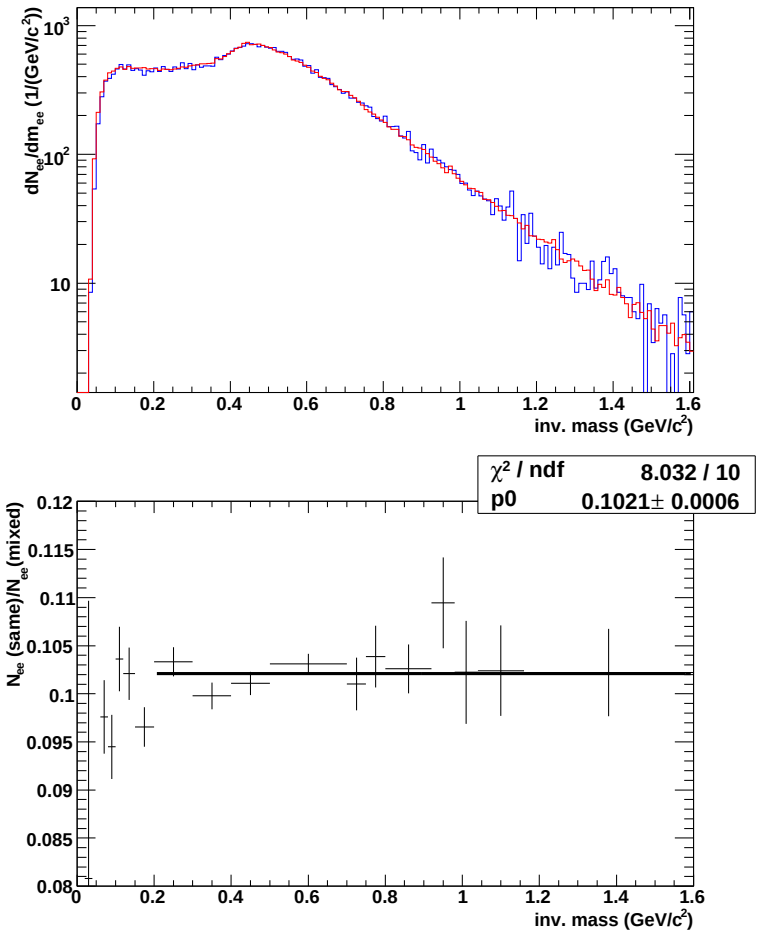

Figure 3.29: Same-event like-sign versus mixed-event like-sign background. Upper panel: comparison of both invariant mass distributions, the mixed-event background is normalized to the same-event distribution. Lower panel: ratio of the two.

bias, and, within the error bars, perfectly consistent with 1.

In the upper panel of Fig. 3.29, the same-event like-sign and the mixed-event unlike-sign pair invariant mass background distributions are superimposed. The ratio of the two, shown in the lower panel, is flat for masses m_{inv} >200 MeV/c^2, at a level of about 0.1 (reflecting the approximate 10:1 ratio of the events used for mixing). In the low-mass region of $m_{inv} < 200$, corresponding to small pair opening angles, the ratio deviates from this flat behavior, as an effect of small-angle correlations between tracks from the same event naturally not reproduced in the event mixing. Most importantly, the RICH reconstruction introduces a positive correlation: 2 rings for different predictors are allowed to share the same hits. Hence, the presence of an electron enhances the probability to create a fake ring due to pick-up of hits from true rings and fluctuations of the density of background hits. Isolation cuts and the Dalitz rejection induce anticorrelations. Consequently,

the mixed-event background can not be used to obtain a reliable low-mass signal. For invariant masses below 200 MeV/c^2 we therefore subtract the like-sign background. For higher masses we use the mixed-event background, downscaled to the level of the like-sign background. The scale factor is obtained from a constant fit to the same- over mixed ratio, as presented in the bottom panel of Fig. 3.29. It is important to note that the error on the fit result is only at the level of a few `tenth of a percent` - a variation of the scale factor of the order of a few `percent` would be enough to induce strong variations of the net signal.

3.8.6 Signal quality

Optimization of the analysis cuts requires an objective measure of signal quality. The so called `effective signal` S_{eff},

$$S_{eff} = \frac{S^2}{S + 2B} \tag{3.7}$$

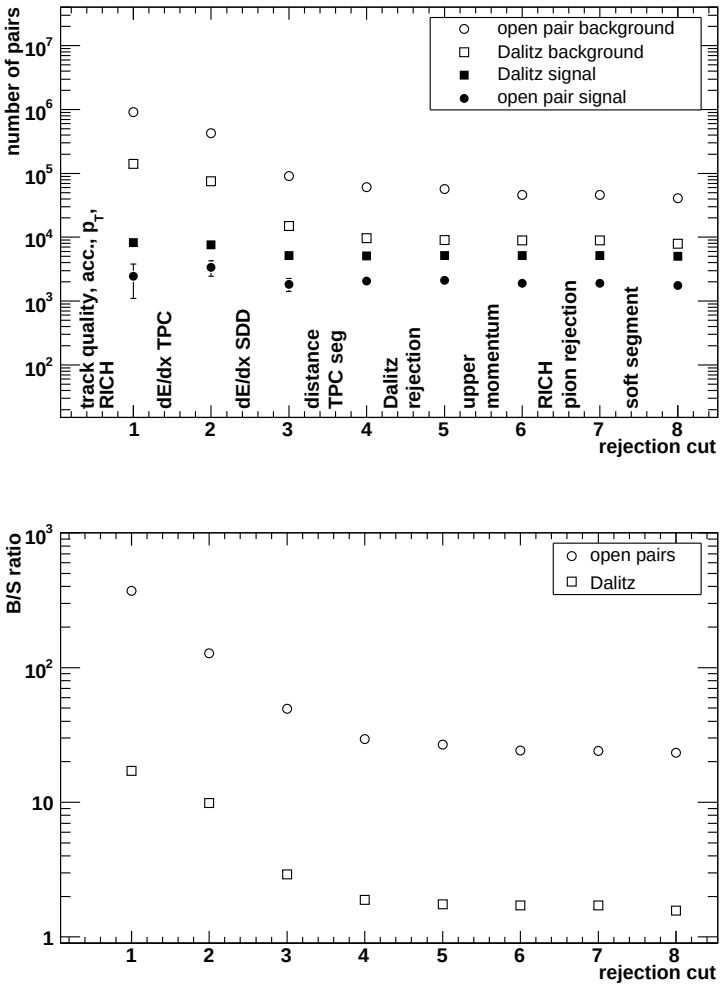

Figure 3.30: Pair yield and background for the sequence of analysis cuts. Upper panel: The number of signal and background pairs with opening angle larger than 35 mrad, plotted separately for invariant mass windows m_{inv}<200 MeV/c^2 ("Dalitz pairs") and m_{inv}>200 MeV/c^2 ("open pairs"). Lower panel: ratio background over signal for the two invariant mass intervals.

(the inverse relative error squared), provides a means to arbitrate between the background reduction achieved by a cut on the one hand and the unavoidable signal loss on the other hand. In each rejection step, the cut is varied and the cut value chosen to maximize S_{eff}, or, equivalently, S^2/B, since B>>S. We abstain, however, from optimizing directly the open pair signal, since that approach would bear the danger to foster upward fluctuations and produce spurious results. We rather use the pairs with an opening angle larger than 35 mrad in the invariant mass region m_{inv} <200 MeV/c^2, optimizing the open pair signal along with the Dalitz signal. This procedure relies on the observation that the single track properties (and efficiencies) of legs from Dalitz decays are very similar to the open pairs (compare Section 5.5).

In Fig. 3.30, we present the number of background pairs and the signal yield for the sequence of analysis cuts, separately for Dalitz and open pairs. The plot starts after the RICH electron identification. Comparison of the effect of the cuts on signal and background illustrates the power of the background rejection: the background, for Dalitz as well as open pairs, is reduced by about a factor of 20, whereas the signal is, within errors, nearly constant. This reduces the background-to-signal ratio, shown in the lower panel, from about 400 to 25 for the open pairs, and from ∼20 to 1.6 for the Dalitz region.

4 The GENESIS event generator

The GENESIS event generator [29, 32, 79, 80, 81] was developed to simulate the production of electron pairs from hadron decays in proton-proton (pp), proton-nucleus (pA) and nucleus-nucleus (AA) collisions. In the invariant mass range $m_{inv} \lesssim 1$ GeV/c^2, covered by CERES, the dilepton yield is dominated by the decays of neutral light mesons, the Dalitz decays $PS \to e^+e^-\gamma$ of the pseudoscalars π^0, η, $\eta\prime$, the direct decays $V \to e^+e^-$ of the vector mesons ρ and ϕ, and both types of decay of the ω meson. The contribution of open charm decays is negligible [82]. This so-called `hadronic cocktail` provides a reference for the physics expected from `vacuum properties` of the hadrons. Any deviation indicates new physics, e.g. in-medium effects. The simulation proceeds in 3 steps: 1.) generation of the mother particles, 2.) decay, using known branching ratios and simulating the correct decay kinematics, and 3.) convolution of the generated electron momenta with experimental resolution and acceptance.

The production cross sections of most light mesons were measured in several experiments in p-p or p-A collisions, including the CERES experiment [30] (for a compilation, see [29] and references therein). The data situation is less favorable for A-A. For Pb-Au collisions, we take the yields relative to the π^0 production cross-section from a thermal model [87, 88] where measurements are not available. The statistical model of particle production in heavy-ion collisions accurately describes a wealth of existing data on strange and non-strange meson and baryon production, as shown in Fig. 4.1. The cross sections

Particle	Decay	σ/σ_{π^0} (p+A)	σ/σ_{π^0} (Pb+Au)	BR
π^0	$e^+e^-\gamma$	1	1	$(1.198 \pm 0.032) \times 10^{-2}$
η	$e^+e^-\gamma$	0.053	0.085	$(6.0 \pm 0.8) \times 10^{-3}$
ρ^0	e^+e^-	0.065	0.094	$(4.67 \pm 0.09) \times 10^{-5}$
ω	$e^+e^-\pi^0$	0.065	0.069	$(5.9 \pm 1.9) \times 10^{-4}$
ω	e^+e^-	0.065	0.069	$(7.14 \pm 0.13) \times 10^{-5}$
ϕ	e^+e^-	0.0033	0.018[1]	$(2.98 \pm 0.04) \times 10^{-4}$
η'	$e^+e^-\gamma$	0.009	0.0078	$\approx 5.6 \times 10^{-4}$

Table 4.1: Relative production cross sections and branching ratios for light mesons implemented in GENESIS [83, 81]. The relative cross sections for Pb-Au collisions are taken from the thermal model [87].

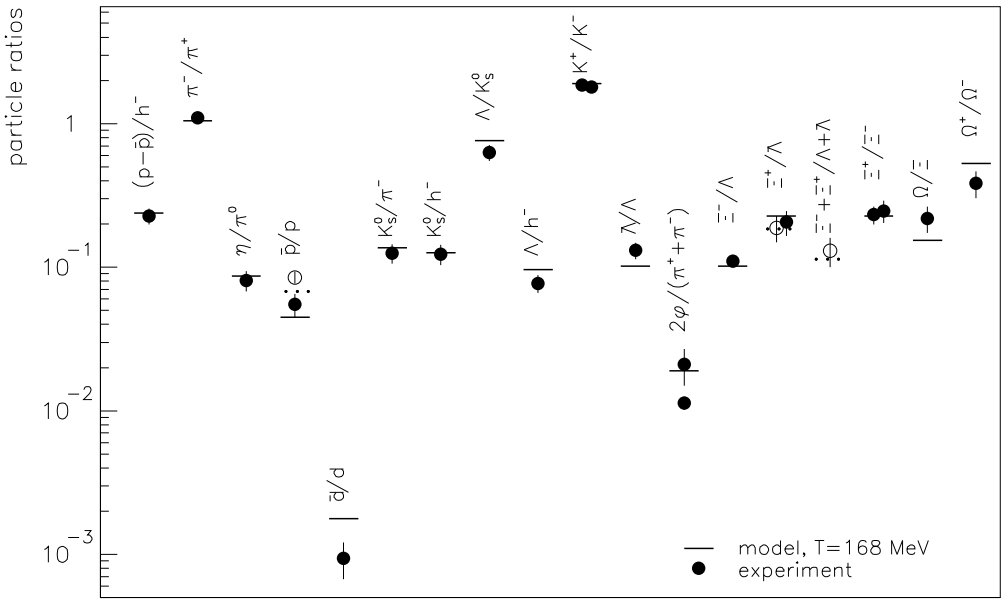

Figure 4.1: Comparison of measured particle ratios and the expectation based on the thermal model [87, 88]

and branching ratios [83, 81] contained in GENESIS are summarized in Table 4.1[1]. For comparison between the cocktail and the measured yield of electron pairs, the cocktail is scaled relative to the number of charged particles applying the measured ratio N_{π^0}/N_{ch}= 0.43 [84].

The kinematics of the generated particles factorize into rapidity (y) and transverse momentum (p_T) distributions. While the widths of the hadron rapidity distributions decrease with particle mass in proton induced collisions, this is not observed in lead induced collisions [89]. Hence, the measured rapidity distribution of negative hadrons measured by NA49 [90] was used for all hadrons.

The collision system is modelled in a state of collective transverse expansion, which is based, among others, on the observation [91] that the inverse slope parameters T_0 of the transverse momentum spectra of produced hadrons, except pions, systematically increase with mass, $T = 0.175 + 0.115 \cdot m(\mathrm{GeV/c^2})$, as shown in Fig. 4.2 [92].

Pion distributions have been measured by CERES [93], NA49 [94], NA44 [95], and WA98 [96]. The transverse momentum distributions are exceptional in that they can not be described by a single exponential, due to the important contribution of pions from

[1]To accommodate for the recent results [85], as well as [86], the contribution of the ϕ meson in Pb-Au collisions is scaled down by a factor 0.7 with respect to the value given in Table 4.1.

resonance decays. The inclusive m_T distribution for neutral pions measured by WA98 is extrapolated to small m_T using the charged pion distribution from NA44. The m_T distribution is parametrized as follows:

$$E\frac{d^3\sigma}{d^3p} \sim a_1 e^{\frac{-m_T}{T_1}} + a_2 e^{\frac{-m_T}{T_2}} + a_3 e^{\frac{-m_T}{T_3}}$$

with

$$a_1 = 1, \qquad a_2 = 0.139, \qquad a_3 = 0.107$$

$$T_1 = 0.1 \text{ GeV}, \qquad T_2 = 0.23 \text{ GeV}, \qquad T_3 = 0.102 \text{ GeV} .$$

For Dalitz decays, the decay cross section is described as the product of the Kroll-Wada expression [97] for a relativistic point source and a form factor F, parametrizing the electromagnetic structure of the particle:

$$\frac{d\sigma}{dq^2} = \frac{d\sigma}{dq^2}_{pointlike} \cdot F(q^2)$$

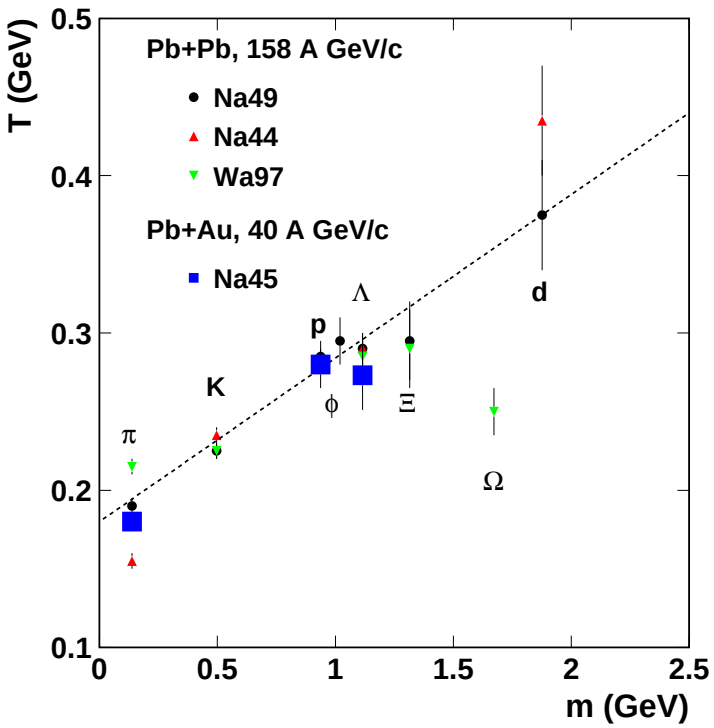

Figure 4.2: Inverse slope parameter T fitted to hadron spectra from central Pb-Pb collisions at the SPS [92].

The form factors are fitted to the Lepton-G experimental data [98, 99]. For the π^0 and η Dalitz decays, the pole approximation $F(M^2) = (1 - bM^2)$ is used, the decays of the ω and $\eta\prime$ are described by a Breit-Wigner function

$$|F(M^2)|^2 = \frac{m_V^4}{(M^2 - m_V^2)^2 + m_V^2\Gamma_0^2}$$

Where M is the e^+e^- invariant mass. For two-body decays of ω and ϕ, the relativistic Breit-Wigner formula is used:

$$\frac{dR}{dM^2} = \frac{[1 - (\frac{m_{th}}{M})^2]^{3/2}}{(M^2 - m_V^2)^2 + m_V^2{\Gamma_0}^2}$$

Here, m_V is the mass of the vector meson, $m_{th} = 3m_\pi$, Γ_0 is the width of ω or ϕ. Due to its large width of $\sim$ 150 MeV, the above formula is not precise for the ρ decay. The correct description, evaluated by [100], was implemented into GENESIS. All decays are assumed isotropic in the rest frame of the decaying particle, except for the Dalitz decays, which follow a $1 + \cos^2\theta$ distribution with respect to the virtual photon direction.

To allow for a meaningful comparison with the data, the generated spectrum is folded with the mass resolution, including bremsstrahlung effects, and subject to the same filters as the data, namely acceptance, p_T, and opening angle cut. To the mass resolution contribute the momentum resolution, parametrized as

$$\frac{\Delta p}{p} = \sqrt{(2\%)^2 + 1\% \cdot (p(\mathrm{GeV/c^2}))^2}$$

and the pair opening angle distribution

$$\sigma_{\theta_{ee}} \approx (\sqrt{2}\sigma_\theta^2 + \sin^2\theta\sqrt{2}\sigma_\phi^2)$$

where $\sigma_\theta \approx$0.6 mrad and $\sigma_\phi \approx$3 mrad. The kinematic cuts are transverse momentum $p_T >$200 MeV/c^2, pair opening angle $\Theta_{ee} >$0.035, and pseudorapidity acceptance 2.1$<\eta<$2.65. In Fig. 4.3, we present the cocktail generated for Pb-Au collisions at 158 AGeV. The contributions of the individual sources are indicated.

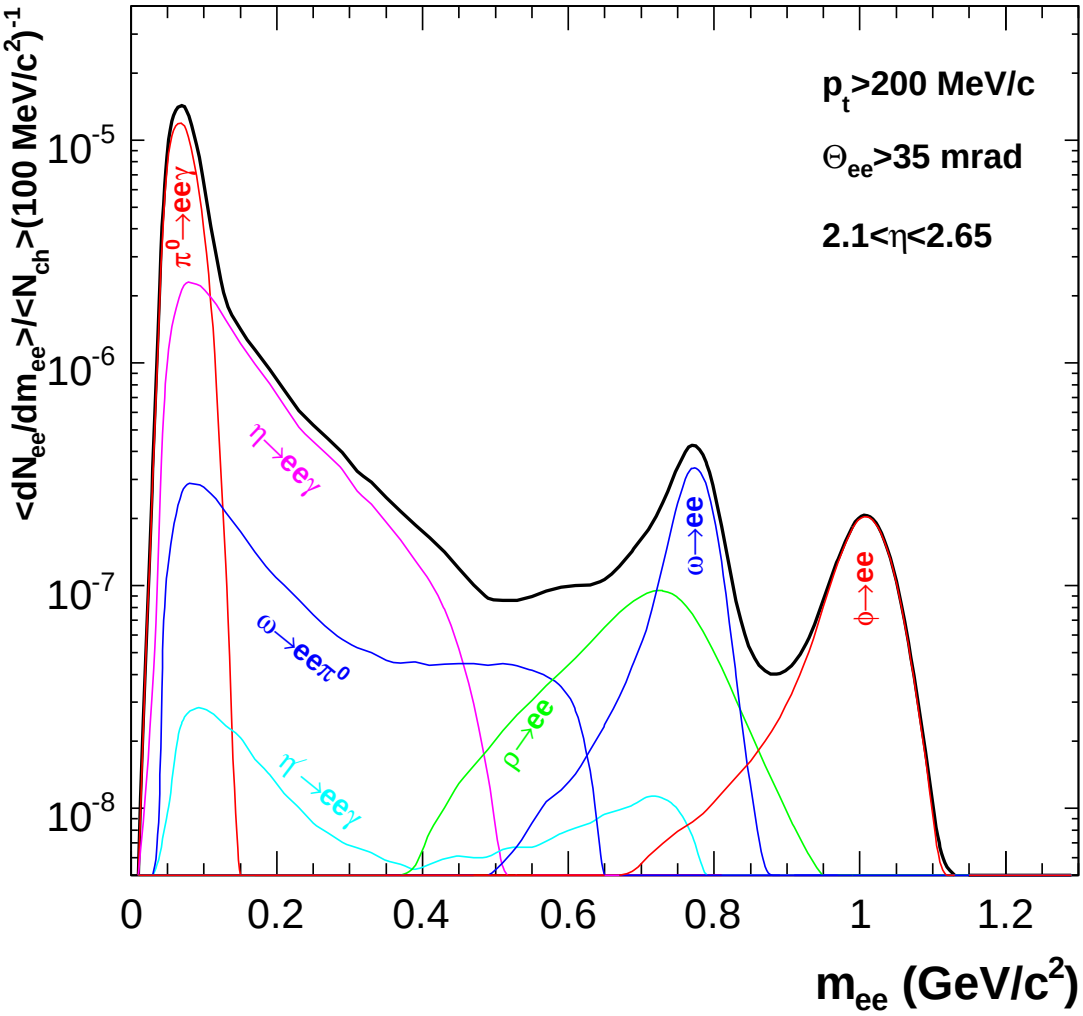

Figure 4.3: The hadronic cocktail folded with momentum and opening angle resolution after applying kinematic cuts and bremsstrahlung effects. The individual contributions to the sum (black line) are shown.

5 Detector simulations

Absolute normalization of the measured spectra (invariant mass, transverse momentum, ...) requires quantitative understanding of the pair reconstruction efficiency. For this purpose, Monte Carlo (MC) simulations of the detector are indispensable. Ideally, the simulation would comprise the electron signal from decays of pseudoscalar and vector mesons as well as all the other 'background' hadrons and leptons generated in the heavy-ion collision. However, the realistic simulation of a full event is extremely complex and consumptive in terms of computing time. Hence, we use the `Overlay Monte Carlo` technique, embedding the generated signal into events from the real data. In this approach, the data tracks act as a background to the MC generated pairs and are analyzed along with those. The method provides for a realistic description of the influence of detector occupancy on the reconstruction efficiency and allows a reliable estimate of efficiency losses during the Dalitz and conversion rejection steps due to hadronic background tracks.

The simulation proceeds in the following steps:

- Source generation: the decays of vector and pseudoscalar mesons are simulated with the CERES event generator GENESIS, described in Chapter 4. The output consists of the final state electron pairs.

- Energy deposit: the generated particles are passed through a Geant3 [101] simulation of the CERES spectrometer, including the complete detector geometry and a description of all detector materials. Geant3 provides the energy deposit, 'transporting' the generated particles through the material, and simulates the physical energy loss processes (ionization, Cherenkov radiation etc.). The Geant output consists of hits which convey the information where a given particle deposited what amount of energy.

- Digitization and overlay: the Geant hits are converted to digi-hits, eventually applying experimentally established detector effects not included in Geant. Digi-hits and real data are merged at the lowest level in the hierarchy of signal processing: the deposited energy is translated into the actual detector response, formatted according to the output of the front-end electronics for every detector subsystem and embedded into the data pixels [102]. The digitization parameters (e.g. gain factors, diffusion constants, thermal noise) are carefully tuned to closely reproduce the detector response from real data.

- Reconstruction: the simulated signal, along with the real data, is passed through the reconstruction software producing hits and tracks from the raw data. The output is produced in step2 format. The information on the generated hits is preserved on the output ROOT tree, so that the digitized hits in data format can be assigned to their MC origin.

- production and data Analysis: the step2 simulation output is fed into the step3/step4 production software. This allows to analyze the MC output in step3 format with the standard analysis routines used for data analysis, e.g. in order to evaluate reconstruction efficiencies.

5.1 SDD

Geant simulates the ionization process of the charged particle traversing the silicon wafer and calculates the energy deposit. The corresponding charge is obtained dividing the energy by the band gap of 3.6 eV and 'smeared' over the anodes according to the measured charge sharing and diffusion. The anode amplitude is calculated, taking local variations of the gain and losses due to diffusion and signal shaping ("ballistic deficit") into account. The amplitude is distributed over time bins according to radial diffusion and the PASA response. Electronics noise is added on top of the generated signal and the zero-suppression by the scanner is simulated. Known dead anodes are skipped in the digitization. Due to charge sharing between several anodes, the probability of a single anode hit is rather small. However, the presence of a dead anode leads to an enhanced probability to find a single anode hit on the adjacent anodes, due to the partial signal loss on the dead anode. Hence, comparison of the phi distributions of single-anode hits, as done in Fig. 5.1, provides an elegant check of the proper implementation of the dead anodes in the simulation. Each dead anode is accompanied by two spikes, representing the neighboring anodes to the left and right. The location of the spikes in the data (upper left panel) and MC (upper right panel) distributions exhibit excellent agreement. Likewise, the distributions of $\Delta\phi$ and $\Delta\theta$ between two hits on a SDD segment, on which the SDD segment quality cuts are applied, agree reasonably well, as is demonstrated in Fig. 5.1 for segments with two multi-anode hits.

The correlated cut on the SDD resummed amplitudes is the most powerful rejection cut. However, along with a strong background reduction, it also induces significant signal loss. Hence, an accurate description of the efficiency of this cut is crucial for the understanding of the total pair efficiency. However, the comparison between the MC generated SDD dE/dx distributions and data is not trivial. The SDD amplitudes display a strong Landau tail intrinsic to the physics of the energy deposit. The tail is enhanced by particles traversing the SDD detector in vicinity of the signal electron, producing a double dE/dx

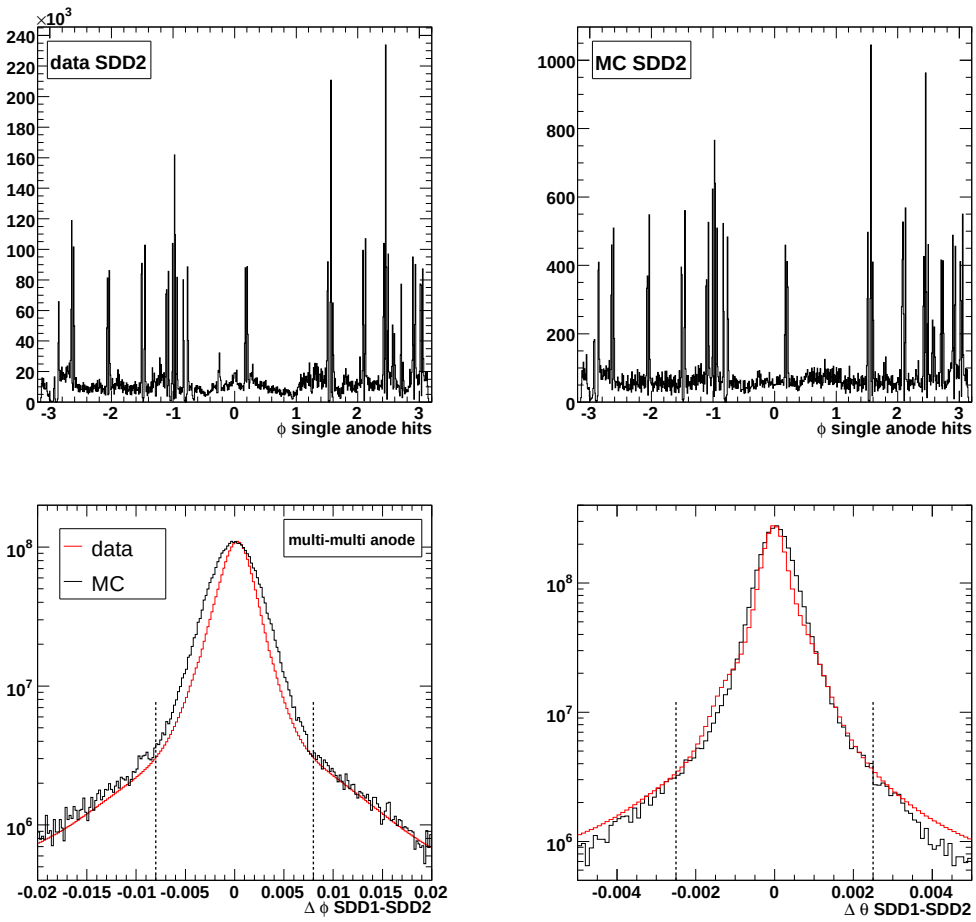

Figure 5.1: Simulation of the SDD detectors - geometrical properties. The upper plots show the measured and simulated ϕ distribution of single anode hits. The spikes represent the position of dead anodes, as explained in the text. The bottom panel presents the distributions of $\Delta\phi$ and $\Delta\theta$ between two hits on SDD segment for data and MC, arbitrarily normalized. The cut applied in the analysis is indicated by the vertical lines.

signal due to pick-up of the additional amplitude. This effect is observed in the resummed dE/dx as well as the SDD hit amplitude (due to limitations in two-track resolution). A naive selection of low-momentum electrons from the data will contain a strong contribution from conversion legs. These are produced in pairs with small opening angle and naturally display a strong double dE/dx peak not representative for electrons from open pairs (this is, of course, the very feature exploited for conversion rejection with the cut on the resummed amplitude). On the other hand, any measure taken to suppress the conversion contamination for a comparison between MC and data risks to suppress also the natural random pick-up of particles from the vicinity of the signal tracks.

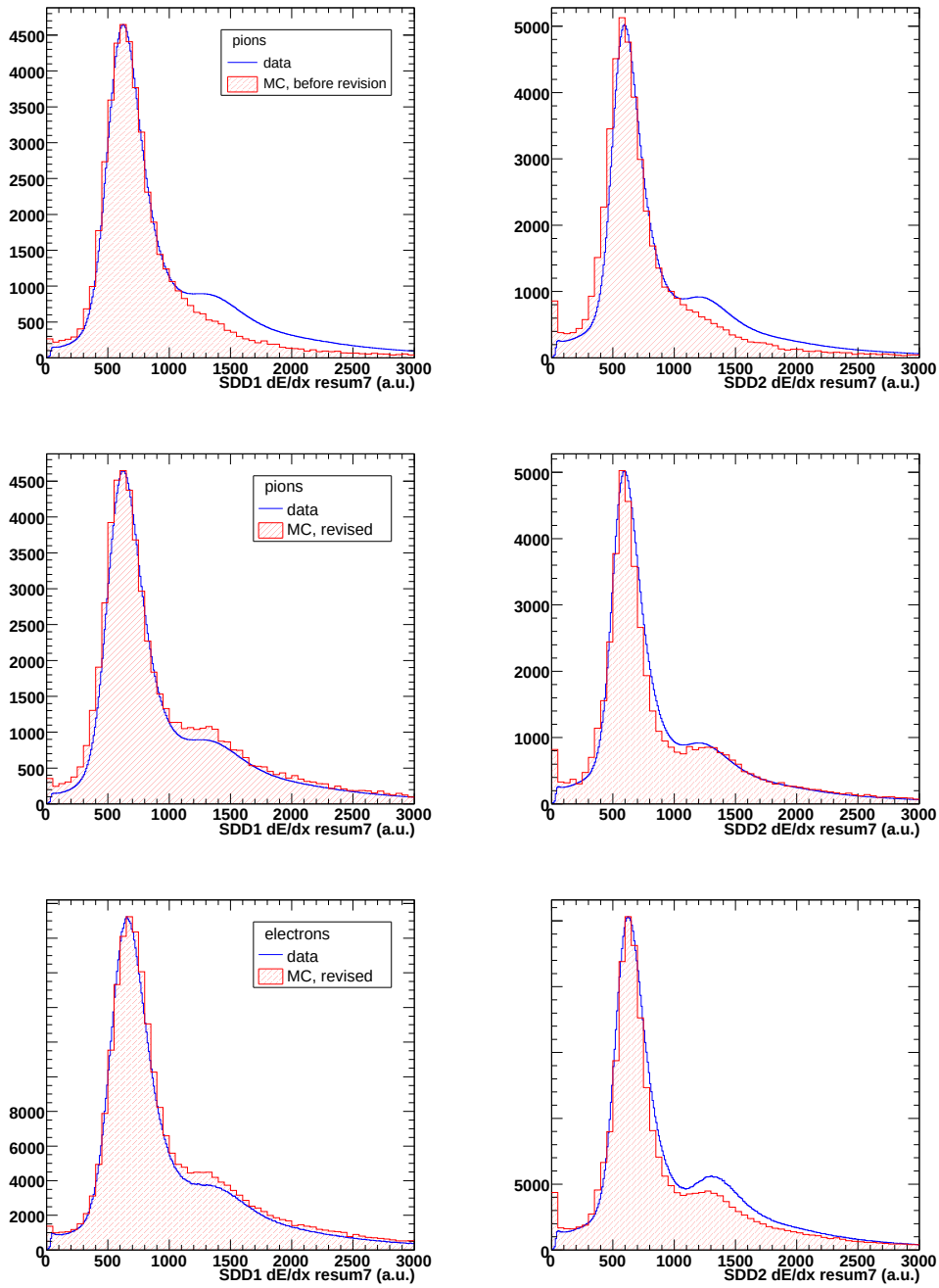

Figure 5.2: SDD resummed amplitude: comparison of data and MC generated distributions for SDD1 (left column) and SDD2 (right column). The upper panel presents the distributions, obtained for charged pions (both in MC and data), before revision of the simulation code. In the center panel, we show results from the corrected simulations. The plots in the bottom present the distributions from the revised MC for electrons.

To circumvent these difficulties, we chose a different approach: we compare the MC generated SDD dE/dx signal for `pions` to a pion reference sample from data. Indeed, it turned out that the MC simulations initially were not able to describe the distribution correctly, as is demonstrated in the upper panel of Fig. 5.2: the double dE/dx peak is significantly underestimated. The same discrepancy, observed before for electrons, had been attributed to the contribution of conversions. The pion data prove, however, that the pick-up contribution is very important, and was hitherto underestimated in the simulations. The center panel shows the same data compared to the generated distributions after revision of the MC code. The new overlay strategy implemented in the SDD simulations significantly improves the comparison between data and MC. In the bottom panel, we present the dE/dx distributions measured and generated for electrons. To allow for a comparison of the position of the maximum and the width of the single dE/dx peaks, we suppress the double dE/dx peak, applying a cut on dE/dx in SDD2 for plotting the dE/dx distribution in SDD1 and vice versa. Therefore the height of the double dE/dx peaks is somewhat arbitrary and the rather good agreement between simulations and data a coincidence. Only the position and width of the electron single dE/dx peak should be compared, and they are well reproduced by the simulations.

5.2 TPC

For the simulation of the TPC, only the position of the Geant hits is used to create the track. The number of primary electrons is determined independently, sampling a Poissonian distribution with mean determined according to [103] as function of the track momentum. Between two Geant hits, a straight track segment is constructed along which the primary ionization is uniformly distributed. Then, the position of the primaries is smeared, and the number of secondary electrons is generated according to a power-law distribution for δ-electrons. The ionization is propagated through the drift electric field, reading the position at the level of the readout pads as function of the initial position from a lookup table. Each ionization electron is assigned to an anode wire according to its z-position, and the induced charge on the readout pads is calculated. Then, the signal for each pad is distributed over time bins according to tabulated time distributions of the induced signal for different positions of the primary electron with respect to the anode. All signals for a given time bin and pad are summed up.

The geometrical properties of the simulated TPC tracks are confronted with the data in Fig. 5.3. In the upper panel we present the distribution of hits on tracks. Simulations and data agree well. We observe in the data a small excess of tracks with very few hits relative to the Overlay MC. It can be attributed to the edges of the TPC acceptance, as is demonstrated in the lower left panel, where the number of hits on track (position of the maximum, averaged over 3 histogram bins) is shown as function of the polar coordinate

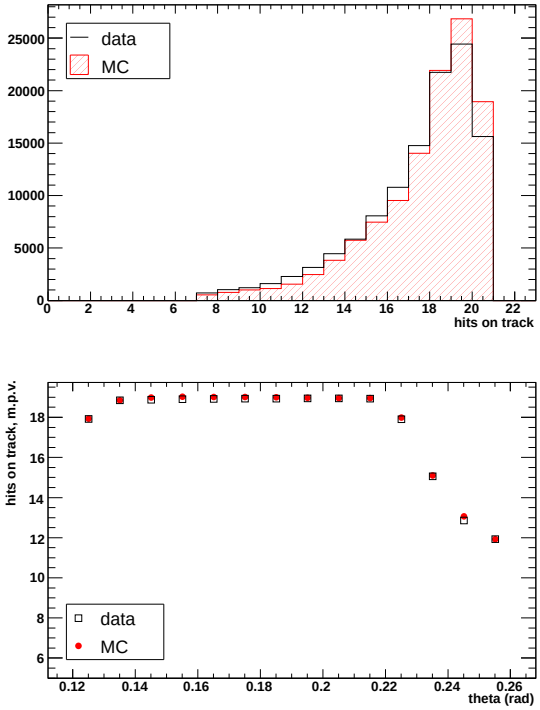

Figure 5.3: Number of TPC hits on track for data and simulations. Top left panel: integral distributions (random normalization). Bottom panels: number of hits (position of the maximum) as function of θ and ϕ.

θ of the track. Systematic deviations occur at very low and very high θ. However, within the single track acceptance for the electron analysis, $0.141 < \theta < 0.244$, the agreement is very satisfactory. Likewise, the ϕ distribution of the number of hits on track from the data, shown on the lower right, is well reproduced. The chamber structure, producing 'holes' of reduced efficiency at the boundaries, as well as the inefficient region at $\phi = -3$ are clearly visible in data and MC.

In Fig. 5.4, we compare the specific ionization dE/dx, for simulated electron tracks to the data. The electron content of the data track sample was enhanced requiring a high number of RICH hits on track. The natural pion contamination produces a second hump at low dE/dx. The position of the electron peak in the data is well described by

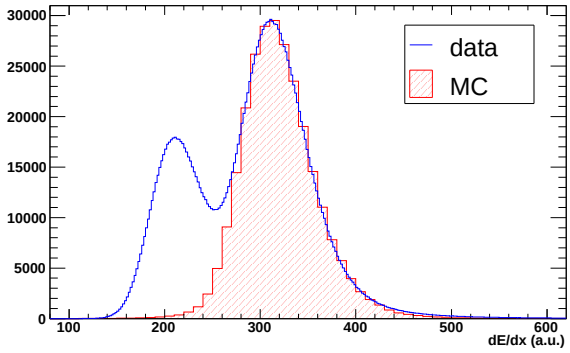

Figure 5.4: Comparison of TPC dE/dx for data and simulations. The pion contamination of the electron enhanced data sample introduces a peak at low dE/dx not present for the simulated electron tracks.

the simulations, as well as the high dE/dx flank of the distribution, indicating a good agreement of the simulated width.

5.3 TPC-SDD matching

In the data analysis we establish global tracks requiring good (2σ) matching between the TPC and SDD segment defining the electron track. For the simulated tracks, the matching quality is evaluated analogously to the data, as described in section 3.8.1. In Fig. 5.5, we show for a slice in θ the width σ from Gaussian fits to the matching distributions obtained for different momentum slices, along with the parametrization according to Eq. 3.2. Data and MC agree reasonably well. For consistency, the matching cuts applied on the MC tracks are evaluated from the observed distributions within the simulations.

We further include into the simulated matching efficiency the effects of 1.) non-Gaussian tails of the measured matching distributions and 2.) systematic deviations of the measured width of the data from the parametrization Eq. 3.2. The first effect reduces the matching efficiency with respect to the expected value (∼95% for a 2σ cut). The second effect leads to an enhancement of the efficiency at low momenta, since there the fitted parametrization tends to overpredict the observed width. Both effects are evaluated from the data, integrating in each θ and momentum slice the measured $\Delta\theta$ and $\Delta\phi$ distributions over the range given by the parametrization and comparing to the total integral. The deviations from the expected efficiency are tabulated and taken into account for the total reconstruction efficiency.

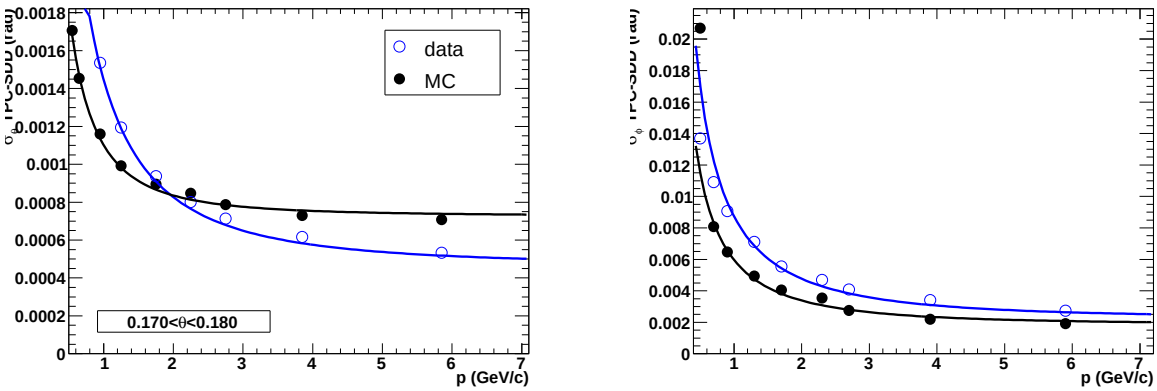

Figure 5.5: TPC-SDD matching versus momentum. The width of the matching distributions (projections along θ (left) and ϕ (right)), along with the parametrization, are compared to simulations.

5.4 RICH detectors

The Geant simulation of the RICH gives the position and energy of the photon hits in the UV detectors. The position of the hits is smeared to simulate the combined effects of chromatic aberration due to the energy dependence of the refractive index of the radiator gas, diffusion of the charge created in the conversion and amplification zone of the readout, mirror quality and position resolution of the readout. The subsequent amplification stages of the RICH readout spread the signal of the single photoelectron over 7×7 readout pads according to an inverse cosh function. Local gain variations and readout thresholds are applied, and the digitized signal is embedded into the data. We apply the hit clean-up procedure to account for possible signal losses on the hit level.

In the upper panel of Fig. 5.6, we confront simulations and data: shown is the distribution of the number of hits on ring. The data distribution is obtained from an electron sample after subtraction of the contamination from pions and other nonradiating particles.

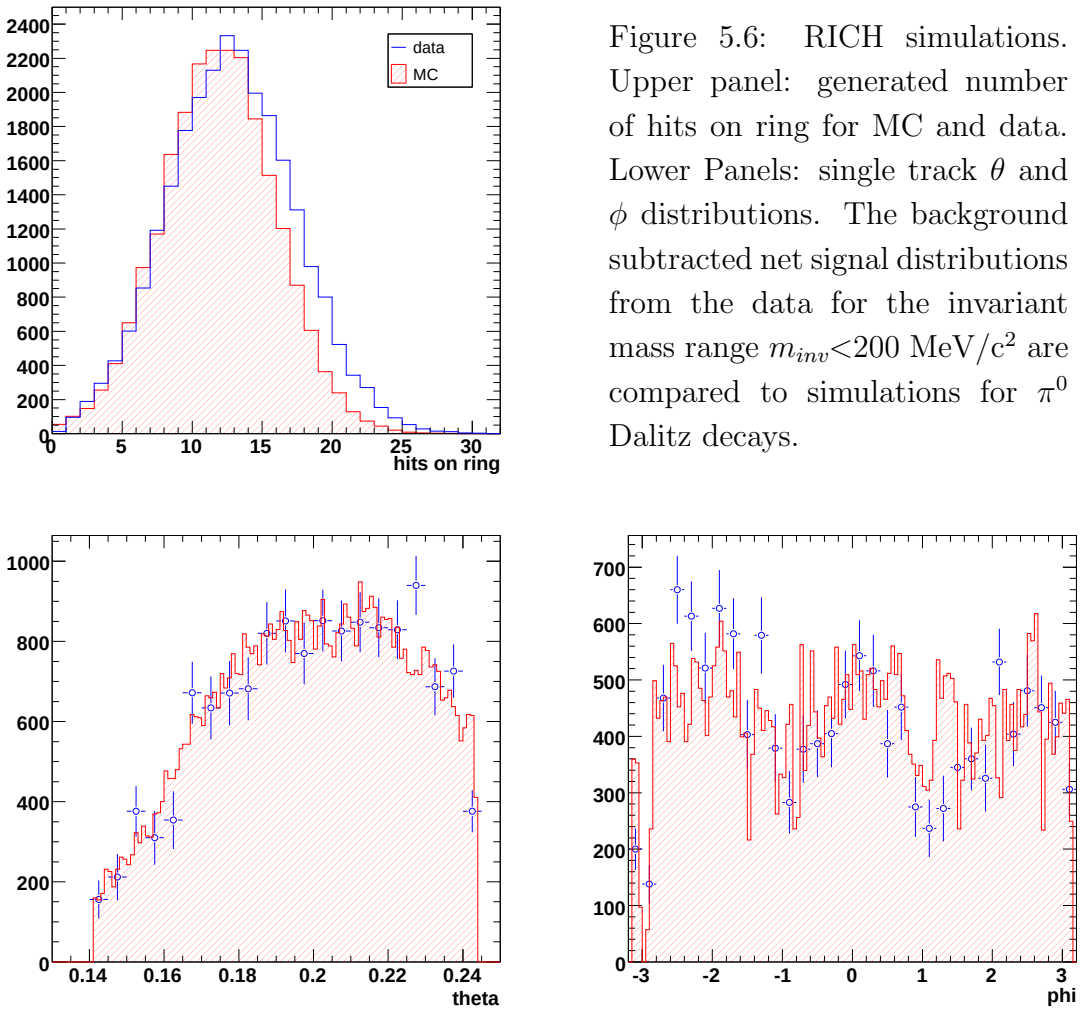

Figure 5.6: RICH simulations. Upper panel: generated number of hits on ring for MC and data. Lower Panels: single track θ and ϕ distributions. The background subtracted net signal distributions from the data for the invariant mass range m_{inv}<200 MeV/c^2 are compared to simulations for π^0 Dalitz decays.

Tracks were restricted to the fiducial acceptance and a momentum interval as described in section 3.7.3. The MC distribution is obtained for electrons from π^0 Dalitz decays, applying the same selection criteria. The tail towards low values of the number of hits is due to local inefficiencies, dead areas, of the RICH readout system. The effect was simulated extracting a map of the inefficient regions for each calibration unit and systematically discarding simulated hits found in such areas from the reconstruction. The agreement between data and simulations is reasonable: the measured and simulated distributions are similar in shape. The maxima roughly agree, however, the simulated distribution is shifted by about one RICH hit. To accommodate for this discepancy, we adjust the cut value applied to the simulated electron tracks accordingly to assure correct evaluation of the pair reconstruction efficiency.

Although the simulation is capable to reproduce reasonably well the RICH performance in terms of `average` quantities, it turns out that `local` effects, i.e. the efficiency as function of θ and ϕ are not well described. To remedy possible inaccuracies in the evaluation of the reconstruction efficiency, we chose to apply within the MC simulations a geometrical correction derived from the the measured RICH efficiency as function of θ and ϕ. A comparison of the resulting MC single track θ and ϕ distributions for electrons from Dalitz pairs and data (background subtracted single tracks from pairs with m_{inv}<200 MeV/c^2, opening angle >0.035 rad) is shown in the lower panels of Fig. 5.6. The distributions agree reasonably well.

5.5 Electron pair reconstruction efficiency

To allow for a quantitative comparison with the hadronic cocktail or theoretical calculations, the measured e^+e^- pair spectra have to be corrected for experimental pair efficiency. To cover a wide range in electron momenta, pair p_T and pair invariant mass, we present efficiency studies for four different sources of electron pairs: π^0, η, ρ, and ϕ. The decays were simulated with GENESIS, applying the standard cuts on acceptance, $2.1< \eta <2.65$, single track transverse momentum, p_T >200 MeV/c, and pair opening angle Θ_{ee}>0.035. The generated electron pairs are cycled through the data production chain and analyzed with the same software as used for the data. The pair efficiency is then simply evaluated as the ratio of reconstructed to generated pairs. In a similar fashion we can evaluate the single track efficiency, counting the number of reconstructed electron tracks and dividing by the number of input tracks. The θ and momentum distributions of the generated sources, before and after analysis cuts, are shown in Fig. 5.7.

An elegant check for correctness of the simulations is provided by the invariant mass region below 150 MeV/c^2 which is dominated by the π^0 and η Dalitz decays. Since the cross sections, p_T, and rapidity distributions of these decays, especially for the π^0, are measured with high accuracy [99], we can compare the measured number of pairs per event

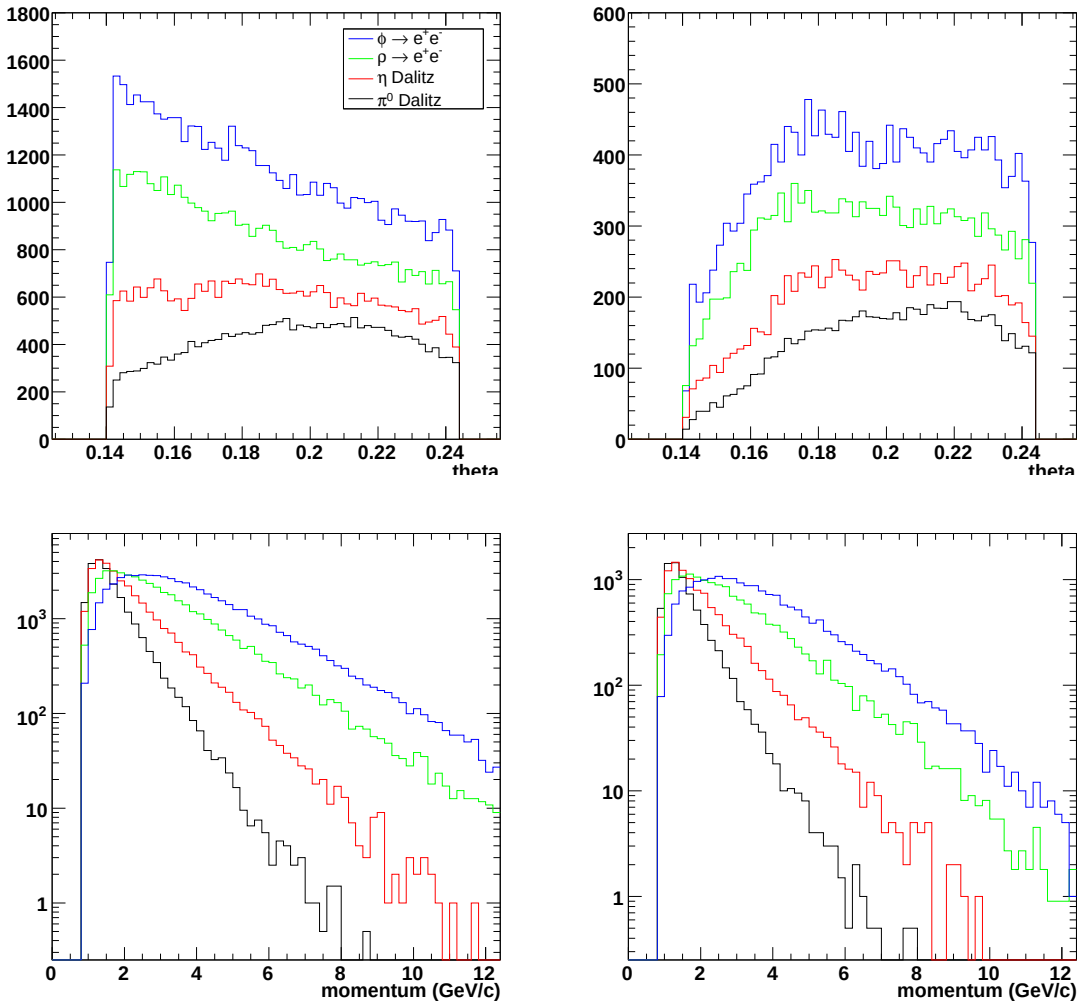

Figure 5.7: θ and momentum distributions of four generated decays (π^0, η, ρ, ϕ) before (left panel) and after (right panel) analysis cuts. The distributions before cuts are arbitrarily scaled.

in this mass region, normalized to N_{ch}, to the expected number to get a precise estimate of the expected pair efficiency[1]. In Fig. 5.8, upper panel, we compare the pair efficiency from data after each cut to the simulated efficiency for π^0 Dalitz pairs (the reconstruction efficiency for the η, which also contributes to the data, is very similar, since in the common invariant mass range the properties of the electron legs from both sources agree). The

[1]Indeed, in the past, sometimes the complementary approach was chosen to normalize the data to the cocktail, i.e. to scale the invariant mass spectrum to the expected cocktail yield in the Dalitz region. Note, that some theoretical calculations predict for heavy-ion collisions an excess of the yield of electron pairs over the cocktail even in this region of low invariant mass. However, the difference to the cocktail is too small to be resolved within the errors of our measurement and the systematic uncertainties

error on the data derived efficiency is dominated by `systematic` uncertainties. These are mainly the 12% relative systematic error of the N_{ch} measurement and an error of 8% on the expected cocktail yield [32]. The statistical error on the reconstructed electron pair signal after subtraction of the combinatorial background is evaluated according to Eq. 3.5. In the low invariant mass region the relative statistical error is below 5%. Simulated and expected pair efficiencies agree well. In particular the steps, the relative reduction for the sequence of cuts, are nicely described.

In the bottom panels we show pair efficiencies, after all rejection cuts, as function of the RICH cut. To check for possible systematic effects, the comparison is carried out for two different approaches: constant and a θ dependant RICH cut. In the latter case, the required number of RICH hits is adjusted for low θ, to compensate for losses outside the

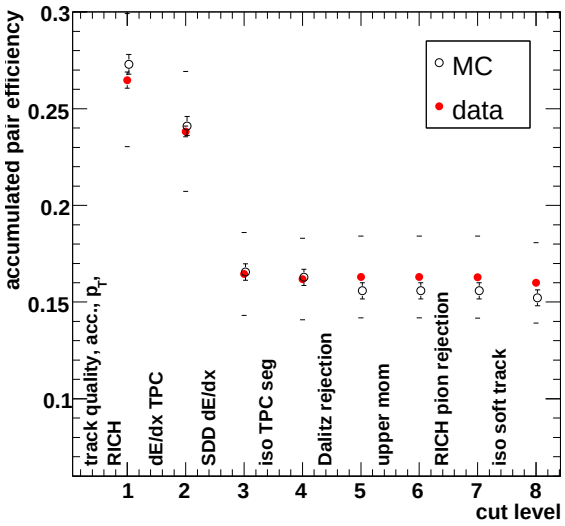

Figure 5.8: Pair efficiency from data (Dalitz pairs) and simulations (π^0 Dalitz). Upper panel: efficiency after each cut in the sequence of the analysis. Bottom row: pair efficiencies after all analysis cuts for different values of the RICH cut on hits on ring, for a θ dependant (left panel) and constant cut (right panel).

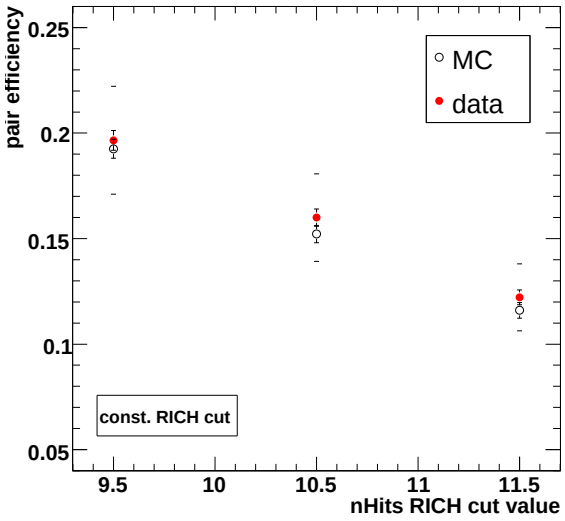

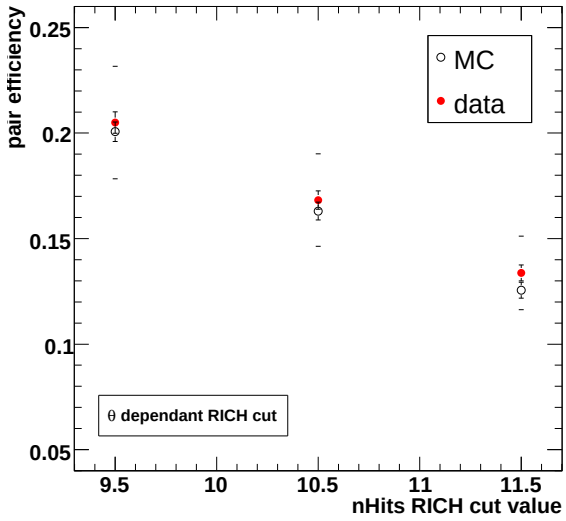

RICH fiducial acceptance. In the comparison, the cut on the number of hits is varied about the nominal value of 10.5 hits (for the θ dependant cut, this value refers to the cut inside the fiducial acceptance). The constant cut induces, relative to the θ dependant cut, a small signal loss well described by the simulations. The pair efficiency from the data is well reproduced by the MC over a wide range.

For a pair-by-pair efficiency correction of the spectra, we have to define a set of variables on which the single-track efficiency exhibits the same functional dependence for all sources. These variables are identified to be the polar angle θ and the event multiplicity. As shown in the left panel of Fig. 5.9, the efficiency plotted as function of θ, averaged over all event multiplicities, agrees very well for all four sources. The total number of electron tracks generated for this study exceeds $1.5{\cdot}10^6$. We observe a flat dependence for higher θ and a drop approaching midrapidity, due to the reduced RICH efficiency for low θ and the impact of the increasing multiplicity and detector occupancy on the TPC tracking efficiency as well as the efficiency of the SDD resummation. The multiplicity dependence is investigated more closely in the right, where the integral single track efficiency for all sources is plotted as function of the calibrated centrality for different slices in θ. In each slice, a first order polynomial is fitted. The overall multiplicity dependence is rather small: the efficiency rises as function of centrality (small centrality = large multiplicity), but the differences between the first and the last centrality bin are only of the order of a percent.

Furthermore, a small `explicit` momentum dependence of the efficiency is introduced by the TPC dE/dx electron identification cut, rising as function of momentum[2]. This is illustrated in the bottom panel of Fig. 5.9.

The efficiency correction to the pair spectra in invariant mass and p_T is applied on a pair-by-pair basis. For each track of the pair, the reconstruction efficiency $\epsilon(\theta, m)$ is calculated as function of θ and event centrality c. First, the linear fits are used to calculate the efficiency for the given centrality for the two closest θ nodes:

$$\begin{aligned} \epsilon(\theta_1, cent_1) &= P_0(\theta_1) + P_1(\theta_1) \cdot cent_1 \\ \epsilon(\theta_2, cent_2) &= P_0(\theta_2) + P_1(\theta_2) \cdot cent_2 \end{aligned}$$

The momentum dependence is incorporated via linear fits of the relative deviation of the efficiency from the mean efficiency in each θ slice, yielding a correction factor $corr(\theta, mom)$:

$$corr(\theta, mom) = corr_0(\theta) + corr_1(\theta) \cdot mom$$

$$\begin{aligned} \epsilon_1 &= \epsilon(\theta_1, cent_1, mom_1) = \epsilon(\theta_1, cent_1) \cdot corr(\theta_1, mom_1) \\ \epsilon_2 &= \epsilon(\theta_2, cent_2, mom_2) = \epsilon(\theta_2, cent_2) \cdot corr(\theta_2, mom_2) \end{aligned}$$

[2]Since, on average, towards midrapidity the momentum of the legs from open pairs tends to increase, any variation of the efficiency with θ introduces an additional implicit momentum dependence.

Finally, we interpolate in theta:

$$\epsilon_{track}(\theta, m) = \frac{\theta_2\epsilon_1 - \theta_1\epsilon_2}{\theta_2 - \theta_1} + \frac{(\epsilon_2 - \epsilon_1)\cdot\theta}{\theta_2 - \theta_1}$$

For each pair, a weight is determined as the inverse product of the efficiencies for both tracks:

$$w = \frac{1}{\epsilon_{track1}\cdot\epsilon_{track2}}$$

The histogram, e.g. of invariant mass or pair p_T, is filled with this weight. The procedure is applied to the (same and mixed event) like-sign as well as the unlike-sign histograms.

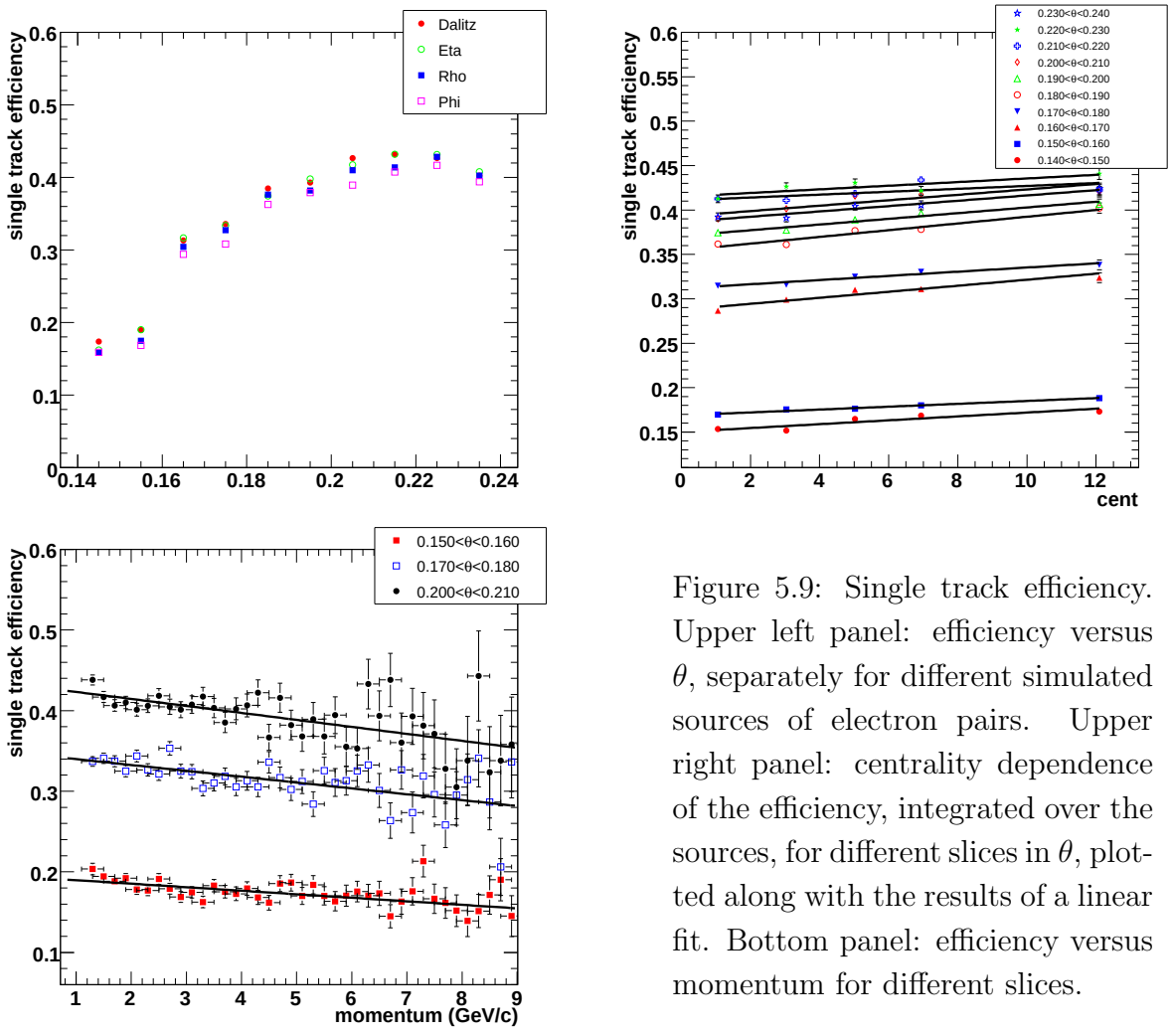

Figure 5.9: Single track efficiency. Upper left panel: efficiency versus θ, separately for different simulated sources of electron pairs. Upper right panel: centrality dependence of the efficiency, integrated over the sources, for different slices in θ, plotted along with the results of a linear fit. Bottom panel: efficiency versus momentum for different slices.

5.6 Combinatorial background composition

Besides the evaluation of the electron pair efficiency, the detector simulation allows to estimate the background rejection achieved with the spectrometer. This permits to explore and understand quantitatively the origin of the combinatorial background. For this purpose, three different sources of electrons (real and fake) were generated:

- π^0: conversion electrons mainly stem from photons from neutral pion decays (branching ratio $BR_{\pi^0\to\gamma\gamma} = 0.988$ [6]). These dominate by far the direct thermal radiation from the fireball.
- π^0 Dalitz decays are the most abundant source of electron pairs. If a single electron is not reconstructed, either due to limitations in acceptance or detection efficiency, the other leg contributes to the combinatorial background.
- charged π: misidentified pions are the most important hadronic source of potential background tracks since 1.) they are the most abundant hadron species and 2.) their low mass results in a strong rise of the energy deposit in the TPC at moderate momenta, resulting in a relatively high probability to survive the dE/dx cut and hence a strong pion contribution to fake electrons.

The electron pairs from Dalitz decays were simulated with GENESIS, without any cut on the pair opening angle and electron momentum. A very wide single leg acceptance of $1.60< \eta <3.91$ was chosen to fully account for pairs with partial acceptance coverage. The charged and neutral pions were generated with Geant, using rapidity and p_T input distributions as implemented in GENESIS.

For comparison of the different contributions, we scale the reconstruction probabilities for tracks from each each source with the production rate relative to the number of charged particles. The number of conversion electrons per charged particle is:

$$\begin{aligned}\frac{N_e}{N_{ch}}^{conversions} &= N_{\pi^0}/N_{ch} \cdot BR_{\pi^0\to\gamma\gamma} \cdot \frac{N_\gamma}{N_{\pi^0}} \cdot \frac{7}{9}\frac{X}{X_0} \cdot p(e|e^+e^-) \\ &= 0.43 \cdot 0.988 \cdot 2 \cdot 7/9 \cdot 0.0075 \cdot p(e|e^+e^-)\end{aligned}$$

where we have used $\frac{X}{X_0} = 0.75\%$ for target conversions (single target disk), which represent the most relevant contribution, since practically all other conversions are removed by the matching and rejection cuts. The term $p(e|e^+e_-)$ denotes the probability to accept a single electron (or positron) leg from a conversion as a 'good' electron which enters the pairing. It includes the acceptance and single electron p_T cuts as well as the particle identification and also the probability to survive the rejection cuts, evaluated in the simulations.

For electron pairs from π^0 Dalitz decays, we have

$$\begin{aligned}\frac{N_e}{N_{ch}}^{Dalitz} &= N_{\pi^0}/N_{ch} \cdot BR_{\pi^0 \to e^+e^-\gamma} \cdot \frac{N_{e^+e^-}}{N_{\pi^0}} \cdot p(e|e^+e^-\gamma) \\ &= 0.43 \cdot 0.0112 \cdot 1.037 \cdot p(e|e^+e^-\gamma)\end{aligned}$$

The correction factor $\frac{N_{e^+e^-}}{N_{\pi^0}}$ accounts for the decays of heavier mesons, evaluated with the values given in table 4.1[3]. The fake electron contribution is simply given by the probability to misidentify a pion above the minimum p_T emitted into the acceptance as an electron:

$$\frac{N_e}{N_{ch}}^{fake} = p(e|\pi)$$

The result of the background simulations is presented in Fig. 5.10. The number of reconstructed electrons and positrons per event, normalized to the charged particle multiplicity, is shown for each source for the sequence of cuts applied in the electron analysis. Conversions after the SDD detectors, especially from Rich-2 mirror, are very effectively removed by the SDD-TPC matching and the RICH condition. The plot nicely demonstrates the suppression of the remaining target conversions by the rejection cuts. The fake electron component, labelled 'charged pions', is suppressed by the RICH and TPC electron identification by more than 4 orders of magnitude, in good agreement with our estimate in section 3.8.3. The most dominant contribution to the combinatorial background stems from π^0 Dalitz decays. To illustrate the origin of the background, we distinguish 3 cases: completely reconstructed pairs, single electrons after loss of a leg due to the limited detector acceptance (which we define ad hoc via the interval $0.120<\theta<0.260$ in polar angle) and after loss due to reconstruction efficiency. Since the detector acceptance is not sharply defined in terms of θ, this distinction bears some arbitrariness. Still, the conclusion is remarkable and does not rely on the technical details of separating the individual contributions: the combinatorial background is mostly due to limited track reconstruction capabilities at very low momenta. The majority of background tracks stem from Dalitz decays with one reconstructed leg with sufficiently high momentum to survive the p_T cut and a non reconstructed low-momentum leg. The low-momentum tracking slightly improves the situation: the isolation cut against soft tracks somewhat reduces the Dalitz background. The background reduction is only moderate, since too strong cutting would result in unacceptable loss of signal efficiency. Furthermore, the plot shows the contribution of fully reconstructed pairs. They contain also the electrons from the pairs plotted in the invariant mass spectrum, with a pair opening angle exceeding 0.035 rad. It is important to note that the number of electrons from fully and from partially reconstructed pairs, here plotted separately, are closely related: the reduction of electrons from

[3]We neglect here the enhancement of the open pair yield with respect to the cocktail, which is measured with large uncertainties and induces only a very small modification of the correction factor.

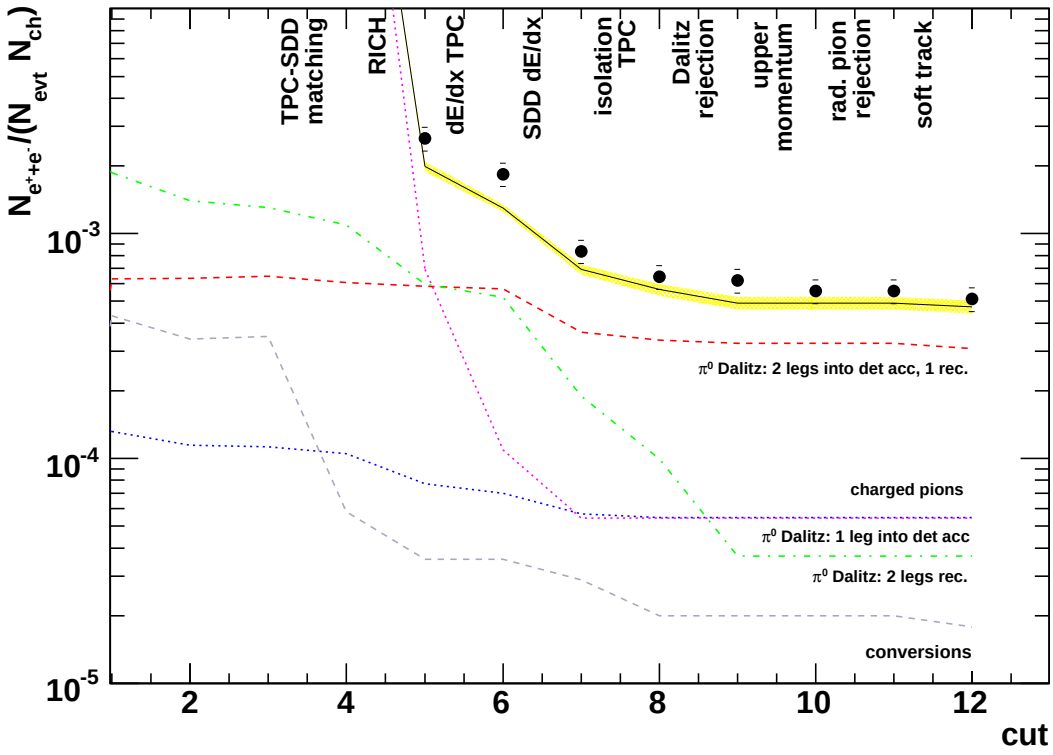

Figure 5.10: Number of reconstructed electron tracks per event above p_T=200 MeV/c into the electron acceptance 2.1< η <2.65, normalized to N_{ch}. The measurement is compared to a simulation of the contributions from conversions, Dalitz decays and misidentified pions. The error band indicates the statistical error on the simulations. For the data, we indicate the systematic error introduced by normalizing to N_{ch}.

fully reconstructed pairs by a given cut will increase, 'feed down' to, the number of single electrons.

The sum of all sources is compared to the measured number of electron tracks for the different cuts. The agreement between data and simulations is good. The statistical error on the simulations, indicated by the shaded band, is $\lesssim 7\%$ (relative error). It is mostly due to the statistics limitations to the accuracy with which the reconstruction efficiency of charged pions is determined. For the data points, the systematic error due to the normalization to N_{ch} is indicated.

6 Results

In this chapter we present the measured invariant mass and transverse momentum spectra and compare them to theoretical predictions. The comparison to previous CERES results yields an estimate of the systematic error on the measurement.

6.1 Data normalization

To allow for a meaningful comparison of the spectra to other experimental results and theoretical predictions, the reconstructed electron pair yield has to be divided by the number of Pb-Au collisions. Furthermore, in the absence of any collective effects induced by the medium produced in the heavy-ion collision, the pair yield is expected to scale linearly with the charged particle multiplicity. Hence, the absolutely normalized spectra are obtained from

$$\frac{1}{\langle N_{ch}\rangle}\frac{dN_{ee}}{dm_{ee}} = \frac{(dN_{ee}/dm_{ee})^{effCorr}}{\Delta\eta \cdot dN_{ch}/d\eta \cdot N_{event}}$$

where $(dN_{ee}/dm_{ee})^{effCorr}$ denotes the invariant mass spectrum after the pair-by-pair efficiency correction described in section 5.5, $dN_{ch}/d\eta$ the charged particle pseudorapidity density, $\Delta\eta = 0.55$ the single track acceptance and $N_{event} \approx 23{\cdot}10^6$ represents the number of measured events. Normalization of the transverse momentum spectra proceeds equivalently.

6.2 Invariant mass spectra

In Fig. 6.1, we present the absolutely normalized invariant mass spectrum. The single track acceptance is $2.1 < \eta < 2.65$, a transverse momentum cut $p_T > 200$ MeV/c^2 and a pair opening angle cut $\Theta_{ee} > 0.035$ are applied. The number of pairs reconstructed from $23.1{\cdot}10^6$ analyzed events in the low-mass region $m_{inv} < 0.2$ GeV/c^2 amounts to 5024±144, with a background over signal ratio of 1.56. In the region 0.2 GeV/c^2 $< m_{inv} < 2.0$ GeV/c^2 we obtain a signal of 1759±285 pairs, with a ratio of background over signal of 22.6 (Eq. 3.5).

In Fig. 6.1, the data are compared to the GENESIS hadronic cocktail described in chapter 4. In the region of low invariant masses $m_{inv} < 0.2$ GeV/c^2, dominated by the π^0

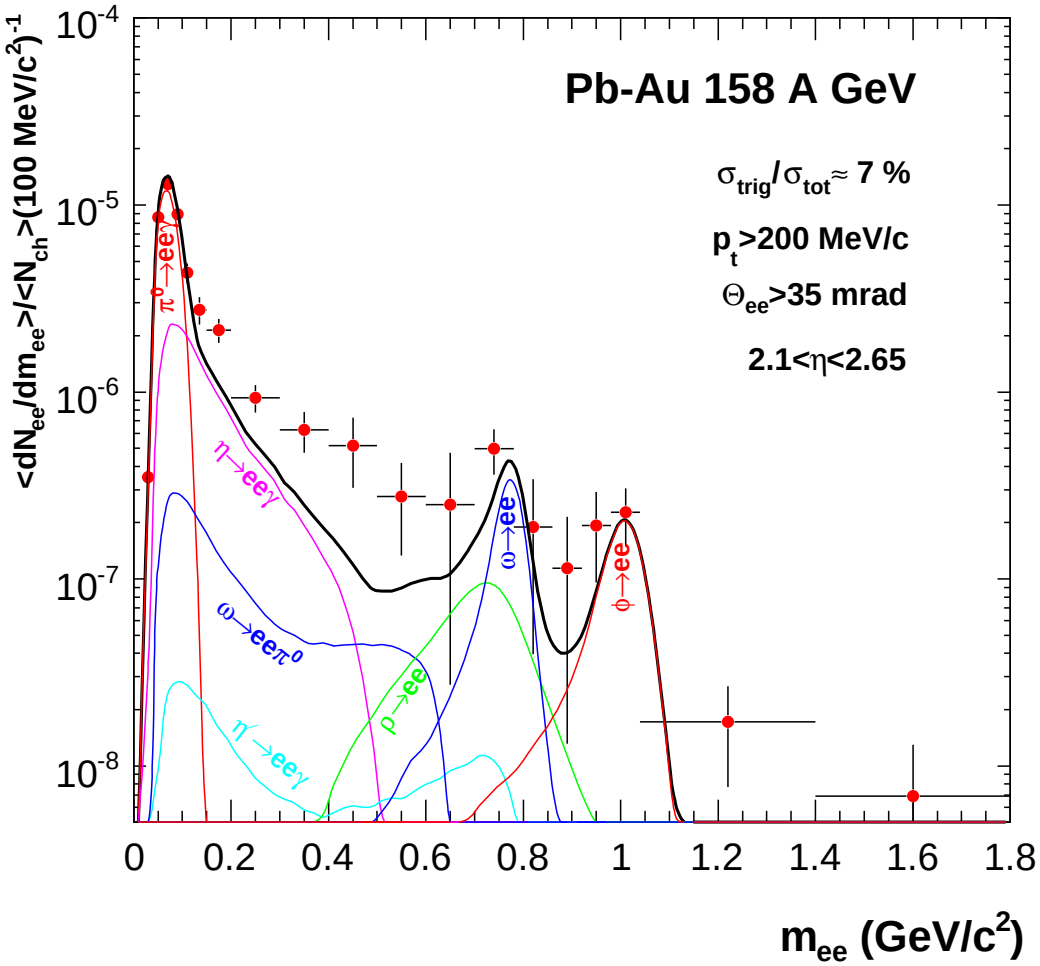

Figure 6.1: Inclusive e^+e^- invariant mass spectrum for Pb-Au collisions at 158 GeV/c per nucleon. The spectrum is corrected for pair reconstruction efficiency and normalized to N_{ch}. The black curve represents the expected yield from the hadronic cocktail. The individual contributions are indicated by colored lines.

and η Dalitz decays, the cocktail describes the data very well: the normalized integrated signal yield of $8.9{\cdot}10^{-6}$ exceeds the cocktail yield by 5% and hence agrees with the data within the statistical error of 3 %. For higher masses, an excess over the cocktail develops: in the mass region $0.2 < m_{inv} < 0.6$ GeV/c^2, the integrated normalized pair yield of $2.4{\cdot}10^{-6}$ exceeds the cocktail by a factor 2.27 ± 0.31. The good resolution obtained with the TPC allows to resolve the peaks of the ω and ϕ meson. Also for the mass region of the ρ/ω and between the ω and the ϕ, we observe the excess of the data over the expectations from hadronic decays: the integrated yield for $0.2 < m_{inv} < 1.1$ GeV/c^2 of $3.6{\cdot}10^{-6}$ lies a factor $2.05{\pm}0.23$ above the calculations. For masses of $\sim$1 GeV/c^2 and above, good agreement between the data and the hadronic cocktail is observed, indicating consistency to the measurement of the ϕ meson yield published in [85]. Systematic uncertainties are

discussed in Section 6.4.

The good tracking capabilities of the CERES TPC allow reconstruction of electron tracks with low transverse momenta down to 100 MeV/c. This offers the possibility to examine the invariant mass spectrum with a lower single track cut $p_T > 100$ MeV/c. However, the lower p_T cut is a strong tool for background rejection, and decreasing the cut value we unavoidably get a stronger background contribution. The invariant mass spectrum with $p_T > 100$ MeV/c is shown in Fig. 6.2. The spectrum is efficiency corrected and absolutely normalized. The net signal increases drastically compared to the results for the higher p_T cut: 29537±447 and 3216±592 for $m_{inv} < 0.2$ GeV/c^2 and $m_{inv} > 0.2$ GeV/c^2, respectively. As expected, the ratio of background to signal deteriorates: B/S is 2.89 and 54.0 in the respective mass regions. The observed excess relative to the hadronic cocktail for $m_{inv} > 0.2$ GeV/c^2 is 2.06 ± 0.26, practically equal to the value observed with the $p_T < 200$ MeV/c cut.

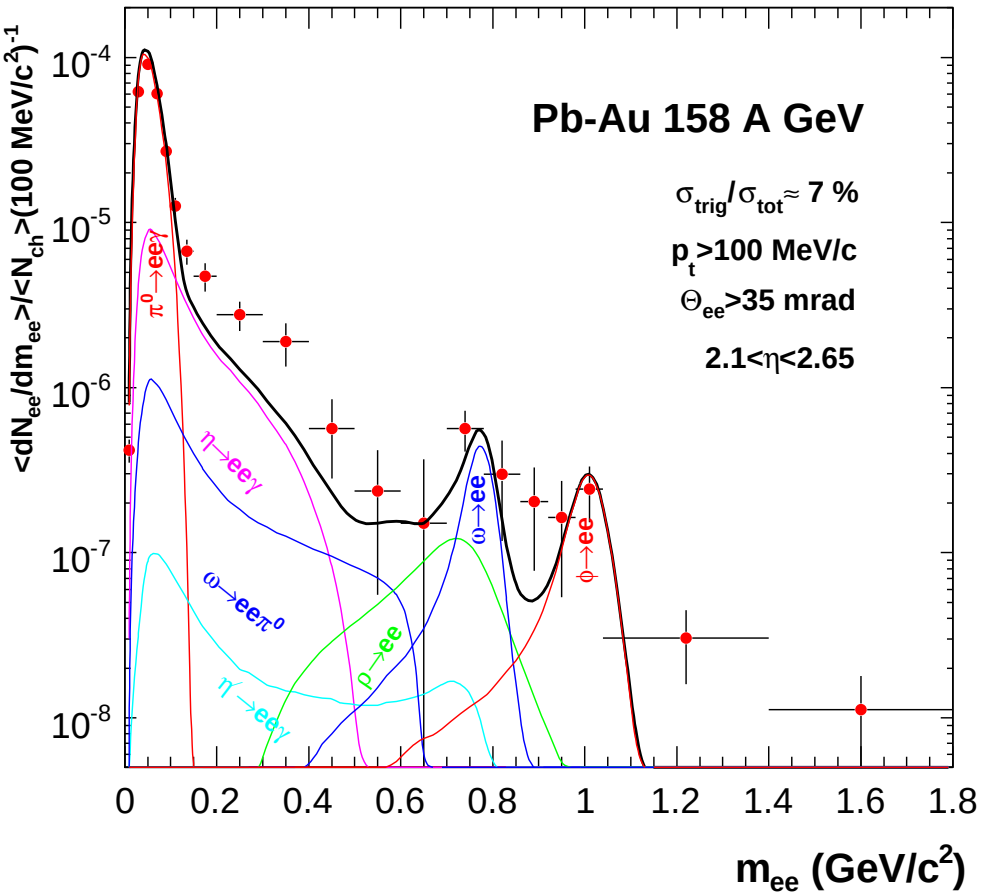

Figure 6.2: Inclusive e^+e^- invariant mass spectrum with a single track p_T cut of 100 MeV/c. The spectrum is absolutely normalized. The black curve represents the expected yield from the hadronic cocktail. The individual contributions are indicated by colored lines.

6.3 Pair transverse momentum spectra

The pair transverse momentum spectra are presented in Fig. 6.3, for different windows of invariant mass: $m_{inv} < 0.2$ GeV/c^2, 0.2 GeV/c^2 $< m_{inv} < 0.7$ GeV/c^2 and 0.7 GeV/c^2 $< m_{inv} < 1.5$ GeV/c^2. The spectra are efficiency corrected and absolutely normalized.

We compare the spectra are to the expectation from the hadronic cocktail. This allows to examine the transverse momentum dependence of the enhancement observed in the invariant mass spectra. In the Dalitz region, $m_{inv} < 0.2$ GeV/c^2, the spectra agree very well with the cocktail for low pair $p_T \lesssim 1$ GeV/c. The steep drop of the pair p_T spectra at about 400 MeV/c^2 is due to the cut on single track transverse momentum: the condition $p_T > 200$ MeV/c removes pairs with small opening angles and transverse momenta below twice the single track cut value. For larger p_T, we observe a gradually developing enhancement. The effect proceeds to the higher invariant mass window from 0.2 GeV/c to 0.7 GeV/c. The excess over the cocktail is most pronounced for the low pair transverse momenta. In the third invariant mass bin above 0.7 GeV/c, the enhancement still remains, although somewhat lower in magnitude than in the middle mass region. It corresponds to the excess observed in the invariant mass interval between the ω and the ϕ mesons.

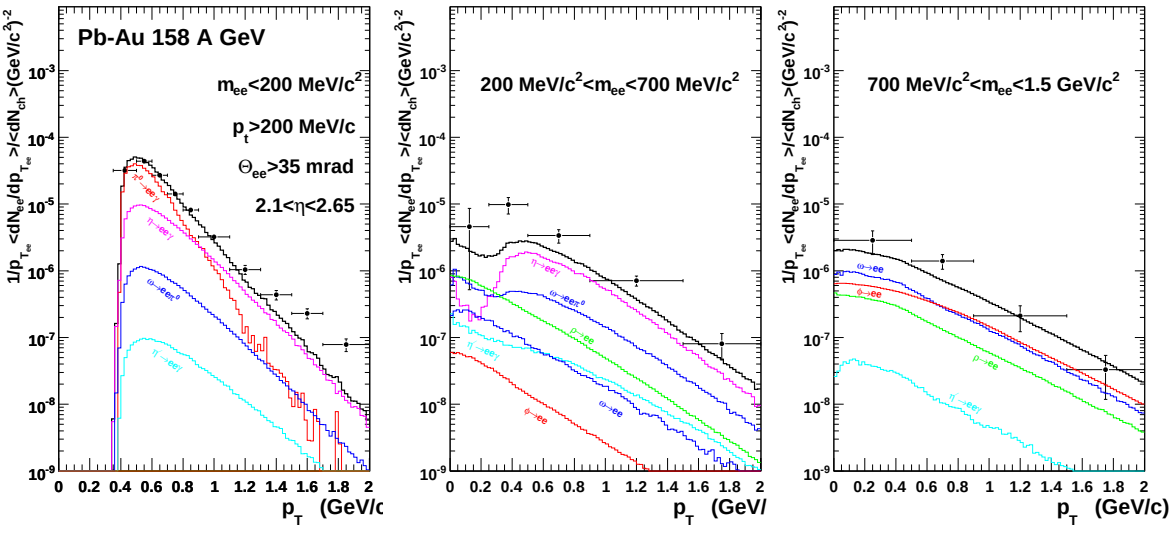

Figure 6.3: Pair transverse momentum spectra, corrected for reconstruction efficiency and normalized to N_{ch}, for different regions of invariant mass. The black curve represents the expected yield from the hadronic cocktail.

6.4 Systematic effects

Comparison of our results to the previous analyses of the same data set by A. Cherlin [54] and S. Yurevich [55, 104] indicates the important role of systematic effects. An overview is given in Table 6.1. We present the uncorrected pair signal along with the ratio of background over signal in the Dalitz region $m_{inv} < 0.2$ GeV/c^2 and for open pairs with 0.2 GeV/c^2 $< m_{inv} < 1.1$ GeV/c^2 as well as the enhancement factor of the normalized pair yield over the expectation from the hadronic cocktail. The ratio of background to signal in the open pair region is very similar in all three analyses. For low masses, we obtain a somewhat better value than in the previous works. The large difference in the raw Dalitz signal reconstructed by Cherlin compared to the other two analyses is due to the smaller number of events analyzed. The difference in the the number of Dalitz pairs observed between Yurevich and this analysis indicates the different pair reconstruction efficiencies. The relative differences observed in the number of open pairs are stronger than for the low-mass region, indicating a variation of the pair efficiency with invariant mass. To avoid the trivial effects of such variations of the reconstruction efficiency, we compare the different results in terms of the efficiency corrected normalized yield, or, equivalently, the enhancement factor of the yield over the cocktail. Within the statistical uncertainty, we find good agreement between the numbers presented by Yurevich and our results ('touching error bars'). The enhancement factor found by Cherlin is statistically barely consistent with our analysis: the difference is 2σ of the geometrical sum of the statistical errors of each analysis.

The question arises whether there might be a systematic discrepancy due to the different analysis strategy pursued in this work compared to the works be Cherlin and Yurevich. The most prominent difference between the present work and all previous analyses is the new RICH ring reconstruction employed. Therefore we shall compare in the following the

work	Dalitz pairs	S/B	open pairs	S/B	enhancement over Cocktail
A.Cherlin	3471±126	1.79	1747±258	18.6	2.9 ± 0.32[stat] ± 0.44 [syst]
S. Yurevich	6114±176	2.00	3115±376	22.0	2.61 ± 0.22[stat] ± 0.43 [syst]
O. Busch	5024±144	1.56	1759±285	22.6	2.05 ± 0.23[stat] ± 0.41 [syst]

Table 6.1: Results from different analyses of the 2000 data set. The electron pair yield, the ratio of background over signal for the Dalitz region ($m_{inv} < 0.2$ GeV/c^2) and for open pairs with $m_{inv} > 0.2$ GeV/c^2 as well as the enhancement factor of the normalized open pair yield over the expectation from the hadronic cocktail (0.2 GeV/c^2 $< m_{inv} <$ 1.1 GeV/c^2) are indicated. We compare our results to the results obtained by A. Cherlin [54] and S. Yurevich [55, 105].

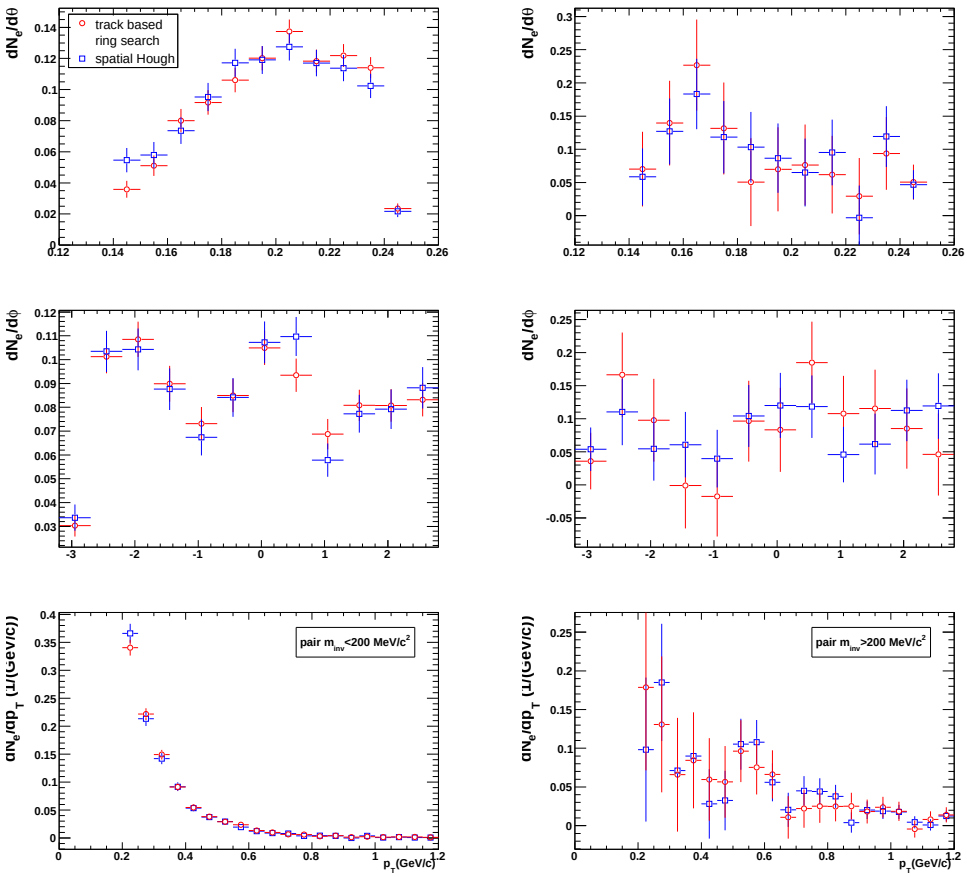

Figure 6.4: Background subtracted single track θ, ϕ and transverse momentum distributions. The distributions obtained for legs from Dalitz (left column) and high-mass pairs (right column) with the spatial Hough and the track based ring reconstruction are compared (distributions arbitrarily normalized).

two methods, the traditional spatial Hough algorithm and the track-based ring search, in terms of the properties of the reconstructed single electron tracks. In this context, one remark is at order: different reconstruction algorithms `can` be expected to produce different distributions. A correct implementation of the detector simulations will reproduce these differences and the efficiency correction to the data should account properly for the characteristics of the employed method. Therefore, this comparison should be understood as a check for any unexpected deficiency, and the aim is to rule out any spurious effect that might be the origin of the observed difference between the analyses.

In Fig. 6.4, we present the single track signal distributions of the polar angle θ, the azimuthal angle ϕ and the single track transverse momentum p_T, separately for the pair invariant mass regions $m_{inv} < 0.2$ GeV/c^2 and $m_{inv} > 0.2$ GeV/c^2. By construction, the combined distributions for the positive and negative legs of each pair represent twice the pair signal in the respective invariant mass region. To eliminate the trivial effect of

the different reconstruction efficiencies, the distributions are scaled to represent the same area. In the θ and p_T distributions, the single track acceptance and p_T cuts are manifest. Comparing the distributions obtained for Dalitz pairs, in the left column, we find very good agreement, especially for the ϕ and p_T distributions. For the lowest θ values, outside the RICH fiducial region, slightly less tracks are reconstructed with the track based ring search compared to the spatial Hough algorithm. This is understood as an effect of the different ring quality cuts: for the spatial Hough reconstruction, the cut on the Hough amplitude is lowered gradually towards low θ to preserve electron reconstruction efficiency, whereas in case of the based ring search the cut on the number of hits is kept at a constant level to preserve pion rejection power. We remind that the θ distribution from data is well described by the detector simulations, as is demonstrated in Fig. 5.6. For the tracks from open pairs, the comparison is very difficult due to the large statistical error reflecting the unfavorable background to signal ratio in this mass region. Within the errors, the distributions agree.

Since we can not detect any unexpected difference between the traditional and the new RICH ring reconstruction, we investigate the effect of a systematic variation of the analysis cuts. This includes the SDD-TPC matching strategy, the quality cuts to accept TPC

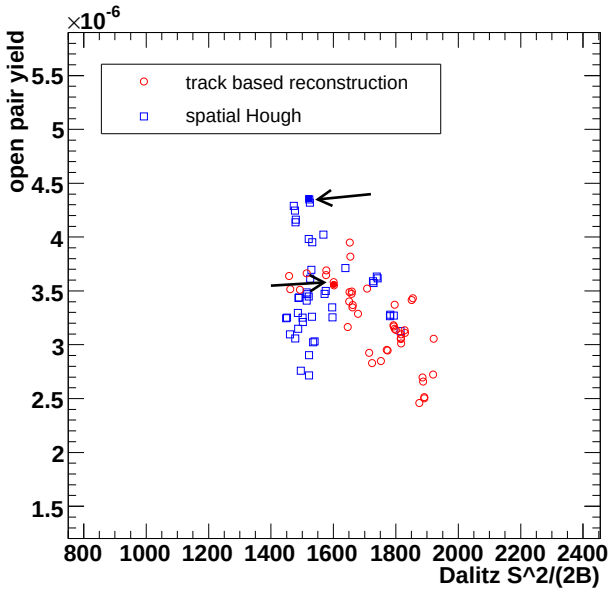

Figure 6.5: Open pair yield for pairs with masses $m_{inv} > 0.2$ GeV/c^2 versus Dalitz effective signal (ratio of squared signal over twice the background in the invariant mass region $m_{inv} < 0.2$ GeV/c^2) for different analysis cuts. Results from the spatial Hough and track based ring reconstruction are compared. The full symbols, indicated by the arrows, correspond to the invariant mass spectra Fig. 6.1 and Fig. 6.6

.

segments for electron tracks, the TPC electron identification via the specific ionization dE/dx, the RICH electron identification, the conversion rejection with the SDD detector and the isolation cut in the TPC. Along with the variation of the cuts, we evaluate the pair reconstruction efficiency accordingly. In Fig. 6.5, we present a scatter plot of the normalized open pair yield versus effective Dalitz signal (ratio $S^2/(2B)$) obtained for the different cut settings, separately for the track based RICH reconstruction and the spatial Hough method. For both methods we observe a comparable scatter of the points. On average, the yield obtained with the new method appears to be slightly lower compared to the traditional ring search, however, the difference is small compared to the observed range of the variations. The invariant mass spectrum presented in Fig. 6.1 corresponds to a point in the center of the scatter plot, indicated by the full circle in Fig. 6.5. To prove the consistency of our analysis strategy with the previous analyses of the 2000 data, we compare in Fig. 6.6 the invariant mass spectrum corresponding to the maximal open pair yield, indicated by the full square in Fig. 6.5, to the results presented by Yurevich [55, 104, 105]. The two spectra are similar, especially in the region below the ρ/ω peak. The χ^2/d.o.f. for the mass region $m_{inv} > 0.2$ GeV/c^2 is 1.46, indicating reasonable statistical consistency. Also the enhancement factor over the hadronic cocktail of 2.5±0.24 for the mass spectrum shown in Fig. 6.6 compares well to the the result quoted by Yurevich.

Obviously, the observed differences between our results and previous works reflect the `systematic` uncertainties of the analysis. The systematic error of the normalized open pair yield and enhancement factor receives three main contributions:

- efficiency correction: the uncertainty introduced by the efficiency correction is estimated by systematic variation of the electron identification and background rejection cuts, adjusting the efficiency correction accordingly. We find a systematic error of the open pair yield of 8.5%, in good agreement with [54] and [55].

- background normalization: the uncertainty of the normalization of the mixed-event to the like-sign background corresponds to the error of the fit to the ratio of both invariant mass distributions (compare Fig. 3.29). We observe a 13% shift of the signal yield introduced by a 0.6% variation of the background level, roughly consistent with the estimate $\sqrt{B}/S$ for our background over signal ratio of 23.

- charged particle density: normalization of the pair yield to N_{ch} introduces a further uncertainty of 12% [74].

To summarize, we evaluate the total systematic uncertainty of our measurement to 8.5% $\oplus$ 13% $\oplus$ 12%. Since the contributions are completely independent, they can be added geometrically. The total systematic error is 20%. This value is slightly higher than the previous estimates of 15% [54] and 17%[55].

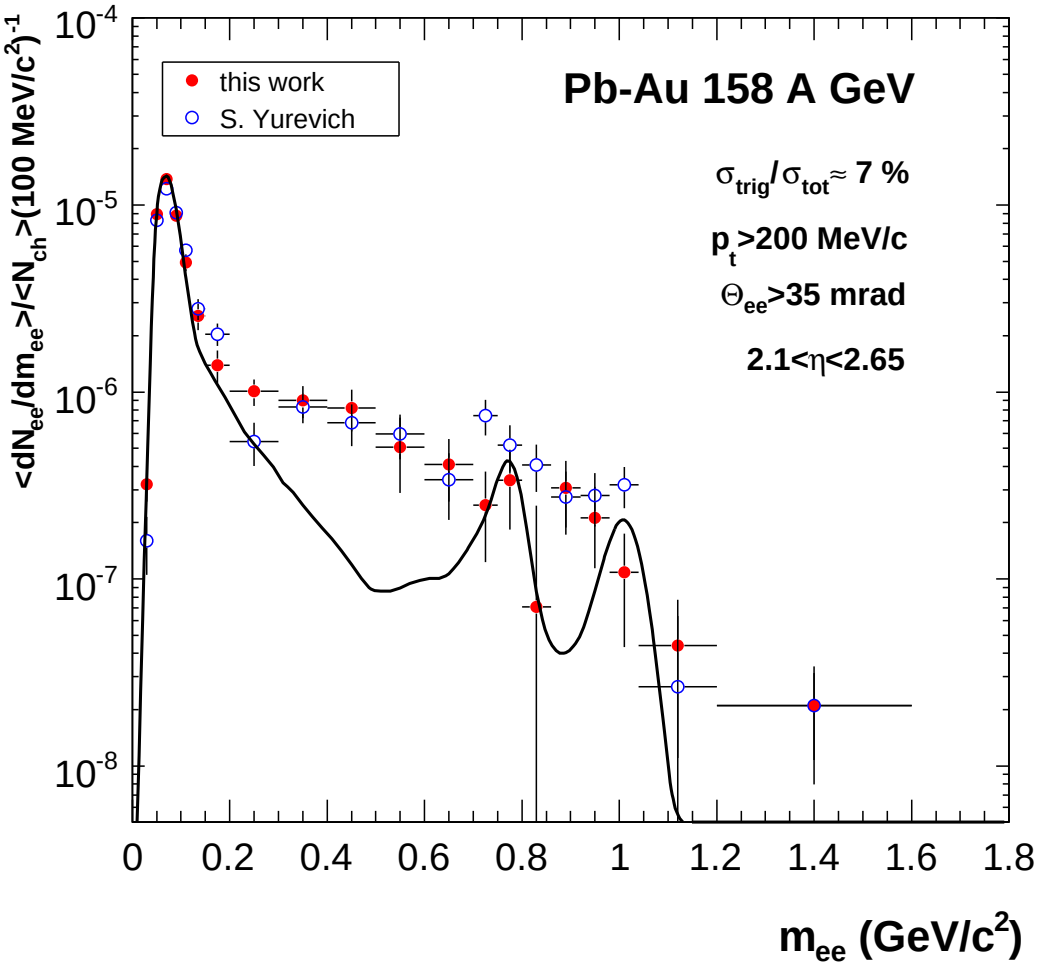

Figure 6.6: Inclusive e^+e^- invariant mass spectrum for Pb-Au collisions at 158 GeV/c per nucleon, absolutely normalized. Our spectrum obtained with a cut setting maximizing the open pair yield (comp. Fig.6.5) is compared to the results by Yurevich [55, 104, 105].

We shall compare our estimate of the systematic uncertainties to the variations observed between the different authors. We compare our value for the enhancement factor over the hadronic cocktail to the results exhibiting the strongest discrepancy, by Cherlin (compare Table 6.1). It is, however, not obvious how to properly accommodate for the statistical errors: on the one hand, in both works the same data were analyzed, and the results are possibly correlated. On the other hand, the smallness of the net open pair signal relative to the total number of analyzed events (ratio o(10^{-4})), and the difference between the results from the different analyses suggests rather weak correlation. Since the degree of correlation can not easily be evaluated, we consider the two extreme cases of perfect correlation and complete statistical independence. If both analyses are perfectly correlated, systematic effects can be evaluated via the relative difference between the enhancement factors found in each work. Since the difference reflects the uncertainty of both measure-

ments, we divide by two and find a relative systematic error on the enhancement factor of 21%. In case we consider the results statistically independent, the difference between the enhancement factors has to be reduced by the geometrical sum of the statistical error on each result. In this case we evaluate the relative systematic error to 11%. The two values should be compared to our previous systematic error, but `excluding` the error on the N_{ch} normalization, which is common to all analyses. The combined systematic uncertainty of 16% due to efficiency correction and background normalization seems to be a reasonable 'compromise' between the two extreme estimates.

For the evaluation of the enhancement factor of the measured pair yield over the hadronic cocktail we also have to account for systematic uncertainties of the calculated yield. These are different for the low-mass and the high-mass regions. The main contributions to the systematics for masses $m_{ee} < 0.2$ GeV/c^2 arise from the uncertainties in the relative production cross section of the π^0 and the parametrization of the transverse momentum and the input rapidity distributions. They add up to a systematic error of 8%. For m_{ee} above 0.2 GeV/c^2 the sources of systematic errors are in the detailed properties of the electromagnetic decays as well as the relative production cross sections of the high mass mesons. A detailed account can be found in [29, 32]. The systematic errors of the hadronic cocktail in the high-mass region were estimated to 30%. This yields an estimate of the enhancement factor over the cocktail of 2.05 $\pm$ 0.23 [stat] $\pm$ 0.41 [syst] $\pm$ 0.5 [decays].

6.5 Comparison to model predictions

Our results indicate a deviation from the hadronic cocktail: the observed dilepton signal clearly exceeds the expected cocktail yield. There are indications that matter created in nucleus-nucleus collisions at SPS undergoes a transition to the QGP phase (see e.g. [106]). However, during the fireball evolution, the system spends most of its life time in the hadronic phase. The high abundance of pions at this stage makes resonant pion annihilation and subsequent decay into dileptons the most likely explanation:

$$\pi^+\pi^- \rightarrow \rho \rightarrow e^+e^- \ . \tag{6.1}$$

One of the main evidences for a 'non-trivial' source of the dilepton pairs in heavy-ion collisions is the dependence of the dilepton signal on the charged particle density:

$$\frac{\mathrm{d}N_{ee}}{\mathrm{d}\eta} \ \sim \ (\frac{\mathrm{d}N_{ch}}{\mathrm{d}\eta})^{\alpha}$$

In [107], a quadratic dependence ($\alpha = 2$) is predicted, whereas other authors find a weaker dependence, e.g. $\alpha = 1.33$ [22] or $\alpha = 1.1$ [108]. Fig. 6.7 presents the enhancement factor over the hadronic cocktail as a function of the charged particle density for the two

invariant mass regions $m_{inv} < 0.2$ GeV/c^2 and $m_{inv} > 0.2$ GeV/c^2. If hadron decays were the only source of dielectron pairs, as is the case in p-p and p-A collisions, the data should scale linearly with charged particle multiplicity, and the normalized yield per charged particle should be unity, as indicated by the horizontal line. This behaviour is observed for the most peripheral centrality bins of the low-mass region. For the central bins, a weak enhancement over the cocktail seems to develop. In the high-mass region above 200 MeV/c^2, a much stronger enhancement is observed, exhibiting a pronounced centrality dependence which lends strong support for two-body annihilation reactions as a dominant source of the electron pair enhancement.

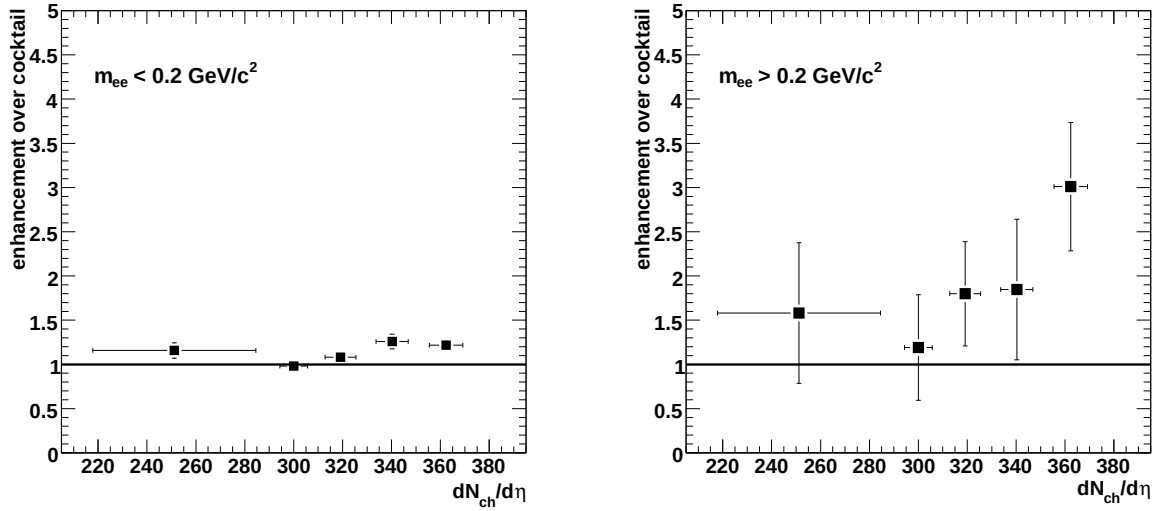

Figure 6.7: Enhancement factor as a function of the charge particle density in two invariant mass bins. The expectation from the hadronic cocktail is indicated by the black solid line showing an enhancement of 1.

In the hot and dense hadronic medium, the annihilation process is subject to modifications induced by interactions with the surrounding hadrons and/or partial restoration of chiral symmetry. Comparing model predictions to the data requires the calculation of dilepton yields in heavy ion collisions and hence a complete description of the fireball evolution. Different theoretical approaches have been developed: the hydrodynamic description is based on the assumption that the strong interactions in the matter are able to maintain local thermal equilibrium throughout the expansion of the nuclear system until some breakup stage (the freeze-out). The system is described as composed of fluid cells characterized by standard thermodynamic variables such as pressure, temperature and energy density. The basic assumptions in this class of models is the choice of initial conditions and of an Equation of State relating pressure, energy density and baryon density. The transport-theoretical approach gives a microscopic description of the fireball, propagating the phase space distribution of the individual hadrons subject to (two-body)

collisions. In this work, we choose the phenomenological fireball simulation [109, 20] by R. Rapp, implementing features of both approaches, as a representative model. It is based on temperature evolution in accordance with microscopical fireball simulations [110]

$$T(t) = (T^i - T^\infty) \exp -t/\tau + T^\infty$$

with an initial temperature of the hadronic phase T^i, a time constant τ and an 'asymptotic' temperature T^∞. The parameters of the models are constrained by experimental data: a baryon chemical potential is imposed, and the system evolves along a trajectory in the $T - \mu$ plane which can be determined from entropy and baryon number-conservation. A pion chemical potential $\mu_\pi \approx 50$ MeV is imposed to reproduce the experimentally observed pion-to-baryon ratio of 5:1. A time scale is introduced modelling the volume expansion by a cylindrical geometry as

$$V_{FC}^{(2)}(t) = 2\ (z_0 + v_z t + \frac{1}{2} a_z t^2)\, \pi\, (r_0 + \frac{1}{2} a_\perp t^2)$$

where two fire-cylinders are employed to allow for sufficient spread in rapidity distributions. Guided by hydrodynamic simulations [111], the primordial longitudinal motion is taken to be v_z=0.75, and the longitudinal and transverse acceleration are fixed to give final velocities $\mathrm{v}_z(t_{fO}) \simeq 0.75$, $\mathrm{v}_\perp(t_{fO}) \simeq 0.55$, consistent with experiment [112]. Dilepton spectra are calculated integrating the thermal rate Eq. 1.6 over the fireball lifetime, roughly 10-12 fm/c.

The dilepton invariant mass distribution resulting from the pion annihilation process strongly depends on the spectral shape of the intermediate ρ resonance formed in the process Eq. 6.1, which may be subject to strong in-medium effects. We compare our results to two models: a dropping ρ mass scenario inspired by Brown-Rho scaling and a ρ spectral distribution calculated by Rapp and Wambach.

Brown-Rho scaling [113] is based on the phenomenological implementation of the restoration of chiral symmetry in the framework of an effective field theory. A chiral Lagrange density is complemented with a scalar "glueball" field χ, related to the gluon condensate, to incorporate the breaking of scale invariance consistently with QCD. (Partial) chiral symmetry restoration in the medium is then equivalent to a reduction of the vacuum expectation value χ_* (and, along with it, the gluon condensate). For vector mesons, this entails the Brown-Rho scaling relation

$$\frac{m_\rho^*}{m_\rho} \approx \frac{m_\omega^*}{m_\omega} \approx \frac{f_\pi^*}{f_\pi} = (\frac{< q\overline{q} >^*}{< q\overline{q} >})^{1/3} = \frac{\chi_*}{\chi}$$

where quantities without asterisks stand for free-space values. Here, f_π is the pion decay constant. Brown-Rho scaling is consistent with QCD sum rules [114]. The model is equivalent to the 'Hidden Local Symmetry' approach [115], in which chiral symmetry is promoted to a a local, gauge, symmetry and vector mesons appear as gauge bosons.

In the calculations carried out by Rapp and Wambach [116], the ρ propagator (=spectral function) in hadronic matter

$$D_\rho^{L,T} = \frac{1}{M^2 - (m_\rho^0)^2 - \Sigma_{\rho\pi\pi}^{L,T} - \Sigma_{\rho M}^{L,T} - \Sigma_{\rho B}^{L,T}}$$

(where L,T denote longitudinal and transverse projections) is evaluated in terms of various contributions entering its in-medium self-energy Σ_ρ. The in-medium $\rho\pi\pi$ width, expressed through $\Sigma_{\rho\pi\pi}$ takes pion cloud modifications through $\pi N N^{-1}$ and $\pi\Delta N^{-1}$ excitations into account. $\Sigma_{\rho M}$ represents effects due to the thermal meson gas (π, K, and ρ mesons, and resonances up to 1.3 GeV). The interaction vertices are constrained by hadronic and radiative decay branchings. The ρ modifications in nuclear matter are incorporated in $\Sigma_{\rho B}$ via $\rho N \rightarrow B$ interactions ($B = N, \Delta, N(1520), \Delta(1700), N(1720) \ldots$) and constrained by photoabsorption spectra on nucleons and nuclei as well as $\pi N \rightarrow \rho N$ scattering data. In addition, a small contribution from 4π annihilation and from an early QGP phase (corresponding to a flat spectral function) are added [117].

In the upper panel of Fig. 6.8, the measured invariant mass distribution is shown along with the expectations for the two models. In addition, we show the distribution (labelled 'free') obtained from calculations implementing an unaltered ρ line shape, taking only the regeneration of the ρ meson in the fireball into account. In the lower panel, the same data are shown, after subtraction of the hadronic cocktail excluding the vacuum ρ. The systematic uncertainty of the subtraction comprises the uncertainty due to the systematic error of the data themselves, indicated by the shaded boxes, and the error of the cocktail itself, indicated by horizontal ticks. We suppress points at invariant masses $m_{inv} \lesssim 0.1$ GeV/c^2 where the systematic uncertainties become overwhelmingly large. The excess spectrum can directly be compared to the ρ spectral functions from different models. The cocktail ρ is completely negligible compared to the data, the measured excess yield dominates by more than one order of magnitude. In contrast, all three models taking ρ production via reaction Eq. 6.1 into account manage to describe the excess yield reasonably well. Comparison of the shape of the distributions clearly excludes the free ρ line shape. In the mass region above 0.5 GeV/c^2, the large statistical error of the data points does not allow to distinguish between the different scenarios. However, in the mass region below 0.5 GeV/c^2, where the two calculations differ most, the data clearly favour the Rapp and Wambach picture, in which the strong coupling of the ρ meson to baryons adds significant strength to the dilepton yield at low invariant masses [118]. In comparison to the data, the models without these effects clearly fall short for masses below 0.5 GeV/c^2. This demonstrates that the observed changes in the ρ spectral function are due to interactions of the ρ-meson with the dense baryonic medium.

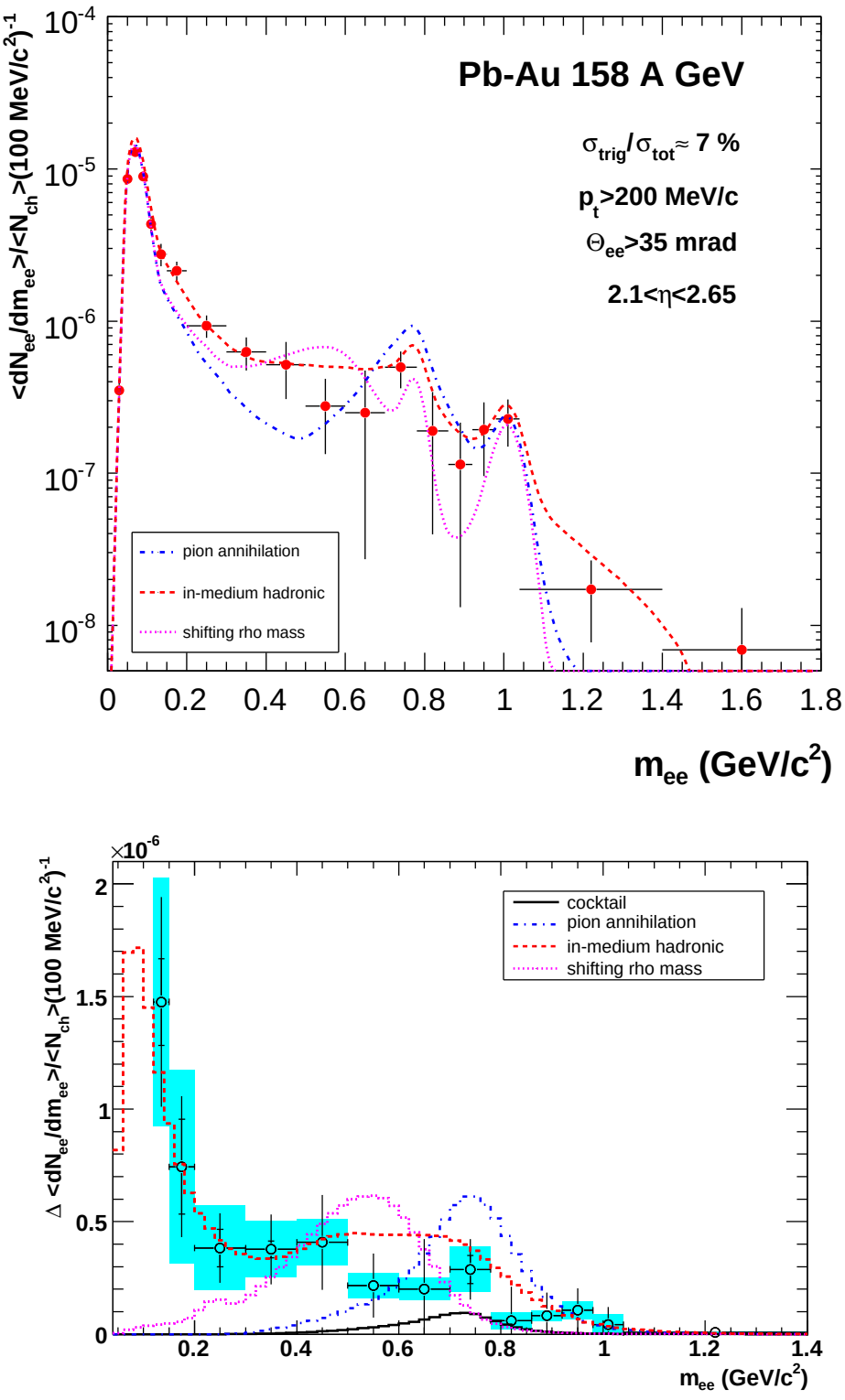

Figure 6.8: Model comparison. Upper panel: invariant mass spectrum compared to calculations assuming unaltered line shape, broadening and shift of the ρ spectral function. Lower panel: dielectron excess yield after subtraction of the cocktail without ρ meson. In addition to the systematic errors of the data (shaded boxes), the systematic errors of the cocktail subtraction are indicated by horizontal ticks.

6.6 Summary

This thesis reports on the measurement of low-mass dileptons carried out with the CERES experiment in the year 2000. The upgraded experimental setup with a radial TPC allows a new method of electron reconstruction with the RICH detector, applied in this work. The new analysis strategy represents an independent check of the previous CERES results. Our results confirm the earlier findings of a strong enhancement of dileptons over the expectations from the hadronic cocktail in the mass region $0.2 < m_{inv} < 0.6$ GeV/c^2. From the analysis of $23{\cdot}10^6$ central Pb-Au collisions we obtain for pair masses below 0.2 GeV/c^2 a normalized electron pair yield of $8.9{\cdot}10^{-6}$, consistent with the expectation from hadronic decays. Integrating over the invariant mass region $0.2 < m_{inv} < 1.1$ GeV/c^2, we obtain a yield of $3.6{\cdot}10^{-6}$, exceeding the cocktail by a factor 2.05 ± 0.23[stat] $\pm$ 0.41 [syst] $\pm$ 0.5 [decays]. In the intermediate mass region $0.2 < m_{inv} < 0.6$ GeV/c^2, the yield of $2.4{\cdot}10^{-6}$ corresponds to an even stronger enhancement factor of 2.27 ± 0.31[stat]$\pm$0.45[syst]$\pm$ 0.6[decays]. Inspection of the transverse momentum spectra allows to locate the enhancement at low p_T.

The systematic error of our results is estimated to 20%. Comparison of our results to the two previous analyses of the same data allows an alternative assessment of the systematic uncertainties of the electron analysis. At an equal level of the ratio of signal to background we find a smaller enhancement factor than presented in the previous works. Our result is consistent with [55]. The comparison to [54] permits an independent estimate of the systematic error of the electron analysis. We find good consistency between both values.

Our results demonstrate the modification of the spectral function of the ρ meson in the hot and dense medium. The data strongly support baryon-induced interactions at the origin of the effect.

7 Transition radiation spectroscopy with prototypes for ALICE TRD

In this chapter, we present measurements of transition radiation (TR) spectra in irregular radiators for different electron momenta. The measurements were carried out with prototypes of the ALICE transition radiation detector.

7.1 The ALICE experiment

The ALICE (A Large Ion Collider Experiment) [119] detector is the only dedicated heavy ion experiment at the CERN Large Hadron Collider (LHC). It is designed to study matter under extreme conditions created in nucleus-nucleus collisions at a center-of-mass energy of 5.5 TeV per nucleon pair. The physics motivation is the study and characterization of QGP in an energy regime unprecedented in the laboratory [120]. In particular, ALICE will provide the opportunity to observe, in the di-electron channel (and simultaneously in the di-muon channel), the production of J/Ψ and Υ as well as open charm and beauty [120].

The ALICE detector is conceived as a general-purpose detector, sensitive to the majority of known observables including hadrons, muons, photons and electrons. The ALICE experimental setup is shown in Fig. 7.1. The experiment consists of three major parts: 1.) the central barrel, housed in the L3 magnet, covering the pseudorapidity interval -0.9< η <0.9; 2.) the forward muon spectrometer, designed for the study of muon pairs from quarkonia decays in the interval 2.5< η <4.0 and 3.) the forward detectors, dedicated to global event characterization based on photon and charged particle multiplicity counters and forward calorimetry. In the central barrel detectors, charged hadrons as well as electrons and photons are detected. The central barrel comprises the Inner Tracking System (ITS) composed of silicon detectors, a large Time Projection Chamber (TPC), a Transition Radiation Detector (TRD) and a Time Of Flight detector (TOF), covering the full azimuth. In addition, there will be at midrapidity two single-arm detectors, an array of Ring Imaging Cherenkov Detectors (HMPID) to identify high-momentum hadrons and an array of crystals (PHOS) for photon detection.

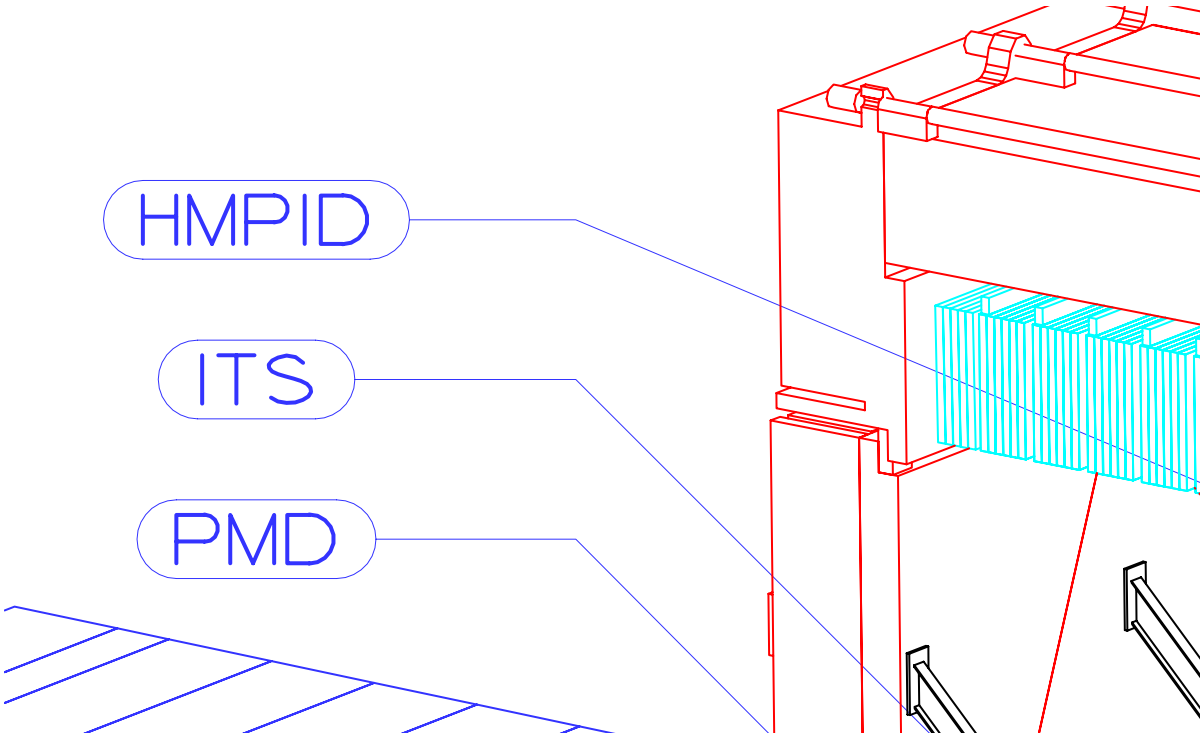

Figure 7.1: Layout of the ALICE experiment.

7.2 ALICE TRD

The ALICE TRD consists of 540 drift chambers, operated with Xe,CO_2(15%), arranged in 6 radial layers around the beam axis. The detector spans a total length of 7 m along the beam axis, with 5-fold segmentation. The radial coverage is 2.9 m$< r <$3.7 m. The total TRD active gas volume is 27 m^3. The largest drift chamber module has an area of 1.2×1.6 m^2. In front of each chamber, a radiator is attached. The radiators have a 'sandwich' structure: they consist of polypropylene fiber mats contained in boxes of a Rohacell foam.

ALICE TRD contributes significantly to the electron identification in the central barrel. An electron passing through the radiator emits transition radiation (TR) photons of an energy of typically 10 keV. The TR effect was first predicted by Ginzburg and Frank in 1946 [121]: any highly relativistic charged particle traversing the boundary between two media of different dielectric constants produces TR. The dependence of the TR yield on the Lorentz factor γ of the particle is used for particle identification: for electrons up to 2 GeV ($\gamma \approx 4000$) a strong linear increase with the energy of the particle is observed, for higher Lorentz factors the yield approaches saturation. In a big momentum range, from 1-100 GeV/c, electrons are the only particles producing transition radiation. The TR photons are emitted at a small angle $\alpha \simeq 1/\gamma$ with respect to the trajectory of the incident particle. The sensitivity of the transition radiation process to the γ-factor of

the particle is unique, any other process used for particle identification depends on β (e.g. Cherenkov radiation) or a combination of β and γ (e.g. the energy loss per unit track length dE/dx). To achieve a detectable yield of TR photons, a large number of boundaries has to be combined. For this purpose, stacks of hundreds of closely spaced foils have been constructed. In ALICE TRD, for mechanical reasons light materials, polypropylene fibres and foams, are used. The polymers provide the necessary variation of the dielectric constant by their microscopic structure. One radiator is attached to the entrance window of each drift chamber. Since the chambers are operated at overpressure, the radiator has to serve as mechanical support of the window. Fig. 7.2 shows scanning electron microscope images of the radiator materials.

In addition to its electron-pion discrimination capabilities, the TRD is a powerful tracking device and an integral part of the ALICE high-level trigger on high-p_T ($\gtrsim$2-3 GeV/c) particles.

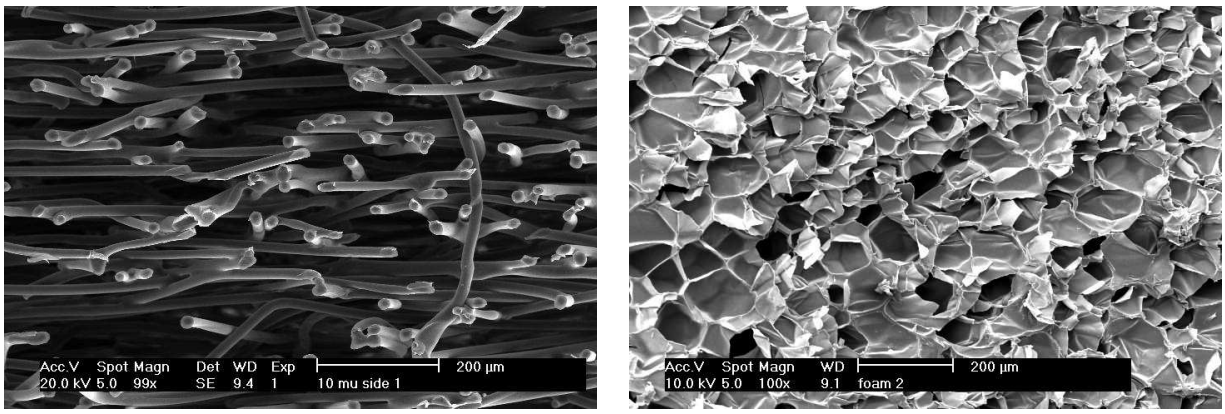

Figure 7.2: Scanning Electron Microscope pictures of the radiator materials: fibres (left panel) and foam (right panel).

7.3 Motivation

The physics performance of the TRD detector [128] is investigated in detailed simulations of the detector response. A quantitative estimate of the anticipated electron identification capabilities of the detector requires an accurate description of the energy loss processes. Electrons traversing the radiator of the TRD emit TR photons, which are subsequently absorbed and detected in the gas volume of the drift chambers. The charge deposit due to absorption of TR is always accompanied by ionization energy loss (dE/dx). Whereas the latter is well understood, the numerical treatment of TR production is more difficult. The commonly known analytic expressions for the TR spectrum apply to the case of regular radiators, i.e. foil stacks, with given foil thickness and constant spacing. Comparisons of measured TR yield and spectra have been presented by many authors for a large variety of

regular radiator configurations. In general, data confirm [122] the theoretical predictions [123], although total TR yield and dependence on the energy of the emitting particle are not always reproduced [124, 125]. Simulation of irregular-layered radiators requires knowledge of the distributions of material thickness and spacing in the medium [126], an information not easy to obtain experimentally. Measurements of spectral distributions and momentum dependence of TR produced in our radiator configuration are therefore indispensable.

7.4 Experimental setup

The measurements were carried out in October 2002 at the T10 secondary pion beam facility with natural electron contamination at CERN PS [127]. For TR detection, two prototype drift chambers (DC) with a construction similar to that of the final ALICE TRD [128], but with a smaller active area (25×32 cm^2) were used. The detectors have a drift region of 30 mm and an amplification region of 7 mm equipped with anode wires(W-Au) of 20 μm with a pitch of 5 mm. The cathode wires (Cu-Be) have 75 μm diameter and a pitch of 2.5 mm. The signal is induced on a segmented cathode plane with rectangular pads of 8 cm length and 0.75 cm width. In the prototype tests, we read out one row of 8 adjacent pads. The entrance window (25 μm aluminized Kapton) simultaneously serves as gas barrier and as drift electrode. We operate the DC with the standard gas mixture for the TRD, Xe,CO_2(15%), at atmospheric pressure. At an anode voltage of 1.56 kV used for the present measurements we achieve a gas gain of about 4000. For a drift field of 0.8 kV/cm, the drift velocity is about 2.0 cm/μs. A more detailed description of the prototypes and the readout electronics can be found in [129].

In Fig. 7.3, we present a schematic drawing of the setup of the beam measurements. The beam trigger is defined by the coincidence of the scintillators S1 and S2. Two threshold Cherenkov detectors are used as reference to distinguish electrons from pions. The radiator is composed of 8 pure polypropylene fiber mats, corresponding to 4 cm total thickness, in a box of 6 mm carbon fiber-enforced Rohacell© HF71. In order to isolate the TR photons from the beam, we detach and separate the radiator from one drift chamber and

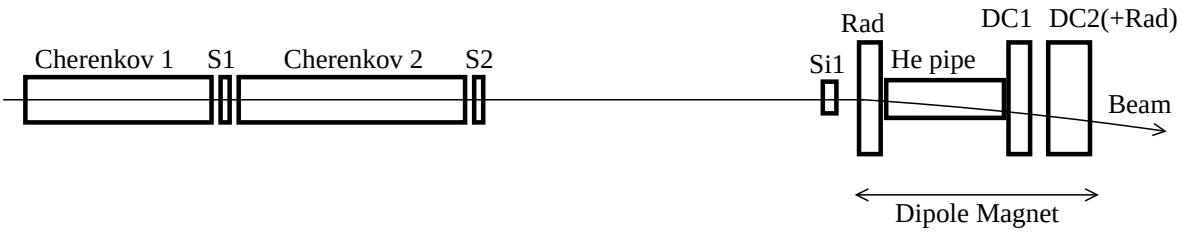

Figure 7.3: Schema of the beam setup. To dissociate TR photons and beam particles, radiator and DC are separated and placed into a dipole.

deflect the beam in the field of a dipole magnet. To minimize the absorption of TR, a He filled Plexiglas tube, 80 cm long, is placed between radiator and chamber. A second chamber for reference measurements, with radiator, is placed behind the first one. For beam momenta of 1.5, 2, 3 and 4 GeV/c the magnetic field strength is B=0.42, 0.42, 0.56 and 0.56 T. In addition, runs at B=0 are carried out for each momentum. Using dedicated triggers, the (momentum dependent) electron content of the beam is enriched to about 35000 per data file, compared to typically 15000 pions. (in the analysis, the data sample for the 1.5 GeV/c run is reduced to 3400 electrons, due to initial operational instabilities of the magnet). Fig. 7.4 presents a view into the magnet, showing the radiator in the foreground, the helium pipe and the two chambers.

Figure 7.4: Beam setup: view into the dipole magnet. The radiator, the helium pipe and the two drift chambers can be seen.

7.5 Simulations

The simulations presented in this work are carried out within the framework AliRoot [130], in a dedicated implementation reproducing the setup of the beam measurements. The interaction of the charged particles with the detector materials and their energy loss are simulated using Geant3 (compare [131]). For the simulation of the performance of the TRD detector system a quantitative understanding of TR is indispensable. Since the production of TR is not included in Geant3, it was explicitly added in AliRoot, under the form of an approximation for the TR yield for a regular stack of foils with fixed thickness. A particle crossing a single interface of two semi-infinite media emits TR photons in the

X-ray range with a spectral density

$$\frac{\mathrm{d}^2W}{\hbar\mathrm{d}\omega\mathrm{d}\Omega} = \frac{\alpha}{\pi^2}\left(\frac{\theta}{\gamma^{-2}+\theta^2+\xi_1^2} - \frac{\theta}{\gamma^{-2}+\theta^2+\xi_2^2}\right)^2 \tag{7.1}$$

$\xi_i^2 = \omega_{Pi}^2/\omega^2$, ω_{Pi} is the plasma frequency for the two media and γ the Lorentz factor of the incident particle. Typical values for ω_P are $\omega_P^{CH_2}$=20 eV, ω_P^{Air}=0.7 eV. The angle θ is measured with respect to the incident particle. If the particle traverses a single foil of thickness d_1, the contributions from two interfaces add coherently and one obtains

$$\frac{\mathrm{d}^2W^{(1)}}{\hbar\mathrm{d}\omega\mathrm{d}\Omega} = \frac{\alpha}{\pi^2}\left(\frac{\theta}{\gamma^{-2}+\theta^2+\xi_1^2} - \frac{\theta}{\gamma^{-2}+\theta^2+\xi_2^2}\right)^2 4\,sin^2\frac{\phi_1}{2} \tag{7.2}$$

with the phase

$$\phi_i = \frac{\omega d_i}{2c}(\gamma^{-2}+\theta^2+\xi_i^2)\ .$$

The generalization of Eq. 7.2 to the case of a radiator consisting of N foils with equal thickness d_1 and spacing d_2 is given by

$$\frac{\mathrm{d}^2W^{(N)}}{\hbar\mathrm{d}\omega\mathrm{d}\Omega} = \frac{\mathrm{d}^2W^{(1)}}{\hbar\mathrm{d}\omega\mathrm{d}\Omega}\,\frac{1+exp(-N\sigma)-2\,exp(-N\sigma/2)\,cos(N(\phi_1+\phi_2))}{1+exp(-\sigma)-2\,exp(-\sigma/2)\,cos(\phi_1+\phi_2)} \tag{7.3}$$

where $\sigma = \mu_1 d_1 + \mu_2 d_2$, μ_1 and μ_2 are the linear absorption coefficients of the two media and depend on the energy of the emitted radiation. We use values tabulated in [132].

The angular distribution resulting from Eq. 7.3 is numerically integrated over the forward solid angle for photon energies from 0 to 100 keV. The pronounced interference pattern requires an elaborate summation in very small θ intervals. Convergence and sufficient precision was reached summing up the spectrum in $\gtrsim 3{\cdot}10^5$ steps with variable step sizes.

We consider W as average energy radiated by many particles of the same Lorentz factor traversing the radiator and producing photons of energy ω. The number of produced quanta follows Poisson statistics. The mean number of photons is $\langle \mathrm{N}_x \rangle = \mathrm{W}/\langle\omega\rangle$ [133], where $\langle\omega\rangle$ is the mean of ω determined from the spectral distribution $\mathrm{d}W/\mathrm{d}\omega$. For the radiator configuration used in the present article, d_1=12 μm d_2=100 μm N=220[1], $\langle \mathrm{N}_x \rangle$ is about 1.5. For each incident electron of a given momentum, the number of produced photons and their energy is generated randomly. Then, the photons are propagated through the experimental setup. The detection efficiency in the chamber is determined by the X-ray absorption cross sections [132]. We also implement absorption in the materials before the chamber, incorporating the detector entrance window, the caps of the Helium pipe, and the 80 cm Helium layer, which induce photon losses. Scattering, the production of δ-electrons, and bremsstrahlung or synchrotron radiation are not included.

[1]The configuration was tuned to reproduce the measured total deposited TR energy in the detector but is not unambiguously determined. However, inspection of Fig. 7.2 shows that the chosen parameters compare well to the typical microscopic dimensions of the radiator.

7.6 Signal reconstruction

In Fig. 7.5 we show for one incident electron the FADC pulse height (PH) distribution from 8 pads in each DC as function of the drift time. A deconvolution of the detector signal was carried out to optimize the time response [128]. The time zero is arbitrarily shifted by 500 ns to have a measure of the baseline. Two TR photons are detected on the upper 3^{rd} pad in the first DC. Charge sharing spreads the signal over 3 adjacent pads. The beam ionization clusters are deposited on the lower pads, in both chambers. The non-perpendicular beam incidence, due to the deflection in the magnetic field, is seen as a displacement of the beam in pad direction along the abscissa and between the two DC.

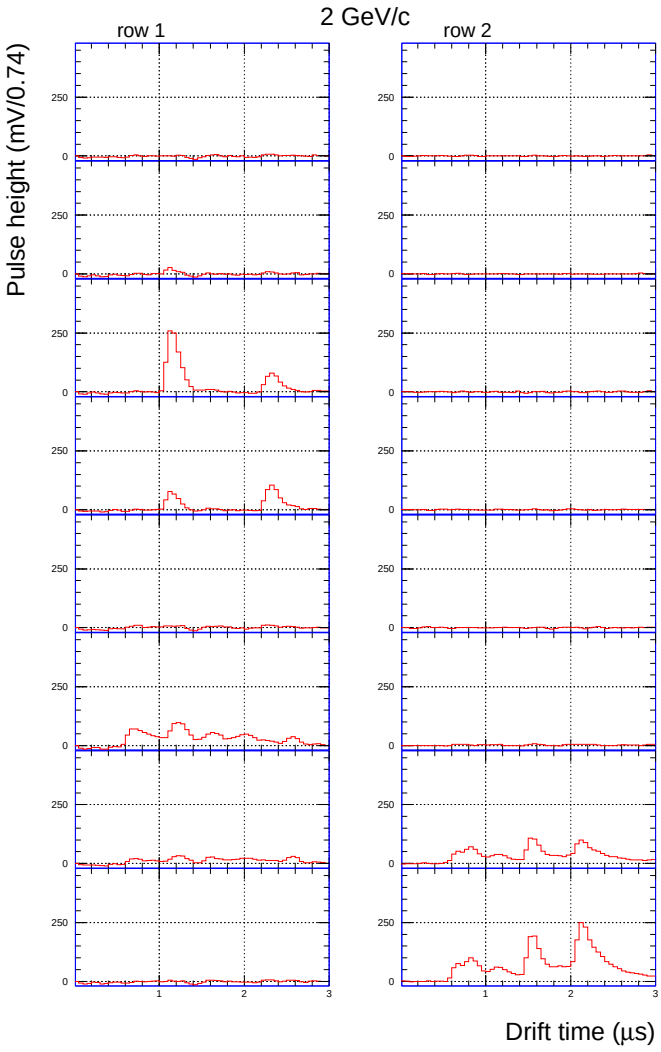

Figure 7.5: FADC signal for one incident electron. The two columns correspond to 8 adjacent pads of each DC. In the upper 3^{rd} pad, two TR photons can be seen. The pulse-height signal from the beam is measured on the lower pads, in both chambers.

For a clean measurement of the TR spectrum it is mandatory to clearly discriminate between the signal from the absorbed photons and from the ionization energy loss (dE/dx). The expected separation between beam and TR is easily estimated: for momenta of 1.5, 2, 3 and 4 GeV/c and B-field settings as given above, the average distance between beam and TR is 2.7, 2.0, 1.8 and 1.3 cm, respectively. With increasing momentum the beam gets stiffer and the higher magnetic field compensates only partially. Hence, for the higher momenta, clean reconstruction of the TR spectra becomes more and more problematic. The separation between the photons and the beam corresponds to roughly four to two times the pad width, and charge sharing between the pads can lead to an overlap between TR and ionization clusters. Furthermore, the scattering of the TR photons, the angular spread of the beam and the Lorentz angle of the deposited charge drifting in the detector result in a wide distribution of the charge deposit from photons and beam particles over the readout pads. Consequently, a careful treatment of each event is mandatory to reconstruct the TR signal undisturbed by the dE/dx signal and avoid contamination of the measured spectra.

To reconstruct the charge deposited by TR photons, we scan pads 1-6 for possible TR clusters. A cluster is defined as follows:

- signal over threshold during at least 4 subsequent time bins (200 ns),
- charge sharing with at least 1 neighbor pad.

The threshold is twice the baseline spread and is determined individually for each run. The pulse height (PH) is summed over the contributing pads (3 at maximum) in the relevant time interval to obtain the total charge. Multiple overlapping clusters are resolved detecting local minima in the PH distribution that occur on two adjacent pads at the same time. The charge deposited by the beam particle is tagged via typical configurations of pads with large signal over long time intervals, preferentially on pads 6 to 8 and simultaneously in both drift chambers. Each TR cluster accepted to contribute to the charge spectra fulfills the following conditions:

- the incident beam particle is an electron
- the beam is unambiguously identified in the DC
- 'safety distance': in the relevant drift time interval, the separation between the TR cluster and the beam is two pads or more.

In case the distance is exactly 2 pads, the signal measured on the interjacent pad can not be unambiguously assigned to the beam or the TR cluster. In this case the cluster is rejected unless the contribution of the interjacent pad to the total cluster charge is less than 5%.

For TR photons incident on pad 1, a fraction of the total charge is lost on a neighbor pad without connection to the readout electronics. From the measured charge on pad 1 and 2 the total charge of the cluster can be recovered using the measured pad response function [134]. The average correction to the measured charge is below 10%. The total contribution of such clusters is only about 2%.

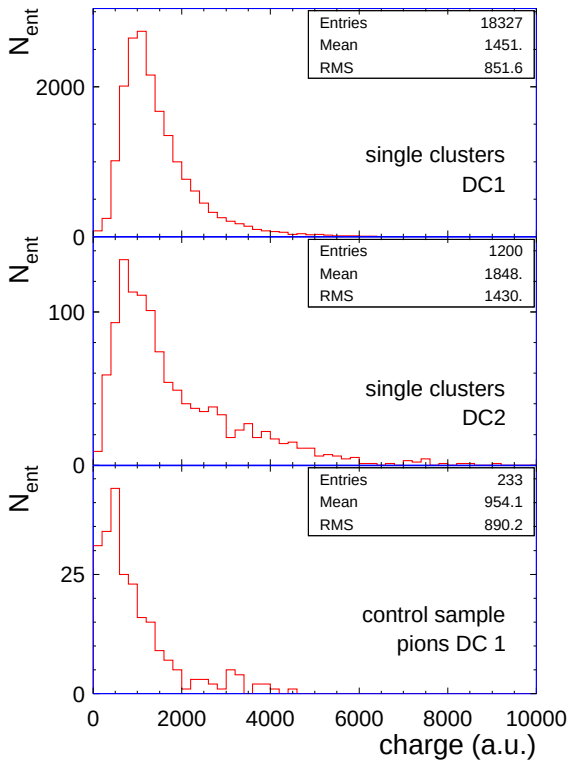

Figure 7.6: TR charge spectra for 2 GeV/c. Upper left and right panels: single clusters in DC1 and 2. Lower panel: charge of fake 'TR' clusters reconstructed for incident pions.

The resulting charge spectra are presented in Fig. 7.6. The upper plots show the charge per photon, i.e. per single cluster, detected in DC1 and 2. Due to the high absorption cross section for low energy photons in the Xe-based gas mixture, the majority of the TR photons is detected in DC1. Only a fraction of relatively hard photons penetrates to DC2. Correspondingly, the number of photons measured in DC2 is much lower, and the distribution displays a stronger tail towards high values of the deposited charge. The plot in the bottom panel illustrates the powerful fake rejection of the cluster search algorithm. We show clusters accepted as TR for the case of incident pions (for the momentum range covered in our measurements, pions do not emit TR and we do not expect a TR signal). A fake cluster is produced for less than 2% of all incident pions.

7.7 Cluster number distribution

In the left panel of Fig. 7.7 we present the normalized distribution of the detected photon number per incident electron for 2 GeV/c beam momentum. The shape of the distribution compares well with a Poissonian, indicated by the dashed curve. On average 0.61 photons per incident electron are detected. This number is smaller than expected from simulations ($\sim$0.8 for the measured momenta). To some extent, TR overlap due to the finite time response of the detector and associated electronics accounts for this discrepancy, as illustrated in the right panel. The minimum time interval between two TR photons resolved in the measurements is 0.2 μs. The measurements are compared with the distribution obtained in simulations with ideal 2-cluster resolution. For higher momenta, increasing stiffness of the beam results in smaller separation to the TR photons and stronger rejection of detected clusters. As a consequence, the number of reconstructed TR clusters drops to 0.43 for 3 GeV/c.

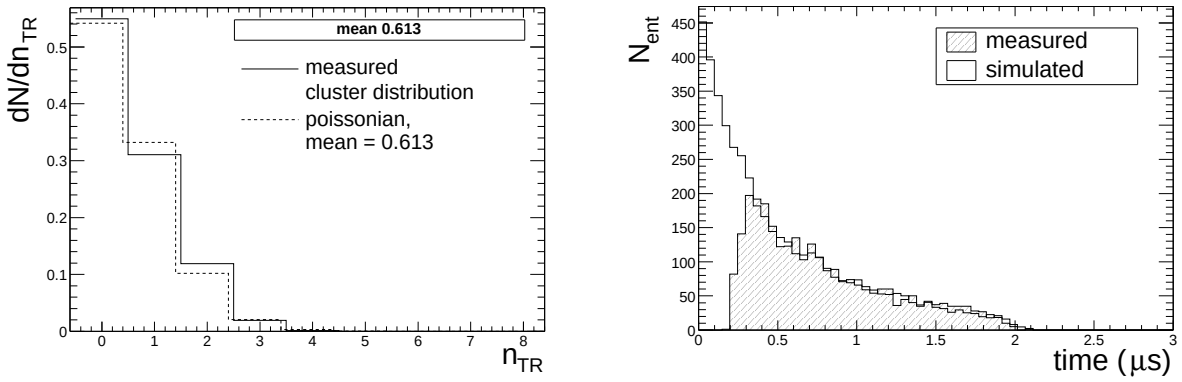

Figure 7.7: Left panel: photon number distribution for 2 GeV/c beam momentum, compared to a Poissonian distribution with equal mean. Right panel: cluster overlap. Measured time interval between 2 TR photons for 2 GeV/c beam momentum compared to the distance between 2 TR photons in simulations with ideal 2-cluster resolution. The distributions are arbitrarily normalized.

7.8 TR energy

To relate the measured charge to the corresponding photon energy we compare the charge deposit in pion runs at B=0 to the simulated energy deposit [131]. To avoid any bias by single track space charge effects, which are maximal at perpendicular beam incidence, we use the charge collected at the beginning of the drift time, in the amplification region of the DC.

The calibration factors obtained comparing for different momenta the most probable values (m.p.v.) of the measured charge distribution and the simulated energy spectra agree to an accuracy of 2.7%. The main sources of errors are: 1) the uncertainty of the assignment of the average pulse height distribution to the amplification region, which is determined for each run by variation of the interval of charge summation by ± 1 time bin. It is typically 10%. 2) the deviation of the measured relative to the simulated shape of the charge spectrum, due to the inhomogeneous field in the amplification region and lack of statistics, resulting in an error of 2.5% in determining the m.p.v.

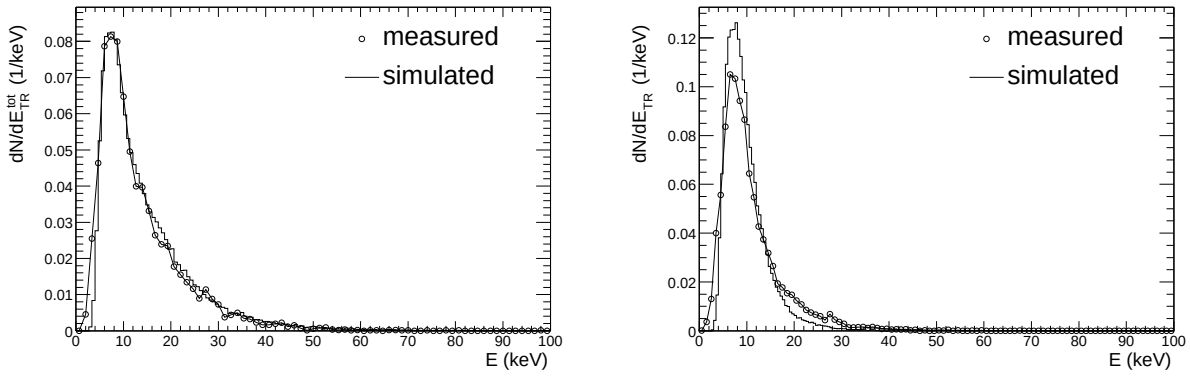

Figure 7.8: Spectra of total TR energy (left panel) and energy per photon (right panel) for 2 GeV/c electron momentum.

In Fig. 7.8 we present the spectra of total TR energy and energy per photon for a beam momentum of 2 GeV. The simulations reproduce the total TR spectrum, whereas the single photon spectrum has a more pronounced tail towards higher energies than calculated, presumably as a consequence of cluster overlap. The evolution of the mean and m.p.v. of the spectra[2] as function of momentum is shown in Fig. 7.9. The errors on the data points are a 5% uncertainty on the measured charge, reflecting the tolerance of the TR search algorithm to contamination from ionization, and the error of the energy calibration. The m.p.v. of the spectra is determined by a Gaussian fit to the maximum. An additional error of 5% on the m.p.v. accounts for the variation of the fit with the fit interval. The data seem to indicate a systematic increase of the TR yield as function of momentum which is not present in the simulations. However, within the errors, which are dominated by the systematic error of the calibration, the simulations agree very well with the measured values.

[2]Note, that in the presented TR spectra the entries in bin 0 are suppressed, since they are mostly due to the rejection of clusters with insufficient separation to the beam. Hence, the mean of the spectra as presented here is `not` the mean TR energy per incident beam particle.

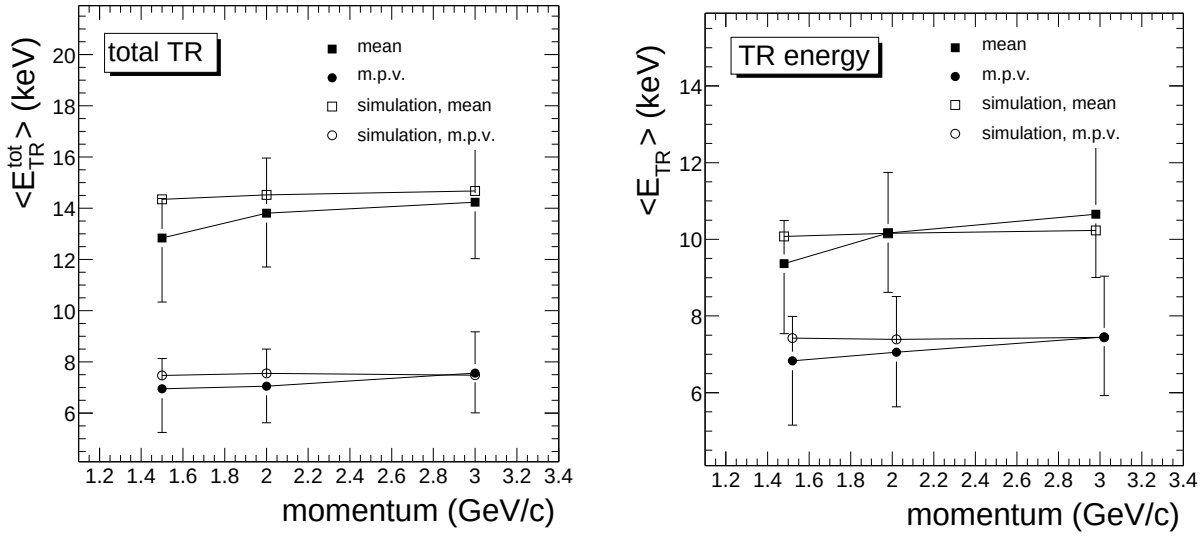

Figure 7.9: Mean and most probable value of the spectra of total TR (left panel) and single photon energy (right panel). The data are compared to simulations.

7.9 Conclusions and perspectives

We have measured, for the first time, the spectral distribution of TR produced in irregular radiators of the type used in ALICE TRD. We could demonstrate that simulations implementing regular radiators reproduce not only the total TR yield but also the spectral shape reasonably well. This observation is important for the simulations of ALICE TRD, which entirely rely, for practical reasons, on regular radiator parametrizations. This approach receives considerable support by our results.

The successful analysis of the first attempt of this kind of measurement during a TRD test beam in 2002 triggered a dedicated campaign in 2004, described in [135], with the goal to investigate systematically TR production from regular and irregular radiators over a wide range of beam momenta. Our results, presented in [129], suggest a series of experimental improvements which were realized in 2004. Most importantly, the setup was modified to ensure sufficient separation between the beam and the produced TR photons, the energy calibration was significantly improved by Fe-source measurements carried out systematically between the runs and the drift electric field was lowered, reducing the drift velocity, to improve the 2-cluster separation. The results [135] nicely corroborate our findings.

Appendix

A Step3c/step4c: technical information

The information stored in the step3c ROOT tree format is organized in 6 classes: CSEvent, CSSegment, CSSegSD, CSSegTPC, CSSegRICH, CSSegPion. The CSSegment class is the base class from which the detector specific 'track' segment classes derive: CSSegSD and CSSegTPC for SDD and TPC segments, CSSegRICH for RICH rings with asymptotic radius reconstructed with the spatial Hough algorithm and CSSegPion for rings with non-asymptotic radius. Each segment contains the indices of the segment with the best match (minimizing the opening angle) in each other detector. All segments are sorted according to their azimuthal coordinate CSSegment::fPhi. The index of each segment within the array is also stored on the segment itself, and can be retrieved as the index of the best matching segment from the same detector. During step3 production, the event vertex is refitted using the known target positions and the TPC tracks are fitted using a map of measured residuals [70] ('step 2.5'). The coordinates are calculated with respect to the accurate vertex position. The non-asymptotic rings stored in CSSegPion are obtained at the level of step2 for each SDD track matching to a high-momentum TPC track. A ring fit is performed to the RICH raw data (pads), for the both RICHes combined and separately for RICH1 and RICH2, to determine precisely ring center and radius. Since the step2 momenta and SDD coordinates are modified by the refitting, some of the original values used for the ring fit are preserved on the CSSegPion class.

Step4c stores the information of the raw data reproduction. The step4c event class, CSEventRICH, contains the complete RICH hits (CSHitRICH) and the soft tracks (CSSegTPCSoft). In addition, the results of the track dependent and hit based RICH reconstruction, for TPC and SDD predictors, are stored (CSRingTPC and CSRingSDD). CSSegTPCSoft inherits from CSSegTPC, hence all variables of the standard TPC segment are equally available for the soft segment. In addition, for each soft segment an attempt is made to establish and fit a kink track 'appendix'. For this purpose, each soft track segment is prolonged adding the closest TPC hit in each plane (without requiring any matching condition). Both the 'straight' part previously established and the new 'kink' appendix are fitted with a straight line fit of ρ versus z and a second order polynomial fit of ϕ vs z to calculate the position and distance of closest approach.

Table A.1: List of data members of the CSEvent class

variable type	variable name	description
Int_t	fRun	run number
Int_t	fBurst	burst number
Int_t	fEvent	event number
Int_t	fTime	production time of event
Int_t	fPattern	trigger pattern (beam=1, minb=2, cent=4, ...)
Int_t	fRich1RecoveryTime	time from last discharge Rich1 (20 ms)
Int_t	fRich2RecoveryTime	time from last discharge Rich2 (20 ms)
Float_t	fBeamBefore	last preceding beam (ns)
Float_t	fBeamAfter	first following beam (ns)
Float_t	fBC1ADC	(adc-mean_adc)/sigma for BC1
Float_t	fBC2ADC	(adc-mean_adc)/sigma for BC2
Int_t	fBC3ADC	BC3 (not calibrated)
Bool_t	testBit 14 set	step2.5 vertex refitting successful
Bool_t	testBit 15 set	step2.5 TPC track refitting successful
Int_t	fCentralityMC	centrality from MC
Int_t	fCentralitySD	centrality from SD
Int_t	fCentralityTPC	centrality from TPC
Float_t	fx1eta1SD	reaction plane for SD X v1 1.7<eta<2.2
Float_t	fy1eta1SD	reaction plane for SD Y v1 1.7<eta<2.2
Float_t	fx2eta1SD	reaction plane for SD X v2 1.7<eta<2.2
Float_t	fy2eta1SD	reaction plane for SD Y v2 1.7<eta<2.2
Float_t	fx1eta2SD	reaction plane for SD X v1 2.2<eta<2.7
Float_t	fy1eta2SD	reaction plane for SD Y v1 2.2<eta<2.7
Float_t	fx2eta2SD	reaction plane for SD X v2 2.2<eta<2.7
Float_t	fy2eta2SD	reaction plane for SD Y v2 2.2<eta<2.7
Float_t	fx1eta3SD	reaction plane for SD X v1 2.7<eta<3.2
Float_t	fy1eta3SD	reaction plane for SD Y v1 2.7<eta<3.2
Float_t	fx2eta3SD	reaction plane for SD X v2 2.7<eta<3.2
Float_t	fy2eta3SD	reaction plane for SD Y v2 2.7<eta<3.2
Float_t	fx1TPC	reaction plane for TPC X v1
Float_t	fy1TPC	reaction plane for TPC Y v1
Float_t	fx2TPC	reaction plane for TPC X v2
Float_t	fy2TPC	reaction plane for TPC Y v2
		continued on next page

Table A.1 - Continued from previous page

variable type	variable name	description
Float_t	fVertexX	vertex X (cm)
Float_t	fVertexY	vertex Y (cm)
Float_t	fVertexZ	vertex Z (cm)
UChar_t	fTarget	target ID
TClonesArray*	fSegSD	array of SDD segments
TClonesArray*	fSegRICH	array of RICH rings from spatial Hough
TClonesArray*	fSegPion	array of RICH pion rings
TClonesArray*	fSegTPC	array of TPC segments
TClonesArray*	fHitsRICH	array of RICH hits from step2 (obsolete!)

Table A.2: List of data members of the CSSegment class. These variables are common to all detector segments.

variable type	variable name	description
Float_t	fTheta	segment coordinate: polar angle
Float_t	fPhi	segment coordinate: azimuthal angle
Int_t	fIdxSD	index to best matching SDD segment
Int_t	fIdxSD_s	index to best matching SDD segment non-vertex
Int_t	fIdxRICH	index to best matching RICH asymptotic ring
Int_t	fIdxPion	index to best matching RICH pion ring
Int_t	fIdxTPC	index to best matching TPC segment
Float_t	fMatchdPhiSD	match to SDD segment: $\Delta\phi$
Float_t	fMatchdPhiSD_s	match to SDD non-vertex: $\Delta\phi$
Float_t	fMatchdPhiRICH	match to RICH ring: $\Delta\phi$
Float_t	fMatchdPhiPion	match to RICH non-asymptotic ring: $\Delta\phi$
Float_t	fMatchdPhiTPC	match to TPC segment: $\Delta\phi$
Float_t	fMatchdThetaSD	match to SDD segment: $\Delta\theta$
Float_t	fMatchdThetaSD_s	match to SDD non-vertex: $\Delta\theta$
Float_t	fMatchdThetaRICH	match to RICH ring: $\Delta\theta$
Float_t	fMatchdThetaPion	match to RICH non-asymptotic ring: $\Delta\theta$
Float_t	fMatchdThetaTPC	match to TPC segment: $\Delta\theta$

Table A.3: List of data members of the CSSegTPC class.

variable type	variable name	description
Float_t	fTheta	segment coordinate: θ RICH2 mirror
Float_t	fPhi	segment coordinate: ϕ RICH2 mirror
UChar_t	fnHits	number of hits
UChar_t	fnFittedHits	number of fitted hits
Float_t	fChi2Rad	χ^2 of ρ-vs-z linear fit
Float_t	fChi2Phi	χ^2 of ρ-dϕ vs z (momentum) fit
Float_t	fdEdx	dE/dx (truncated mean)
Float_t	fPcor2	momentum: 2-parameter fit
Float_t	fPcor3	momentum: 3-parameter fit
Float_t	fThetaMean	average θ of first 4 hits on track
Float_t	fPhiMean	average ϕ of first 4 hits on track
Float_t	fPhiR2MnoFringe	ϕ RICH2 mirror, no fringe field correction
Float_t	fPhiFirstHit	phi of first hit
Float_t	fXLine0	track fit: offset x for z=0 (target center)
Float_t	fYLine0	track fit: offset y for z=0 (target center)
Float_t	fXLine1	track fit: slope dx/dz
Float_t	fYLine1	track fit: slope dy/dz

Table A.4: List of Data members of the CSSegRICH class.

variable type	variable name	description
Float_t	fTheta	segment coordinate: θ of ring center
Float_t	fPhi	segment coordinate: ϕ of ring center
Float_t	fHoughAmpl	combined hough amplitude
Float_t	fSumAmpl1	sum amplitude rich1
Float_t	fSumAmpl2	sum amplitude rich2
UChar_t	fNHits1	number of hits rich1
UChar_t	fNHits2	number of hits rich2
Float_t	fQuality	variance of the combined fit
Float_t	fRadius	ring radius in pad units

Table A.5: List of data members of the CSSegSD class.

variable type	variable name	description
Float_t	fTheta	segment coordinate: average θ of hits (topological weight)
Float_t	fPhi	segment coordinate: average ϕ of hits (topological weight)
Char_t	fSD_shared	SDD hit shared by several SDD tracks: 1=SDD1, 2=SDD2, 0=no shared hit
Char_t	fSD1_nanodes	number of anodes
Float_t	fSD1_dEdx	hit amplitude
Float_t	fSD1_resum5	resummed hit amplitudes within 5 mrad
Float_t	fSD1_resum7	resummed hit amplitudes within 7 mrad
Float_t	fSD1_resum10	resummed hit amplitudes within 10 mrad
Float_t	fSD1_dn	opening angle between closest and next closest hit
Bool_t	fSD1_splitFlag	flag raised for split hits
Char_t	fSD2_nanodes	number of anodes
Float_t	fSD2_dEdx	hit amplitude
Float_t	fSD2_resum5	resummed hit amplitudes within 5 mrad
Float_t	fSD2_resum7	resummed hit amplitudes within 7 mrad
Float_t	fSD2_resum10	resummed hit amplitudes within 10 mrad
Float_t	fSD2_dn	opening angle between closest and next closest hit
Bool_t	fSD2_splitFlag	flag raised for split hits

Table A.6: List of Data members of the CSSegPion class.

variable type	variable name	description
Float_t	fTheta	segment coordinate: θ of ring center (comb. fit)
Float_t	fPhi	segment coordinate: ϕ of ring center (comb. fit)
Int_t	fType	ring type (predictor charge, electron/pion)
Int_t	fTrackMask	type of predictor
Float_t	fRICH1_theta	ring theta
Float_t	fRICH1_phi	ring phi
Float_t	fRICH1_radius	ring radius
Float_t	fRICH1_pradius	ring predictor radius
Float_t	fRICH1_chi2	chi2 ring fit
Float_t	fRICH1_var	variance ring fit
Float_t	fRICH1_kolm	kolmogorov test rich1
Float_t	fRICH1_sumAmpl	sum amplitude rich1
Int_t	fRICH1_nHits	number of hits
Int_t	fRICH1_quality	fit quality
Float_t	fRICH2_theta	ring theta
Float_t	fRICH2_phi	ring phi
Float_t	fRICH2_radius	ring radius
Float_t	fRICH2_pradius	ring predictor radius
Float_t	fRICH2_chi2	chi2 ring fit
Float_t	fRICH2_var	variance ring fit
Float_t	fRICH2_kolm	kolmogorov test rich2
Float_t	fRICH2_sumAmpl	sum amplitude rich2
Int_t	fRICH2_nHits	number of hits
Int_t	fRICH2_quality	fit quality
Float_t	fRICHC_theta	ring theta
Float_t	fRICHC_phi	ring phi
Float_t	fRICHC_radius	ring radius
Int_t	fRICHC_nHits	number of hits
Int_t	fRICHC_quality	fit quality
Float_t	fP_pred	momentum used for radius prediction
Int_t	fIdxTPC_pred	index to predictor TPC segment
Int_t	fIdxSD_pred	index to predictor SD segment

Table A.7: List of data members of the CSEventRICH class

variable type	variable name	description
Int_t	fRun	run number
Int_t	fBurst	burst number
Int_t	fEvent	event number
Int_t	fTime	production time of event
TClonesArray	fHitsRICH	array of RICH hits
TClonesArray	fSegTPCSoft	array of soft segments
TClonesArray	fRingsTPC	array of rings, TPC predictors
TClonesArray	fRingsSD	array of rings, SD predictors

Table A.8: List of Data members of the CSHitRICH class.

variable type	variable name	description
Float	fTheta	hit coordinate θ
Float	fPhi	hit coordinate ϕ
Float	fAmp	hit amplitude
UChar	fWhichRICH	RICH1/RICH2 hit

Table A.9: List of Data members of the CSSegTPCSoft class. Note: since CSSegTPCSoft inherits from CSSegTPC, all variables from CSSegTPC are also available for CSSegTPCSoft.

variable type	variable name	description
Float_t	fchi2Kink	χ^2 straight-line fit to kink part
Float_t	fchi2Straight	χ^2 straight-line fit to straight part
Float_t	fchi2Last4Kink	χ^2 straight-line fit to last 4 hits
Float_t	fzClosestApp	z of closest approach
Float_t	fzLastHitFound	z of last hit on straight part
Float_t	fdistClosestApp	distance of closest approach
Int_t	fnHitsKink	number of hits on straight part
Int_t	fnHitsStraight	number of hits on kink part
Float_t	ftruncMean	dE/dx of all hits
Float_t	fparLineStraight[2]	ϕ vs z fit: parameters straight part
Float_t	fparLineKink[2]	ϕ vs z fit: parameters kink part

Table A.10: List of Data members of the CSRingTPC class.

variable type	variable name	description
Int_t	fIdxTPC	index of TPC predictor
Float_t	fTheta	ring center θ coordinate
Float_t	fPhi	ring center ϕ coordinate
Float_t	fNHits1NC_el	raw number of hits on ring RICH1
Float_t	fNHits2NC_el	raw number of hits on ring RICH2
Float_t	fNHitsB_el	number of hits, background corrected (straight line background fit)
Float_t	fNHitsBA_el	number of hits, background corrected (background fit adapted to non-fiducial acceptance)
Float_t	fCOGshift_el	displacement between center-of-gravity of hits and ring center
Float_t	fSumAmp_el	sum of hit amplitudes
Float_t	fRadius	free radius ring search: radius
Float_t	fNHitsBA	free radius ring search: number of hits, background corrected
Float_t	fNHits_weightShB	number of hits after hit reassignment
Float_t	fResumAmpPl0	TPC hit resummation: plane 0
Float_t	fResumAmpPl1	TPC hit resummation: plane 1
Float_t	fResumAmpPl2	TPC hit resummation: plane 2
Float_t	fResumAmpPl3	TPC hit resummation: plane 3

Table A.11: List of Data members of the CSRingSD class.

variable type	variable name	description
Int_t	fIdxSD	index of SDD predictor
Float_t	fTheta	ring center θ coordinate
Float_t	fPhi	ring center ϕ coordinate
Float_t	fNHitsNC_el	raw number of hits on ring
Float_t	fNHitsB_el	background corrected number of hits on ring
Float_t	fSumAmp_el	sum of hit amplitudes

B Ring fitting procedure

In this section, we describe the ring fit used for the track-based RICH reconstruction. After some general considerations concerning statistical distributions of data and methods of non-linear optimization [77], we describe the algorithm employed in the ring reconstruction and give an account of the technical details of the implementation.

We consider binned data, described by the bin entries $y_i(x_i) \in \mathbb{N}$, $i = 1,..., N$, where N corresponds to the number of bins. The data consist of a sample of observations drawn from a parent distribution $y_{\{a_i\}}(x)$: $\mathbb{R} \to \mathbb{R}$ with parent parameters $a_1, ..., a_k$ that determines the probability of making a particular observation. Each individual bin entry y_i is itself drawn from a Poisson distribution with mean $y_{\{a_i\}}(x_i)$. The probability of observing the set of data points $\{y_i\}$ is given by the `likelihood function`

$$P(a_1, ..., a_k) = \prod_{i=1}^{N} \frac{y_{\{a_i\}}(x_i)^{y_i}}{y_i!} e^{-y_{\{a_i\}}(x_i)} \ .$$

The fit function $y_{\{a_i\}}(x)$ is determined maximizing the likelihood function[1] or, equivalently, minimizing the negative logarithm of the likelihood (NLL)

$$\mathcal{L} = -\ln P(a_1, ..., a_k) = \sum [y_i \ln(y_{\{a_i\}}(x_i))] - \sum y_{\{a_i\}}(x_i) + const. \qquad \text{(B.1)}$$

with respect to the parameters $a_1, ..., a_k$.

In general, the fit function can not be determined analytically, especially if the fit function exhibits non-linear dependence on the parameters a_i. There are different numerical approximation methods which allow to evaluate the solution iteratively to any desired accuracy. The most straightforward method, the `grid search`, samples the parameter space, evaluating the NLL at each node, to determine the global minimum. The convergence of the grid search algorithm is generally rather slow. The number of iterations needed to converge to the minimum can be reduced using a `gradient search` algorithm: for a reasonable choice of starting values the parameters are varied so that in each iteration the resultant direction of travel in parameter space is along the gradient, the direction of maximum variation of the NLL. One disadvantage of this method is that it is difficult

[1] If the bin entries are sufficiently large to justify Gaussian approximation of the Poissonian occupation probability, maximizing $\mathcal{L}$ is equivalent to minimizing χ^2, and the fit reduces to the standard least-squares problem.

to approach the bottom of the minimum asymptotically because the gradient tends to 0 at the minimum. Better convergence in vicinity of the minimum can be achieved by parabolic expansion of the NLL hypersurface (`Newton method`)

$$\mathcal{L} \approx \mathcal{L}_0 + \sum_{i=1}^{k} \left\{ \frac{\partial \mathcal{L}}{\partial a_i}\, \delta a_i \right\} + \frac{1}{2} \sum_{i=1}^{k} \sum_{j=1}^{k} \left\{ \frac{\partial^2 \mathcal{L}}{\partial a_i \partial a_j}\, \delta a_i\, \delta a_j \right\} \ .$$

Minimizing $\mathcal{L}$ with respect to the `increments` δa_i in the parameters, we obtain a set of k linear equations in δa_i that we can write as a matrix equation

$$\vec{\beta} = \vec{\delta a}\ \ \alpha \tag{B.2}$$

$$\text{with} \quad \beta_j = -\frac{1}{2}\frac{\partial \mathcal{L}}{\partial a_j} \quad \text{and} \quad \alpha_{ij} = \frac{1}{2}\frac{\partial^2 \mathcal{L}}{\partial a_i\, \partial a_j}.$$

The step $\vec{\delta a}$ is calculated by inversion of the Hessian matrix α.

One disadvantage inherent in the analytical expansion methods is that, although they converge quite rapidly to the point of minimum NLL from points nearby, they cannot be relied on to approach the minimum with any accuracy from a point outside the region where the NLL hypersurface is approximately parabolic. The Levenberg-Marquardt algorithm [75, 76, 77] combines the best features of the Newton and the gradient search methods. It is obtained by increasing the diagonal terms of the Hessian matrix α by a factor $1 + \lambda$ that controls the interpolation of the algorithm between the two extremes. The matrix equation Eq. B.2 becomes

$$\vec{\beta} = \vec{\delta a}\ \ \alpha' \tag{B.3}$$

$$\alpha'_{ij} = \begin{cases} \alpha_{ij}(1+\delta) & \text{if } i = j \\ \alpha_{ij} & \text{if } i \neq j \end{cases}$$

If λ is very small, the steps δa_i are very similar to the solution of Eq. B.2 developed from a Taylor's expansion. If λ is very large, the diagonal elements of the Hessian matrix dominate and the matrix equation degenerates into k separate equations

$$\beta_i \simeq \delta a_i\, \alpha_{ii}$$

which yield increments δa_i in the same direction as the gradients β_i. The recipe given by Marquardt is:

1.) Compute $\mathcal{L}(\vec{a})$.

2.) Start initially with $\lambda = 0.001$.

3.) Compute $\vec{\delta a}$ and $\mathcal{L}(\vec{a}+\vec{\delta a})$ with this choice of λ.

4.) If $\mathcal{L}(\vec{a}+\vec{\delta a}) > \mathcal{L}(\vec{a})$, increase λ by a factor of 10 and repeat step (3).

5.) If $\mathcal{L}(\vec{a}+\vec{\delta a}) < \mathcal{L}(\vec{a})$, decrease λ by a factor of 10, consider $\vec{a}' = \vec{a}+\vec{\delta a}$ the new starting point, and return to step (3) substituting $\vec{a}'$ for $\vec{a}$.

In our specific application, the fit function (fiducial acceptance), presented in Fig. 3.9, is given by

$$y(x) = a_0\, x + a_1 \exp \frac{-(x-a_2)^2}{2\, a_3^2} \ . \tag{B.4}$$

($k = 4$). The slope parameter a_0 describes the background distribution, under the assumption of a locally homogeneous and isotropic density of background hits in the RICH detector. The Gaussian peak describes the signal, corresponding to a RICH ring of radius a_2. Effects like multiple scattering of the charged particle during the Cherenkov emission process, photon scattering in the radiator, the position resolution of the RICH readout etc. give rise to a certain smearing of the positions of the hits on ring with respect to the nominal radius, resulting in a finite width a_2. The number of collected photons corresponds to the area of the Gaussian, proportional to the weight a_1. In each iteration of the algorithm, it may be necessary to recompute the parameter increments δa_i from Eq. B.3 several times to optimize λ. Accumulation of the elements of the matrices α_{ij} and β_i needs to be done only once per iteration, however. For the required evaluation of the first and second derivatives of $\mathcal{L}$ we supply Eq. B.1 with the analytic form of the derivatives of Eq. B.4. Likewise, the elements of the 4×4 inverse Hessian matrix α^{-1} are computed analytically from α_{ij}.

The assumption of an isotropic background hit density is only justified within the RICH1 and RICH2 fiducial acceptance. To avoid any bias in the ring reconstruction, a geometrical correction is applied to Eq. B.4 for predictors outside of this region. The geometry is sketched, for the most relevant case of a ring predictor at low polar angle θ, in the upper panel of Fig. B.1. For simplicity, the RICH ring is reduced to a circle with radius x in the RICH1/RICH2 projective plane, and the inner rim of the RICH detector is treated as a circle with a radius R. The distance of the predicted ring center from the rim is labelled d. Any possible ring with radius $x > d$ is not fully contained in the RICH acceptance. The angle α corresponding to half the circumference of the 'missing piece' is easily obtained as

$$\cos\alpha = \frac{2Rd + d^2 + x^2}{2(R+d)x} \tag{B.5}$$

(note: $\cos\alpha \to \frac{d}{x}$ as $R \to \infty$). On average, the number of hits reconstructed on the incomplete ring relative to the hypothetic case of full containment in the RICH acceptance is

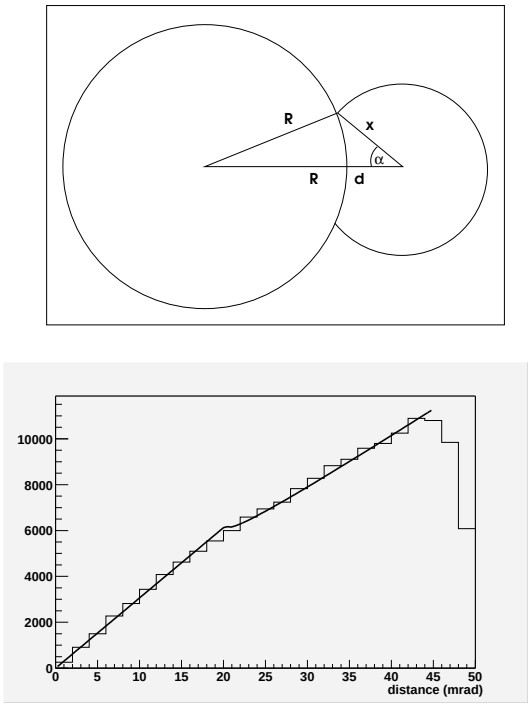

Figure B.1: RICH non-fiducial acceptance. Upper panel: sketch of the (simplified) geometry in the RICH1/RICH2 combined projective plane, for a ring with radius x located in distance d from the inner rim of the acceptance, represented by a circle with radius R. Lower panel: distribution of RICH background hits for a sample of pion tracks with momenta below the Cherenkov threshold and polar angle $0.150 < \theta < 0.160$. The data are compared to the background function Eq. B.6.

$$\frac{N}{N_0} = 1 - \frac{\alpha}{\pi}$$

($\alpha \in [0, \pi]$ by definition). Hence for predictors outside the fiducial acceptance, the background term $a_0\, x$ in Eq. B.4 is replaced by

$$a_0\, x \quad \rightarrow \quad a_0\, x \left(1 - \frac{\alpha(x)}{\pi}\right) \tag{B.6}$$

In the lower panel of Fig. B.1, we present the distribution of background RICH hits obtained from the data. For a sample of pions with momenta below the Cherenkov threshold and polar angle $0.150 < \theta < 0.160$, the distance of all RICH hits to the predicted ring center is accumulated. From about 20 mrad on, the loss of hits visibly reduces the background with respect to the extrapolation from smaller distances. The shape of the distribution is well described by the expected shape from Eq. B.6.

The opposite case of predictors close to the `outer` edge of the acceptance is treated analogously, replacing Eq. B.5 by the corresponding expression.

Bibliography

[1] H. Fritzsch, M. Gell-Mann and H. Leutwyler, Phys. Lett. B47(1973) 365

[2] D. Politzer, Phys. Rev. Lett. 30(1973) 1346

[3] D. Gross and F. Wilczek, Phys. Rev. Lett. 30(1973) 1343

[4] H. Fritzsch and M. Gell-Mann, Proc. XVI Int. Conf on High Energy Physics, Chicago-Batavia 1972

[5] S. Bethke, Progr. Part. Nucl. Phys. 58(2007) 351

[6] W.-M. Yao et al., Review of Particle Physics, J. Phys. G33(2006) 1

[7] U. Mosel, Fields, Symmetries, and Quarks, Springer 1999

[8] V. Koch, Aspects of Chiral Symmetry, Int. J. Mod. Phys. E6(1997)

[9] T. Ericson and W. Weise, Pions and Nuclei, Clarendon Press, Oxford, 1988

[10] Y. Nambu and G. Jona-Lasinio, Phys. Rev. 122(1961) 345; ibid 124(1961) 246;
Y. Nambu and D. Lurie, Phys. Rev. 125(1962) 1429

[11] M. Gell-Mann, R.J. Oakes and B. Renner, Phys. Rev. 175(1968) 2195

[12] M.A. Shifman, A.I. Vainshtein and V.I. Zakharov, Nucl. Phys. B147(1979) 385

[13] L.D. McLerran and B. Svetitsky, Phys. Lett. 98B(1981) 199

[14] J. Kuti, J. Polonyi and K. Szlachanyi, Phys. Lett. 98B (1981) 199

[15] F. Karsch and E. Laermann, Phys. Rev. D 50(1994) 6954

[16] P. Braun-Munzinger and J. Stachel, Nucl. Phys. A638 (1998) 3c;
J. Stachel, Nucl. Phys. A654(1999) 119c; nucl-ex/9903007

[17] M. Cheng el al, Phys.Rev. D74(2006) 054507,
F.Karsch for the RCB-Bielefeld Collaboration, hep-ph/0701210 (2007)

[18] Y. Aoki, Z. Fodor, S.D. Katz and K.K. Szabó, hep-lat/0609068 (2006)

[19] F. Karsch, Nucl. Phys. A698(2002) 199c,
hep-ph/0103314

[20] R. Rapp, J. Wambach, Adv. Nucl. Phys. 25(2000) 1

[21] E.V. Shuryak, Phys. Lett. B 78(1978) 150

[22] E.L. Feinberg, Nuovo Cim. A34(1976) 391

[23] L. McLerran and T. Toimela, Phys. Rev. D31(1985) 545

[24] S. Weinberg, Phys. Rev. Lett. 18(1967) 507

[25] M. Dey, V.L. Eletsky and B.L. Ioffe, Phys. Lett. B252(1990) 620;
V.L. Eletsky, Phys. Lett. B245(1990) 229

[26] J. Kapusta and E. Shuryak, Phys. Rev. D49(1994) 4694

[27] G. Chanfray, J. Delorme and M. Ericson, Nucl. Phys. A637 (1998) 421

[28] J. Delorme, M. Ericson and P.A.M. Guichon, A.W. Thomas, Phys. Rev. C 61(2000) 025202

[29] G. Agakichiev et al., Eur. Phys. J. C 4(1998) 231

[30] G. Agakichiev et al., Eur. Phys. J. C 4(1998) 249

[31] G. Agakichiev et al., Phys. Rev. Lett. 75 (1995) 1272

[32] G. Agakichiev et al., Eur. Phys. J. C41 (2005) 475

[33] S. Damjanovic, Electron-pair production in Pb-Au collisions at 40 AGeV, PhD thesis, Ruprecht-Karls-Universität Heidelberg, 2002
www.physi.uni-heidelberg.de/physi/ceres/theses.html

[34] R. Baur et al., Nucl. Instr. Meth. A 371(1996) 16

[35] P. Holl et al., CERES/NA45 Report to Cogne, CERN/SPSLC 95-20(1995)

[36] W. Chen et al., Nucl. Instr. Meth. A 326(1993) 273

[37] P. Holl et al., CERN/SPSLC 96-50(1996)

[38] D. Miśkowiec, New trigger implementation for CERES/NA45 at CERN. Technical report, GSI Scientific Report (1999) 222

[39] E. Gatti and P. Rehak, Nucl. Instr. Meth. A 225(1984) 608

[40] D. Green, The Physics of Particle Detectors, Cambridge University Press (2000)

[41] P. Holl, P. Rehak, F. Ceretto, U. Faschingbauer, J.P. Wurm, A. Castoldi, E. Gatti, Nucl. Instr. Meth. A 377(1998) 367

[42] R. Baur et al., CERES Collaboration, Nucl. Instr. Meth. A 343(1994) 87

[43] J. Jackson, Classical Electrodynamics, Second Edition, John Wiley & Sons, New York, 1975

[44] P. Glässel, Nucl. Instr. Meth. A 433(1999) 17

[45] G. Hering, Dielectron Production in Heavy Ion Collisions at 158 AGeV/c per Nucleon, PhD thesis, Technische Universität Darmstadt, 2001
www.physi.uni-heidelberg.de/physi/ceres/theses.html

[46] J. Seguinot, T. Ypsilantis, Nucl. Instr. Meth. 142(1977) 377

[47] R. Baur et al., CERES Collaboration, Nucl. Instr. Meth. A 355(1994) 329

[48] CERES collaboration, The CERES/NA45 Radial Drift Time Projection Chamber, submitted to Nucl. Instr. Meth. A

[49] W. Schmitz, Cathode pad design for the CERES TPC, CERES internal note, 1998

[50] R. Baur et al., Nucl. Instr. Meth. A 409(1998) 278

[51] D. Miśkowiec, list of runs in 2000,
http://www-linux.gsi.de/~misko/ceres/daq/run-history-2000.txt

[52] http://castor.web.cern.ch/castor/

[53] A. Maas, Teilchenidentifikation mit RICH Detektoren: Algorithmen und ihre Optimierung, Diploma thesis, Technische Universität Darmstadt, 2000

[54] A. Cherlin, Low-mass dielectron production in Pb-Au collisions at 158 A GeV using the upgraded CERES spectrometer,
PhD thesis, Weizmann Institute of Science, Rehovot, 2005
www.physi.uni-heidelberg.de/physi/ceres/theses.html

[55] S. Yurevich, Electron-Pair Production in 158 AGeV/c Pb-Au Collisions from CERES, PhD thesis, Ruprecht-Karls-Universität Heidelberg, 2006
www.physi.uni-heidelberg.de/physi/ceres/theses.html

[56] http://batch.web.cern.ch/batch/

[57] D. Antończyk, Detailed Analysis of Two Particle Correlations in Central Pb-Au Collisions at 158 GeV per Nucleon,
PhD thesis, Technische Universität Darmstadt, 2006
www.physi.uni-heidelberg.de/physi/ceres/theses.html

[58] K. Fomenko, PhD thesis, in preparation

[59] R. Soualah, PhD thesis, in preparation

[60] S. Radomski, Neutral strange particle production at top SPS energy measured by the CERES experiment, PhD thesis, Technische Universität Darmstadt, 2006
www.physi.uni-heidelberg.de/physi/ceres/theses.html

[61] M. Kalisky, PhD thesis, in preparation

[62] G.K. Tsiledakis, Scale Dependence of Mean Transverse Momentum Fluctuations at Top SPS Energy measured by the CERES experiment,
PhD thesis, Technische Universität Darmstadt, 2005
www.physi.uni-heidelberg.de/physi/ceres/theses.html

[63] J. Milošević, Investigation of Azimuthal Asymmetries in Charged and Strange Particle Distributions from CERES,
PhD thesis, Ruprecht-Karls-Universität Heidelberg, 2006
www.physi.uni-heidelberg.de/physi/ceres/theses.html

[64] M. Ploskon, Act. Phys. Hung. A, in print, nucl-ex/0511043

[65] S. Kniege, PhD thesis, in preparation

[66] http://root.cern.ch/

[67] J. Slívová, Azimuthal Correlations of High-p_T Pions in 158 AGeV/c Pb-Au Collisions Measured by the CERES experiment, PhD thesis, Max-Planck-Institut für Kernphysik, Heidelberg, 2003
www.physi.uni-heidelberg.de/physi/ceres/theses.html

[68] http://consult.cern.ch/service/afs/

[69] O. Busch, Track fitting in the CERES TPC, CERES internal note

[70] W. Ludolphs, Measurement of Open Charm in 158 AGeV/c Pb-Au Collisions,
PhD thesis, Ruprecht-Karls-Universität Heidelberg, 2006
www.physi.uni-heidelberg.de/physi/ceres/theses.html

[71] W. Allison and J. Cobb, Ann. Rev. Nucl. Part. Sci. 30(1980) 253

[72] G. Agakichiev et al., Nucl. Instr. Meth. A 394(1997) 225

[73] D. Miśkowiec et al., Nucl. Phys. A 774(2006) 43

[74] D. Miśkowiec, Charged particle multiplicity in the CERES 2000 data, CERES internal note

[75] K. Levenberg, Quart. Appl. Math. 2(1944) 164

[76] D.W. Marquardt, J. Soc. Ind. Appl. Math. 11(1963) 431

[77] P. Bevington, D.K. Robinson, Data Reduction and Error Analysis for the Physical Sciences, McGraw-Hill Science; 2nd edition

[78] H.D. Hansen et al., Phys. Rev. Lett. 91(2003) 014801

[79] D. Irmscher, Suche nach direkten Photonen in ultrarelativistischen S-Au-Kollisionen bei 200 GeV pro Nukleon, PhD thesis, Ruprecht-Karls-Universität Heidelberg, 1993

[80] T. Ullrich, Produktion von e+e- -Paaren in ultrarelativistischen S-Au-Kollisionen bei 200 GeV/u PhD thesis, Ruprecht-Karls-Universität Heidelberg, Heidelberg 1994 www.physi.uni-heidelberg.de/physi/ceres/theses.html

[81] H. Sako, Development of new GENESIS, CERES internal note

[82] P. Braun-Munzinger, D. Miśkowiec, A. Drees and C. Lourenco, Eur. Phys. J. C1(1998) 123

[83] S. Eidelman et al., Phys. Lett. B592(2004)

[84] M. Aguilar-Benitez et al., Z. Phys C50(1991) 405

[85] D. Adamova et al., Phys. Rev. Lett. 96(2006) 152301

[86] S.V. Afanasiev et al., Phys. Lett. B491(2000) 59

[87] P. Braun-Munzinger and J. Stachel, Nucl. Phys. A638(1998) 91

[88] P. Braun-Munzinger, I. Heppe and J. Stachel, Phys. Lett. B465(1999) 15

[89] C. Höhne et al., Nucl. Phys. A661(1999) 485

[90] F. Sikler et al., Nucl. Phys. A661(1999) 45

[91] P. Braun-Munzinger, J. Stachel, J.P. Wessels, N. Xu, Phys. Lett. B365(1996) 1

[92] J. Stachel, Nucl. Phys. A 654(1999) 119

[93] F. Ceretto et al., Nucl. Phys. A638(1998) 467

[94] H. Appelshäuser et al., Nucl. Phys. A638(1998) 91

[95] A. Kaneta et al., J. Phys. G23(1997) 1865; Nucl. Phys. A638 (1998) 419

[96] M.M. Aggarwal et al., Phys. Rev. Lett. 81(1998) 4087

[97] N. Kroll and W. Wada, Phys. Rev. 98(1955) 1355

[98] R.I. Dzhelyadin et al., Phys. Lett. 102B(1980) 548

[99] L.G. Landsberg, Phys. Rep. 128(1985) 301

[100] B. Friman and J. Knoll, unpublished

[101] R. Brun et al., CERN DD/EE/84-1

[102] B. Lenkeit, Elektron-Positron-Paar Emission in Pb-Au-Kollisionen bei 158 AGeV, PhD thesis, Ruprecht-Karls-Universität Heidelberg, 1998 www.physi.uni-heidelberg.de/physi/ceres/theses.html

[103] V. Ermilova et al., Sov. Phys. JETP 29(1969) 861

[104] D. Adamova et al., submitted to Phys. Lett. B, nucl-ex/0611022

[105] S. Yurevich, private communication

[106] Proceedings of the 17th International Conference on Ultra-Relativistic Nucleus-Nucleus Collisions, Oakland, California, USA, 11-17 January 2004, edited by H.G. Ritter and X.N. Wang, J. Phys. G 30(2004)

[107] V. Ĉerný, P. Lichard and J. Pišút, Z. Phys. C 31(1986) 163

[108] J. Cleymans, K. Redlich and D.K. Srivastava, Phys. Lett. B 420(1998) 261

[109] R. Rapp, G. Chanfray and J. Wambach, Nucl. Phys. A617(1997) 472

[110] Q.G. Li, C.M. Ko, G.E. Brown and H. Sorge, Nucl.Phys.A611(1996) 539

[111] C.M. Hung and E. Shuryak, Phys. Rev. C56(1997) 453

[112] J. Stachel, Nucl. Phys. A610(1996) 509

[113] G.E. Brown and M. Rho, Phys. Rev. Lett. 66(1991) 2720

[114] T. Hatsuba, Nucl. Phys. A 544(1992) 27

[115] M. Harada and K. Yamawaki, Phys. Rep. 381(2003) 1

[116] R. Rapp and J. Wambach, Eur. Phys. J. A6(1999) 415

[117] R. Rapp, private communication

[118] H. van Hees and R. Rapp, hep-ph/0603084

[119] ALICE Collaboration, Technical Proposal, CERN/LHCC/95-71.

[120] ALICE Collaboration: F. Carminati et al, Physical Performance Report, J. Phys. G 30(2004)

[121] V.L.Ginzburg and I.M.Frank, Zh.Eskp.Teor.Fiz. 16(1946) 15

[122] C.W. Fabjan and W. Struczinski, Phys. Lett. B 57(1975) 483

[123] X. Artru, G.B. Yodh, G. Mennessier, Phys. Rev. D12(1975) 1289

[124] M.L. Cherry and D. Müller, Phys. Rev. Lett. 38(1977) 5

[125] M.L. Cherry et al., Phys. Rev. D 10(1974) 3594

[126] G.M. Garibian et al., Nucl. Inst. Meth. 125(1975) 133

[127] CERN PS, http://psdoc.web.cern.ch/PSdoc/acc/pscomplex.html

[128] ALICE Collaboration, Transition Radiation Detector, Technical Design Report, CERN/LHCC 2001-021, http://www-aix.gsi.de/alice/trdtdr/index.html

[129] O. Busch et al., Nucl. Inst. Meth. A 522(2004) 45

[130] http://AliSoft.cern.ch/offline/

[131] A .Andronic et al., Nucl. Inst. Meth. A 519(2004) 508

[132] http://physics.nist.gov/PhysRefData/Xcom/Text/XCOM.html

[133] M. Castellano et al., Comput. Phys. Commun. 51(1988) 431

[134] W. Blum and L. Rolandi, Particle Detection with Drift Chambers, Springer Verlag, Berlin, Heidelberg, New York, 1993

[135] A. Andronic et al., Nucl. Inst. Meth. A 558(2006) 516

Acknowledgements

This work would not have been possible without the effort and involvement of many people to whom I want to express my gratitude. I am deeply grateful towards Prof. Peter Braun-Munzinger, who gave me the unique opportunity to join his research groups and introduced me as a new member to the CERES collaboration. I profited very much from his enthusiasm for physics - and for teaching physics - in general and his vivid interest in my work in particular.

I am deeply indebted to my supervisor Dr. Anton Andronic. I profited very much from his advice and support during - and after - the TR analysis. Special mention also deserve Dr. Dariusz Miśkowiec and Dr. Ana Marin, who never lost patience during long hours of discussion, were never at loss for a new idea or a challenging advice and were my teachers during the CERES analysis. I also want to express my thanks to Prof. Johanna Stachel and Prof. Harald Appelshäuser for many stimulating discussions and useful suggestions. I am grateful to all my colleagues from the ALICE and CERES collaborations. Without their hard work, this thesis would not have been possible. Many thanks especially to Dr. Dariusz Antończyk for his advice concerning the matching functions, the old step3c and all aspects of programming and compiling, to Dr. Sylwester Radomski for splendid collaboration during the design and implementation of the new step3c classes, as well as Dr. Alexander Cherlin and Dr. Sergey Yurevich for so much discussion and support during the electron analysis. Special thanks also to Anar Manavof for his generous help and advice in all matters related to software and programming in C++.

I am grateful to my colleagues who made my time at GSI such a pleasant one, in particular Dr. Chilo Garabatos, Matus Kalisky, Dr. Georgios Tsiledakis, and my office mate Raphaelle Bailhache, who established such a nice working atmosphere.

I finally express my thankfulness to my parents for their encouragement and support during all this time. Without them, this work would not have been realized.

Curriculum Vitae

Name:	Busch, Oliver
Born the:	07.04.1976 in Darmstadt (Germany)
Nationality:	German
Address:	Friedrich Ebert Platz 19
	64289 Darmstadt
	Germany
E-mail address:	o.busch@gsi.de

Education:

09/07 - present	Postdoc at Heidelberg University
08/02 - 08/07	PHD student at GSI Darmstadt
07/02	Diploma in Physics
05/01 - 07/02	Diploma student at
	Gesellschaft für Schwerionenforschung (GSI) Darmstadt
10/99 - 07/02	Technical University of Darmstadt
09/99 - 09/00	Université de Bordeaux I
10/96 - 09/99	Technical University of Darmstadt
07/1995	Abitur
1992 - 1995	Senior High school 'Alfred Delp', Dieburg
1986 - 1992	High school 'Auf der Aue', Münster
1982 - 1986	Primary school 'J.F. Kennedey', Münster

Civil Service:

10/95 - 10/96	Male nurse at nursing home for the elderly, Dieburg

Publications

Leptonic and charged Kaon Decay Modes of the ϕ Meson Measured in Heavy-Ion Collisions at the CERN Super Proton Synchrotron
D. Adamova et al. (CERES collaboration)
Phys. Rev. Lett. 96(2006) 152301

Transition Radiation spectroscopy with prototypes for ALICE TRD
O. Busch (for the ALICE TRD Collaboration)
Nucl. Instrum. Meth. A522 (2004) 45
physics/0404106

Results from prototype tests for the ALICE TRD
O. Busch (for the ALICE Collaboration)
Nucl. Instrum. Meth. A525 (2004) 153

Prototype Tests for the ALICE TRD
A.Andronic et al. (for the ALICE Collaboration)
GSI Scientific Report 2002, GSI 2003-1 239

Lorentz angle measurements with ALICE TRD prototypes
O.Busch et al. (for the ALICE Collaboration)
GSI Scientific Report 2001, GSI 2002-1 221

Talks

Results from CERES
physics of compressed baryonic matter, 12/2005, GSI Darmstadt

CERES detector and data analysis
CBM dilepton workshop, 05/2005, GSI Darmstadt

Elektronenidentifikation in CERES
XXXVI. Arbeitstreffen Kernphysik, 02/2005, Schleching

TR spectroscopy with prototypes for ALICE TRD
TRD 2003, 09/2003, Bari, Italy

Results from prototype tests for the ALICE TRD
Imaging 2003, 06/2003, Stockholm, Sweden

Momentum dependence of the ALICE TRD performance:
results from prototype tests
DPG Frühjahrstagung, 03/2003, Tübingen

Track Reconstruction with Prototypes for ALICE TRD
DPG Frühjahrstagung, 03/2002, Münster

Erklärung

Hiermit erkläre ich an Eides statt, daß ich die vorliegende Dissertation selbständig verfasst, keine anderen als die angegebenen Hilfsmittel benutzt und noch keinen Promotionsversuch unternommen habe.

Darmstadt, den 17. Oktober 2007,

gez. Oliver Busch